Characterisation of an Asymmetric AGATA Detector

Thesis submitted in accordance with the requirements of the
University of Liverpool for the degree of
Doctor in Philosophy

by

Carl David Unsworth

Oliver Lodge Laboratory

September 2011

"Measure what can be measured,
and make measurable what cannot be measured."

- Galileo Galilei

Acknowledgements

I can hardly believe it's finished. The last four years have been interesting and challenging in about equal parts. There are a huge number of people who have helped me out along the way and I'm sure to forget some, but here are a few of them at least...

Firstly I'd like to thank my supervisors Dr Andy Boston and Prof Paul Nolan, for the opportunity to study for my PhD with the Nuclear Physics Group in Liverpool and for constant help and advice through the course of my studies. There are so many people, academic and support staff alike, who work hard to keep the department running smoothly that I won't try and list them all. Particular thanks however must be offered to Dr John Cresswell, without his work on computing and data acquisition this thesis would not have been possible.

It's been a great pleasure to work, chat, and of course drink, with the many PhD students and post-docs that have been part of the group over the last five years and my thanks goes out to all of them. Fear of missing someone prevents me from mentioning everyone but again, there are those who have helped so much that I must mention them individually. Ren Cooper, Matt Dimmock, Steven Moon, David Oxley and David Scraggs; cheers boys.

Working with collaborators on the AGATA project from across Europe has been a wonderful experience. I'm hugely grateful to all those in Cologne, Legnaro and elsewhere who have taught me so much and made me feel at home. In particular I must mention Andrew Robinson, Bart Bruyneel, Francesco Recchia, Enrico Farnea and Michael Schlarb, all of whom helped me greatly through informative discussions.

I'd like to thank all the friends who've kept me sane over the last few years with kind words, strong drinks and banging tunes from Barndale to Waterloo and everywhere in-between. In no particular order Ange, Ste M (again), Ro, Laura, Tony, Dave (again), Martin, Danny, Ken, Nat, Bobby, Tara, Ailis, Jo, Frankie, Toni, Charlie-ann, Lucy, Ren, Nish, Adam, Sai, whoever I've missed...the lot of you...thanks. And for all of the above plus the many nights sitting in, Nick and Shell, cheers very much.

And Rach, what can I say, it's been hard being apart all this time but your support

from afar has been so valuable that I don't know how I would have got through writing up without it. Love you loads, and can't wait for us to be together again.

Finally, for support of every kind from emotional to financial, not just through this course but always, I'd like to thank my family. Mum and John, Dad and Pauline, Lynsey, Ste and Grandad, I would never have been able to do this without you, thanks so much.

Nice one, everyone. I think that's it.

Abstract

The Advanced GAmma Tracking Array, AGATA, is a European project aimed at constructing a next-generation gamma-ray spectrometer for nuclear structure studies. The completed array will consist of a 4π shell of 180 highly segmented HPGe detectors arranged into 60 triple clusters. The array will be instrumented with state of the art digital electronics, and will apply Pulse Shape Analysis (PSA) and Gamma-Ray Tracking (GRT) algorithms to achieve high efficiency while maintaining the excellent peak-to-total ratio of current escape-suppressed spectrometers.

Vital to the successful application of PSA is the establishment of a pulse shape database describing the signal shape produced by interactions at each point in the detectors volume. Electric field simulations have been developed within the AGATA collaboration to provide this signal basis but it is necessary that they are tested against experimental measurements.

Characterisation measurements were performed on asymmetric AGATA capsule C001 using the Liverpool scanning system and state-of-the-art digital electronics. A highly collimated beam of 662keV gamma rays was scanned across the detector and single and coincident trigger modes were used to measure the response due to gamma rays interacting at precisely determined points within the detector.

These signals were then compared with signals produced by the electric field simulations *Multi Geometry Simulation (MGS)* and *JAVA AGATA Signal Simulation (JASS)* and an assessment made of their performance. Position resolutions of 7.8mm and 8.4mm have been measured when performing PSA with MGS and JASS respectively. These values are larger than expected and an attempt has been made to understand the reasons for this. In addition, measurements have been carried out to assess the electronics response function of the detector and associated electronics.

The results of these characterisation measurements will be used by the AGATA collaboaration to refine the online PSA and GRT algorithms used with the array.

Contents

Chapter 1

Introduction

The atomic nucleus is a complex, mesoscopic, femtoscale (10^{-15}m) system of interacting fermions. A particular nucleus can be defined by the number of *protons*, Z, and *neutrons*, N, it contains. The stability of a nucleus depends, primarily, on the balance between the repulsive Coulomb force and the attractive nuclear forces. Within certain constraints, such as conservation of baryon number, if a nucleus can reduce its total relativistic potential energy by undergoing a decay, it will do so with some finite probability [RN95].

Modern nuclear physics seeks to describe the nature of the nuclear forces and understand what structures arise as a result of the interplay between them [HGH$^+$04]. The key questions which must be addressed to advance this goal include [UK 07]:

- What are the limits of nuclear existence? What are the heaviest elements we can make and where do the neutron- and proton-drip lines lie?
- Do new forms of collective motion occur far from the valley of nuclear stability?
- Are there new forms of nuclear matter in very loosely bound nuclear systems?
- Do the symmetries seen in near-stable nuclei appear far from stability and do we observe new symmetries?
- How are the elements and isotopes found in the Universe formed? Where are the sites of the r-process of nucleosynthesis? What are the reaction rates of key exotic nuclei in the hot CNO cycles and rp-processes?

The synthesis of exotic nuclei far from the valley of beta stability and the spectroscopy of the gamma rays emitted as they decay to their ground state has long been, and remains, one of the key experimental methods that can be used to investigate these questions.

1.1 Gamma-ray Spectroscopy

When a nucleus is created, either by the decay of another nucleus or by some nuclear reaction, it is generally in an excited state. Such a nucleus will release excess angular momentum and approach its ground state through the release of gamma rays. Spectroscopy of gamma rays is an important tool for establishing the nature of nuclear states, measuring *energy*, *lifetime* [NSS79], *angular distribution* [Kra87], and *linear polarisation* [Jon02], tells us about the excitation energy, transition probability, spin and parity of the nuclear state.

Nuclear physics accelerator facilities produce beams of nuclei which can be focused onto a target at the centre of an array of radiation detectors. The beam species, beam energy and target is chosen so as to optimise the rate of the particular nuclear reaction that is to be investigated. The decay of nuclear states populated by the reaction is then carefully studied using a gamma-ray spectrometer coupled to appropriate ancillary detectors e.g. silicon detectors for charged particle identification.

Over the last few decades, developments in accelerators for nuclear physics have involved the establishment of a number of *Radioactive Ion-Beam (RIB)* facilities which allow us to produce and investigate nuclei with more extreme masses and neutron to proton ratios than ever before. In Europe, fragmentation facilities such as the SIS/FRS at GSI in Darmstadt, Germany, produce such beams at intermediate to high energies while online isotope separation (ISOL) facilities such as SPIRAL at GANIL in Caen, France, and REX-ISOLDE at CERN in Geneva, Switzerland, produce beams at intermediate to low energies. As such, these different types of facility provide complimentary sources of information on nuclear structure. In addition several new RIB facilities, such as FAIR at GSI, SPIRAL2 at GANIL and HIE-ISOLDE at CERN, are in development that promise to provide even more exotic, high-intensity beams.

Projects such as *The Advanced GAmma Tracking Array, AGATA* [Sim06] in Europe and *The Gamma-Ray Energy Tracking Array, GRETA* [DLV+99] in the USA are now under way to produce a new generation of gamma-ray spectrometer by achieving a complete 4π shell

of *high-purity germanium (HPGe)* detectors. When completed, these devices will provide the sensitivity to weak gamma-ray signals required to fully exploit this new generation RIB facilities.

Both AGATA and GRETA are currently in the final stages of deploying their demonstration phases. The AGATA Demonstrator, being assembled in INFN Legnaro, Italy, consists of five AGATA cryostats each containing 3 individual crystals. GRETINA, which is being assembled in LBNL, Berkeley, California, consists of seven cryostats each containing four crystals.

1.2 Properties of Gamma-ray Spectrometers

In order to understand the development in gamma-ray detection technology over recent decades, and to understand the motivation for the development of new arrays like AGATA and GRETA, we must first consider the properties that make a good spectrometer.

1.2.1 Efficiency

The efficiency [VKLL01] of a detector, the fraction of gamma rays it can detect, can be measured in a number of ways. The *intrinsic efficiency*, ϵ_{int}, is the fraction of gamma rays incident upon the detector that interact in it. The *absolute efficiency*, is the fraction of gamma rays emitted from a source that deposit some energy in the detector; for an isotropic source, this can be related geometrically to the intrinsic efficiency by the solid angle subtended by the detector from the source (Ω),

$$\epsilon_{int} = \epsilon_{abs} \left(\frac{4\pi}{\Omega} \right). \tag{1.1}$$

In gamma-ray spectroscopy measurements, the important measure of efficiency is the number of gamma rays that deposit their full energy in a detector, this is known as the *photo-peak efficiency*, ϵ_{pp}.

The absolute efficiency depends strongly on gamma-ray energy and source to detector distance, this means if the efficiency of two detectors is to be compared there must be an agreed measurement scenario. The *relative efficiency*, defined as the photo-peak efficiency for 1332.5 keV gamma rays when the detector is 25cm from a point ^{60}Co source, divided by

the efficiency for a 1 inch cube Sodium Iodide detector in the same situation, is often used as a standard efficiency measure for this purpose.

To improve the efficiency of a detector array more or larger detector elements can be used to increase the amount of material with which gamma rays can interact. Alternatively detectors can be constructed from a material with higher atomic number which increases the stopping power for gamma rays due to the increased density of electrons with which gamma rays may interact.

1.2.2 Energy Resolution

Simply detecting the presence of a gamma ray is not enough to yield valuable information on a nucleus. A precise measure of the gamma ray's energy not only provides information on the excitation energy of a nuclear state but also allows different gamma rays to be distinguished in order to study other properties. Energy resolution is typically measured as the full width of a peak when it is at half of its maximum height (FWHM).

For nuclei produced in-beam at an accelerator facility, the contributions to energy resolution can be divided into two classes, those pertaining to the intrinsic energy resolution of the detector and those that result from the fact that the nuclei are not at rest in the lab frame. HPGe detectors have the best intrinsic energy resolution of any detector type for nuclear spectroscopy, the factors contributing to this will be discussed in *Chapter 2.*

The energy resolution component due to the nuclear recoil velocity comes about due to the apparent shift in energy of a gamma ray depending on whether the source is moving toward or away from an observer. The measured energy of a gamma-ray is given by,

$$E_\gamma = E_{\gamma 0}\frac{\sqrt{1-\beta^2}}{1-\beta cos\theta} \tag{1.2}$$

where β is the recoil velocity as a fraction of the speed of light, and θ is the angle between the emitted gamma ray and the direction of motion of the nucleus. The finite opening angle of detectors, and the uncertainty on the direction of motion of the recoil, lead to uncertainty in θ, differentiating *Equation 1.2* with respect to θ gives an expression for the uncertainty introduced by this effect, *Equation 1.3.*

$$\frac{\Delta E_\gamma}{E_\gamma} = \frac{\beta sin\theta}{1-\beta cos\theta}\Delta\theta \tag{1.3}$$

An additional source of uncertainty is the loss of energy of the nucleus as it moves through the target material, this leads to uncertainty in β which in turn produces uncertainty in the corrected energy.

The combination of all these uncertainties leads to the total energy resolution of the array [BS96]:

$$\Delta E_{\gamma}^{total} = \left(\Delta E_{int}^2 + \Delta E_{open}^2 + \Delta E_{ang}^2 + \Delta E_{vel}^2\right)^{\frac{1}{2}} \tag{1.4}$$

where E_{int}, E_{open}, E_{ang} and E_{vel} represent contributions from the intrinsic detector resolution, the opening angle of detectors, the opening angle of the recoil cone and the uncertainty in velocity, respectively.

ΔE_{int} can be optimised by improving the noise characteristics of the detector and associated electronics, but there is a fundamental limit imposed by the uncertainties involved in charge production within the detector (see *Chapter 2*).

ΔE_{ang} and ΔE_{vel} are dependent on the choice of beam and target used in the experiment and so cannot be improved by changes to spectrometer used to measure the gamma ray. Ancillary detectors can help to reduce ΔE_{ang} if they are used to measure the trajectory of the outgoing reaction products

The remaining contribution, ΔE_{open}, is a function of the position sensitivity of the gamma-ray spectrometer. The more precise the determination of the position of a gamma-ray interaction, the smaller the effective opening angle and hence the smaller the contribution to the energy resolution. This thesis aims to contribute towards improving the position sensitivity through the use of *Pulse Shape Analysis* (see *Section 1.3.2*).

1.2.3 Resolving Power

It is convenient to consider a single parameter, *Resolving Power*, that provides a measure of the total sensitivity of an array after all factors have been considered, *Equation 1.5* is a commonly used definition [BS96].

$$R = \left(\frac{SE_{\gamma}}{\Delta E_{\gamma}^{total}}\right) PT \tag{1.5}$$

where $\Delta E_{\gamma}^{total}$ is the FWHM resolution of the gamma rays in the spectrum, PT is the ratio of counts in the peaks to counts in the background of the spectrum (*peak-to-total*)

and SE_γ is the average separation energy of the gamma rays being studied. As SE_γ is independent of the properties of the detector system, any attempt to improve the resolving power must focus on improving the energy resolution and peak-to-total.

Increasing the peak-to-total ratio can be achieved by either detecting more photopeak events using more or larger detectors, by rejecting more of the background using Compton Suppression (*Section 1.2.4*), or by employing gamma-ray tracking (*Section 1.3.3*).

The energy resolution can be reduced to some degree by improving the intrinsic detector resolution however, in most nuclear physics experiments, the majority contribution is due to Doppler broadening. Increasing the granularity of the array i.e. using more, smaller, detector elements allows a more precise determination of the angle, θ, and hence an improved correction for Doppler effects. In traditional arrays however, this is in conflict with the desire to increase the number of full energy events and so a compromise must be made.

The final factor we need to consider is related to both the detector and the nature of the nucleus being studied. The gamma-ray *multiplicity* is defined as the number of gamma rays emitted from a nucleus in order to reach its ground state. A related quantity, the *detector fold*, is the number of gamma rays detected in the spectrometer array. When analysing data from a nuclear physics experiment, a common technique involves *gating* on a particular gamma ray and seeing what other gamma rays were detected at the same time. Multiple successive gates can be applied to a data set, each one of which selectively reduces the number of nuclei contributing to a spectrum but increases the peak-to-total ratio. The total number of gates applied in an analysis is known as the *coincidence fold*, ultimately the process of applying successive gates reaches a statistical limit where there are no longer clear peaks in the spectrum on which to gate. This limit can be extended, and hence the achievable peak-to-total improved, by increasing the photopeak efficiency of an array.

1.2.4 Spectrometers of the Past and Present

Since the Compton-suppressed, high resolution array, TESSA0 [SSS88], there has been a steady improvement in the resolving power of gamma-ray spectrometers [Lee99], [ES08].

TESSA0, *Figure 1.1*, was the first array to improve the peak to total ratio by adding a *Compton Suppression Shield* to each detector crystal, this is a high efficiency, scintillation detector (Sodium Iodide (NaI(Tl)) in the case of TESSA0) which covers the back and sides

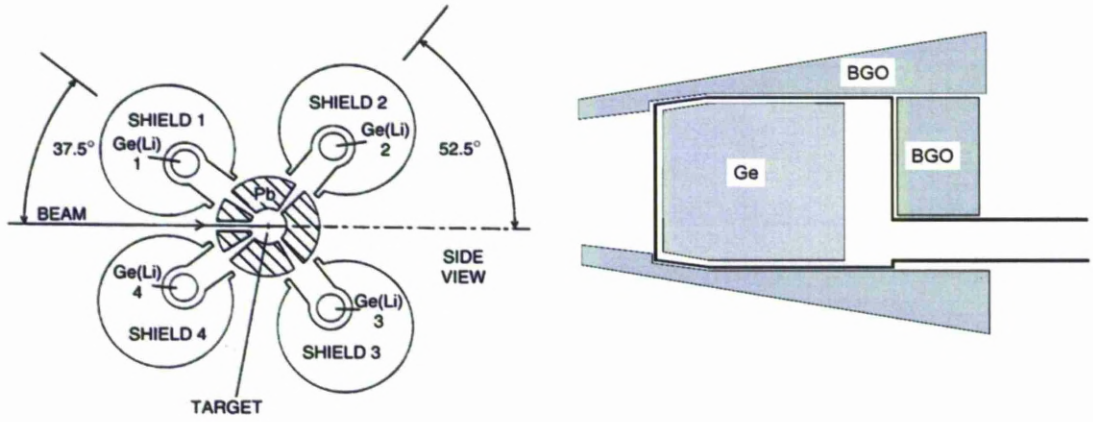

Figure 1.1: TESSA0 side view [ES08] (left), showing the four Ge(Li) detectors surrounded by NaI(Tl) escape suppression shields. The detectors are arranged around the target position with lead shields to prevent gamma rays from directly triggering the escape suppression shields. A single Gammasphere detector module [Lee99] (right), showing a single HPGe detector and BGO escape suppression shields. The full Gammasphere array contains 110 of these modules arranged in a complete 4π shell around the target position.

of each crystal. The shield is operated in anti-coincidence with the detector so that any gamma ray which deposits part of its energy in the crystal before scattering out will likely be detected in the shield and the interaction is vetoed. This approach produces a large reduction in the background count rate and hence improves the peak-to-total ratio.

Later arrays improved on TESSA0 by increasing the number of detector crystals and hence the total solid angle subtended by the array and the total efficiency [NGT85]. The NaI(Tl) suppression shields were replaced with the higher efficiency scintillator, Bismuth Germanate (BGO) which allowed for thinner shields and hence more room for additional Germanium crystals. Today's most powerful completed array is Gammasphere [Lee90], currently at Argonne National Lab, Illinois. It consists of 110 HPGe detectors equipped with BGO suppression shields and has a photopeak efficiency of $\approx 9\%$ for 1 MeV gamma rays, *Figure 1.1.*

Figure 1.2 [Sim05] shows the sensitivity of selected gamma-ray detector arrays in terms of the smallest fraction of the reaction channel that can be observed as a function of spin. Selected nuclear structure phenomena that have been revealed as sensitivity has increased

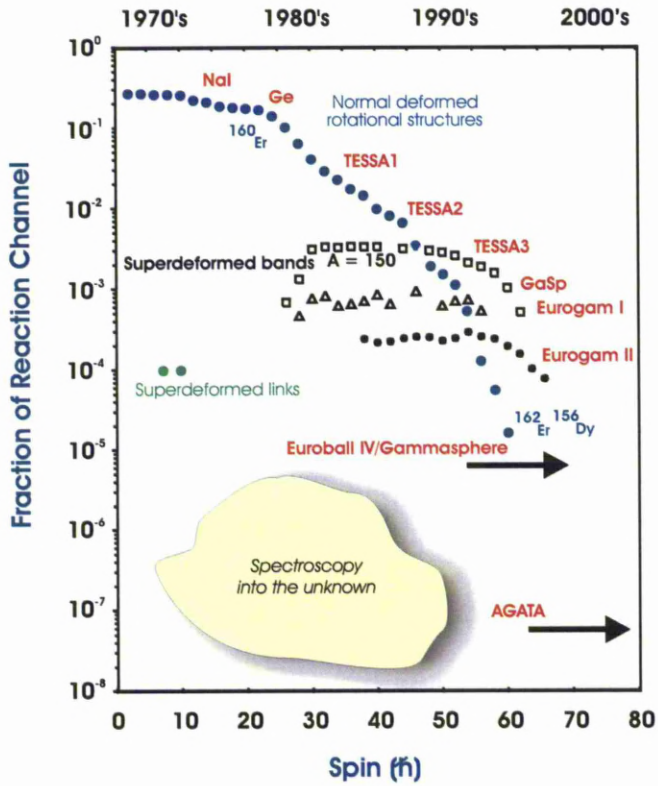

Figure 1.2: Plot showing the development of gamma-ray spectrometers over the last few decades [Sim05] from early NaI scintillators to recently proposed 4π gamma-ray tracking arrays. The sensitivity of selected arrays is shown in terms of the smallest fraction of the reaction channel that can be observed as a function of spin. Each major increase in detector sensitivity has revealed new types of nuclear structure phenomena.

are indicated. It is hoped that the improvement provided by the development of AGATA and GRETA will reveal further new and interesting physics.

However, improvement upon the latest Compton suppressed arrays requires a new approach. The peak-to-total ratio they provide is excellent but further improvements in efficiency are restricted by the fraction of the solid angle covered by the suppression shields. Larger germanium crystals could be used, thereby increasing the fraction of events depositing their full energy in a crystal. However this would reduce the granularity, thereby increasing the uncertainty in θ and the probability of more than one gamma ray being counted in a single detector.

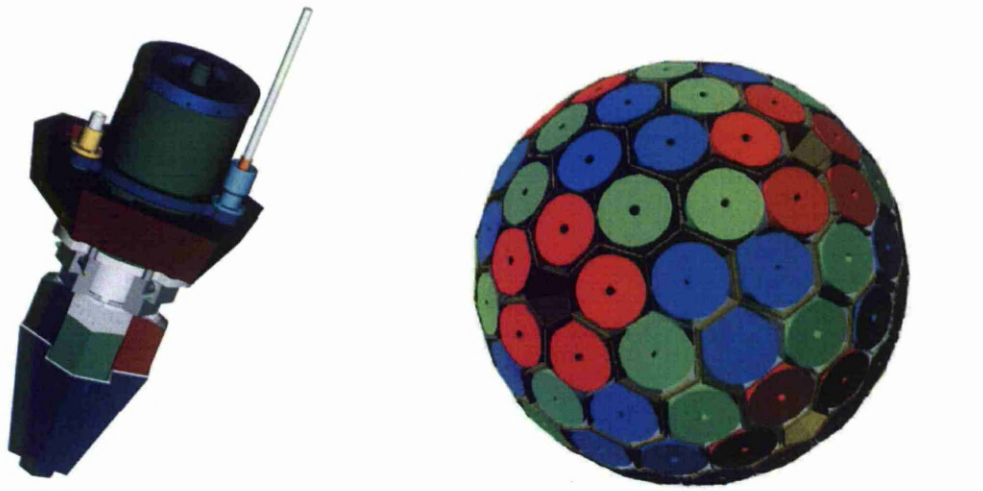

Figure 1.3: An AGATA triple cluster containing three AGATA crystals in a common cryostat, preamplifier electronics, liquid nitrogen Dewar and support structure (left) and the layout of the complete AGATA shell of HPGe crystals (right).

1.3 AGATA

1.3.1 Design and Goals

The AGATA collaboration seeks to improve on the efficiency of existing arrays by achieving a complete, 4π shell of HPGe detectors, while maintaining the peak-to-total ratio of current state-of-the-art arrays. It will achieve this by using highly segmented detectors to improve the granularity and then tracking gamma-ray paths through the array so that the incident energy and angle can be recovered from photons which interact in more than one detector element.

The AGATA design consists of 180 coaxial n-type HPGe detectors mounted in 60 triple clusters [WHB+10], *Figure 1.3*. In order to allow complete tessellation of the spherical surface, three different, asymmetric, hexagonal profiles are used for the crystals, *Figure 1.4*.

During detector manufacture, which is carried out by Canberra France, poly-crystalline Germanium is melted then purified by *zone refining* before the single crystal is grown from a seed using the *Czochralski technique* [KR90]. The outer contact of each detector is produced by boron implantation and electrically segmented into 6 sectors and 6 rings resulting in 36

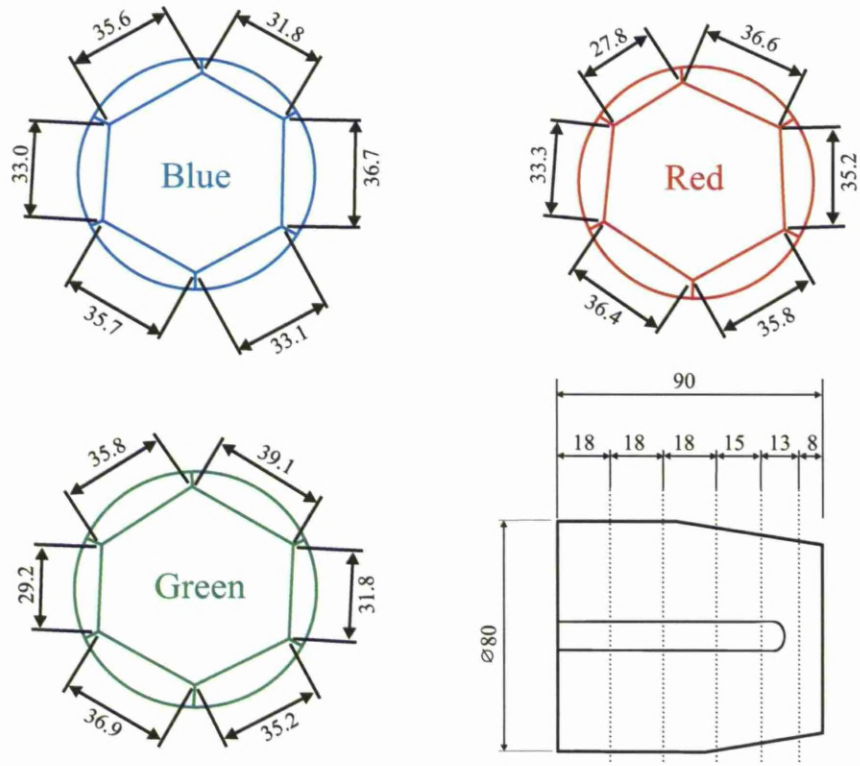

Figure 1.4: The front profile of the three AGATA crystal shapes, red, green and blue. The fourth figure shows the side profile, with the positions of the outer contact boundaries shown. The contact depths for rings 1 to 6 are 8, 13, 15, 18, 18, 18mm respectively, the diameter of the circular profile at the back is 80mm for all crystal shapes. [AAA+11]

effective detector elements in each crystal. The central contact has a diameter of 10mm and is produced by lithium drifting [ES08]. The contacted, HPGe crystal (*Figure 1.5*) is then encapsulated in an aluminium casing, and provided to the AGATA collaboration for assembly into a cryostat. The figure also shows the labelling convention for the detector segments. The sectors are labelled A-F and the rings 1-6, giving each segment a unique combination of letter and number.

1.3.2 Pulse Shape Analysis

Although each AGATA crystal is highly segmented, with the proposed completed array containing 6480 individual detector elements, the granularity is not sufficient to achieve the

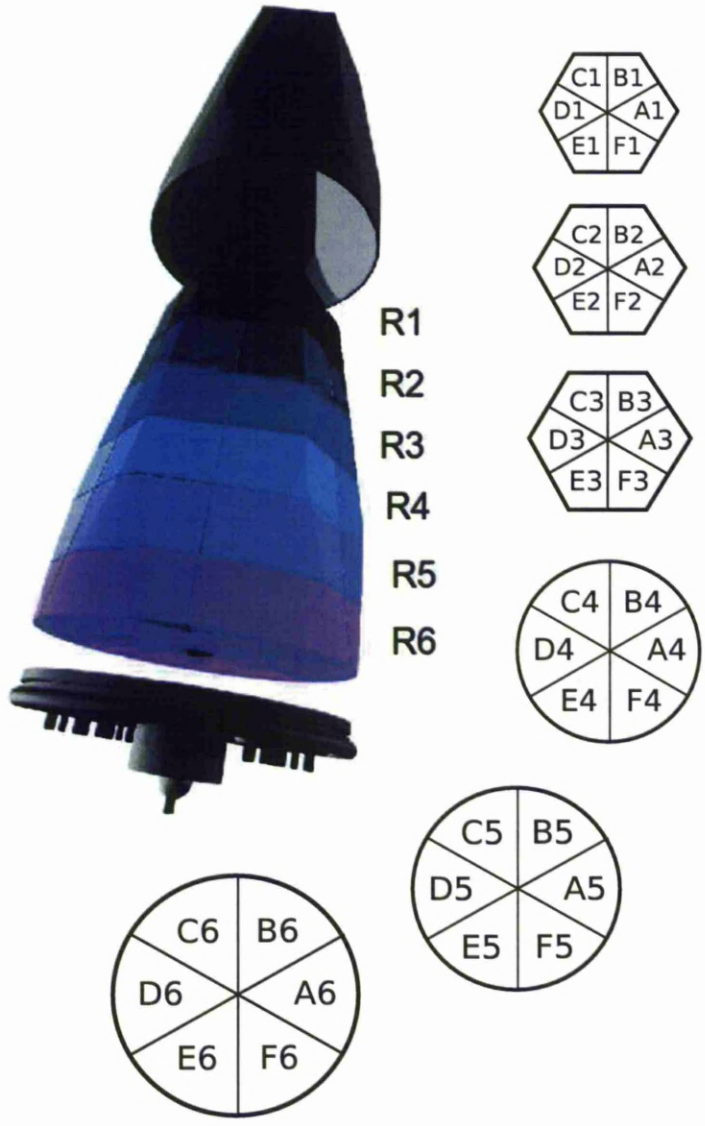

Figure 1.5: An AGATA crystal, aluminium capsule, and high voltage and readout connectors. The outer contact is electrically segmented into 6 rings (R1-6) and six sectors (A-F), producing a total of 36 detector elements per crystal.

position sensitivity required for gamma-ray tracking (*Section 1.3.3*). In order to achieve the required granularity, AGATA will exploit the dependence on the gamma-ray interaction position of the signal shape produced by the detector, a technique known as *Pulse Shape Analysis*, PSA.

In order to implement PSA, there must first be a method of storing the signal shapes, this is accomplished in AGATA using state-of-the-art digitisers with a 100MHz sampling rate and 14bit dynamic range. Once signals have been recorded there are a number of ways to extract information on the position of interaction.

The simplest approaches rely on the definition of parameters relating to the rise time of charge signals in the detector and the magnitude of signals induced in neighbour segments [Kro96], [DNB$^+$05]. This approach is tried and tested however it is limited by the inability to process events with coincident interaction in more than one detector segment. This limitation arises due to the inability to deconvolve the signals induced on segments due to the different interactions.

An alternative approach is to construct a *pulse-shape database* which stores theoretically determined pulse shapes for a grid of interaction positions within the detector. Observed detector signals are then compared with those in the database and the interaction is judged to have occurred at the point with the best matching database signal. This method has the advantage of being able to process multiple interactions by comparing observed signals with a superposition of those from multiple different points in the database, and is the approach that will be adopted by AGATA [Gor03] and GRETA [Vet00].

1.3.3 Gamma-ray Tracking

As discussed earlier, AGATA is intended to improve upon the efficiency of the current generation of arrays while still maintaining the excellent peak-to-total ratio provided by Compton suppression. With sufficiently accurate determination of interaction positions, this is possible using *Gamma Ray Tracking*, GRT. When a series of interactions occur in the array, the positions will be tested against the restricted kinematics of Compton Scattering (see *Equation 2.5*) and the most probable scatter paths will be identified. This allows the identification of interactions resulting from a single gamma ray to be grouped and then the total energy and initial position of interaction identified.

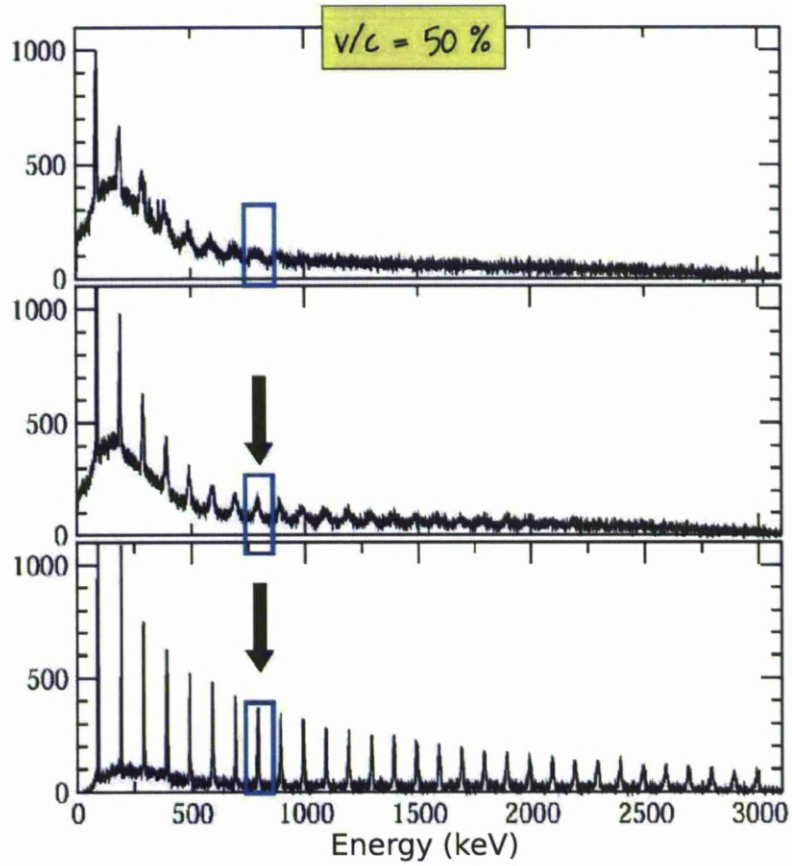

Figure 1.6: Simulated gamma-ray spectra showing the energy deposited in AGATA by the decay of a rotational band with gamma-ray multiplicity 30 and a recoil velocity of 50% v/c. Spectra are shown with a Doppler correction using the crystal position only (top), the segment position (centre), and full gamma-ray tracking using the MGT forward tracking algorithm (bottom). The blue box highlights the improvement in resolution for a single transition.

There are a number of algorithms being developed to implement online GRT including *forward tracking* [LHK+04], *back tracking* [LHK+04] and *deterministic annealing filter (DAP)* [DDLM10]. *Figure 1.6* shows the effect on a gamma-ray spectrum of applying GRT. The spectra are produced from simulated data representing the decay of a rotational band with multiplicity 30 and a recoil velocity of 50% v/c. The Doppler correction has been performed using only the crystal positions (top), the segment positions (centre), and full GRT using a forward tracking algorithm (bottom). The fully tracked spectrum shows the

excellent peak-to-total ratio that is maintained even at such high recoil velocities, allowing transitions up to 3 MeV to be clearly distinguished.

Application of tracking algorithms to such simulated data with normally randomised positions suggest that accurate tracking can be performed if interaction positions can be located to within 5mm FWHM (2.1mm standard deviation).

1.4 AGATA Performance

The unprecedented performance of AGATA will be such that the array will be able to exploit a wide range of different experimental conditions. In order to achieve the maximum scientific benefit it will moved between European labs and coupled to a range of ancillary detectors, thereby allowing the widest possible range of nuclear reactions to be investigated. The completed 4π array will have an unprecedented photopeak efficiency of 50% for 1 MeV gamma rays.

The initial demonstrator phase of AGATA is currently taking place at the stable beam facility in Legnaro National Lab, Italy. Five AGATA triple clusters are currently in place at the target position of the PRISMA magnetic spectrometer and experiments are ongoing with the dual purpose of exploring new physics and developing the hardware and software components of AGATA itself. While the Demonstrator phase has a lower photopeak efficiency of 6.7% it still represents a powerful instrument in its own right.

Figure 1.7 shows simulated spectra produced by the emission of 1 MeV gamma rays from ^{90}Zr nuclei with an energy of $\approx$350 MeV (FWHM = 35 MeV). The Doppler correction has been performed by combining the recoil trajectory information from the PRISMA spectrometer with the interaction position of the gamma rays found using CLARA [GNdA+03] (red, green) and using the AGATA Demonstrator positioned at 14cm (blue) and 24cm (black) from the target position. The recoiling nuclei were emitted uniformly within a 10° cone around the entrance of PRISMA. Combining the information from PRISMA and AGATA allows the resolution of gamma-ray energy to approach the intrinsic limit of the detector, a significant improvement over the performance of CLARA/PRISMA.

Once the commissioning and physics experiments at Legnaro are complete, the array will be moved to the SIS accelerator at GSI. Here it will be employed to detect the gamma rays produced from reactions with the high energy secondary beam such as secondary

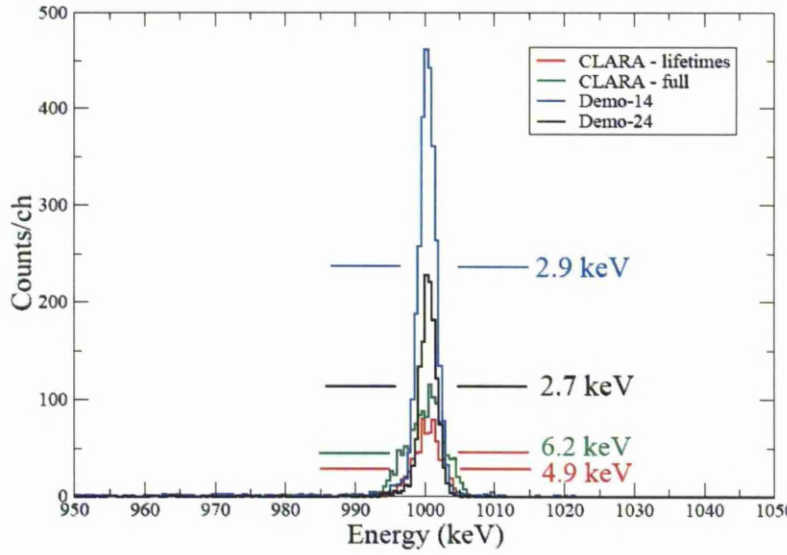

Figure 1.7: Simulated spectra showing the peaks produced by the emission of 1 MeV gamma rays from ^{90}Zr nuclei with an energy of ≈350 MeV (FWHM = 35 MeV). The Doppler correction has been performed using the recoil trajectory information from the PRISMA spectrometer combined with the CLARA Compton suppressed HPGe clover array [GNdA+03] and with the AGATA Demonstrator at each of two distances from the target (14cm and 24cm). Using full GRT in the Demonstrator, it is possible to produce an energy resolution close to the intrinsic detector limit.

fragmentation reactions and relativistic Coulomb excitation. The position sensitivity of AGATA should allow energy resolutions of ≈1% for v/c of 0.5. Combined with the increased efficiency of the array, this improved energy resolution will allow $\gamma - \gamma$ coincidences to be measured with fragmentation reactions. During the GSI stage the array will be upgraded to include up to 30 detector crystals, taking the total photopeak efficiency to >10% for 1 MeV gamma rays.

The third AGATA campaign will take place at GANIL in France. Here the array will be coupled with several existing state-of-the-art spectrometers such as EXOGAM [FdR+00] and VAMOS [Sav03] to exploit the wide range of beam species and energies that can be produced. At this stage AGATA will be upgraded to the 1π stage with 15 triple clusters and a photopeak efficiency to >20% at 1 MeV.

1.5 This work

The aim of this work is to characterise the response of an AGATA detector in order to aid the creation of an accurate pulse-shape database for PSA. In order to achieve this measurements have been carried out on AGATA crystal C001 mounted in a single test cryostat at the University of Liverpool. Data have been collected using a full digital acquisition system using both collimated sources mounted on an automatic scanning table and 'flood' sources.

Software has been developed to extract from the data information useful for the successful application of pulse-shape analysis. The charge transport process within the detector has been studied and compared with the results of electric field simulations. In addition, the electronic response function has been studied and parameters to allow a correction for proportional crosstalk have been determined.

Chapter 2

Detector Signal Formation

As discussed in Chapter 1, the AGATA spectrometer relies on the principle of pulse shape analysis using a database of simulated detector signals. In order to ensure that the simulated signals accurately represent the true response of the detector a detailed understanding of the physical processes leading to an observed signal must be developed. This leads us to consider the interaction of radiation with the detection medium, the production and collection of a signal carriers within the medium, and the processing of the signal by electronic instrumentation associated with the detector.

2.1 The Interaction of Gamma Rays with Matter

Most radiation detectors, including semi-conductor and scintillator based devices, rely on ionisation produced by the deposition of energy within their sensitive volume by radiation quanta. In the case of gamma rays, as they have no mass or charge, they do not directly ionise a material as they pass through it but have a finite probability of undergoing an interaction with an atomic electron for each unit length of material through which they pass. When an an interaction occurs, the electron will move through the detector material producing additional ionisation until it has lost all of its energy. The range of an electron in the detector depends on its energy and the density of the detector material. For typical gamma-ray energies in germanium, electron ranges are less than 1mm [Muk76]. There are a variety of mechanisms by which a gamma ray may transfer energy to an electron, and consideration of each of these permits an understanding of the features seen in a typical

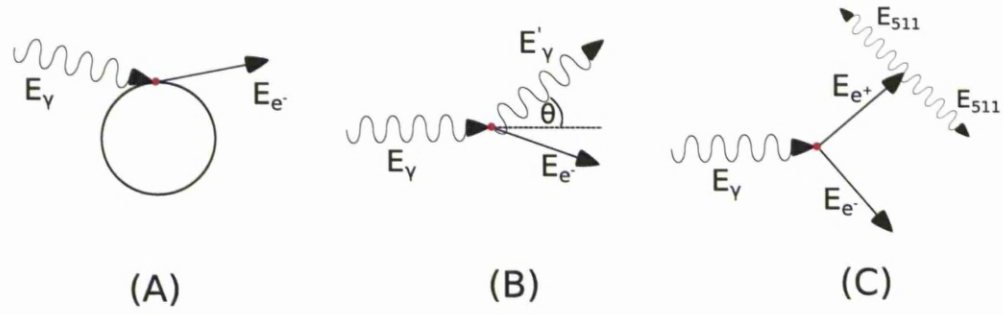

Figure 2.1: Photon interactions at gamma-ray energies, (A) *Photoelectric Absorption*, where a gamma ray disappears and transfers its full energy to an atomic electron, (B) *Compton Scattering*, where the gamma ray scatters from a loosely bound atomic electron transferring part of its energy, and, (C) *Pair Production* where, within the Coulomb field of a nucleus, a gamma ray photon is converted to an electron-positron pair.

gamma-ray spectrum.

Only those interaction mechanisms which deposit energy within the material and have a significant cross-section at gamma-ray energies are important for radiation detection. Three processes fulfil these criteria, *photoelectric absorption*, *Compton scattering* and *pair production*; others such as *Rayleigh scattering* and *Photo-nuclear reactions* will not be considered here. The total attenuation of a gamma-ray flux by some material can be considered to arise from the sum of the attenuation due to each of these interactions,

$$\mu_{Total} = \mu_{PE} + \mu_{CS} + \mu_{PP} \tag{2.1}$$

Here, μ is the *linear attenuation coefficient*. The fraction of photons which will interact in a given thickness of material is then given by *Equation 2.2*.

$$\frac{I}{I_0} = e^{-\mu t} \tag{2.2}$$

where I_0 is the incident gamma-ray flux, I is the flux after the absorbing material and t is the length of the path through the material.

2.1.1 Photoelectric Absorption

Photoelectric absorption, *Figure 2.1 A*, is an interaction in which a gamma-ray photon transfers its total energy to an atomic electron. The electron is ejected from the atom with a kinetic energy given by,

$$E_{e^-} = E_\gamma - E_b \tag{2.3}$$

where E_b is the binding energy of the atomic shell. At gamma-ray energies, it is most probable that the photoelectron will come from the most tightly bound, K-shell, in Germanium this amounts to a binding energy of ≈12 keV. The photoelectron then moves through the detector and, due to its electric charge, quickly transfers its excess energy to other nearby atomic electrons. The vacant orbital left by the photoelectron is quickly filled by a free electron or by rearrangement in the electron shells, resulting in the release of an X-ray photon. In the general case, this X-ray is quickly reabsorbed but for small detectors there is a significant chance of it escaping which can influence the resulting measured energy.

The probability of photoelectric absorption is dependent on the gamma-ray energy and the atomic number, Z, of the absorbing material. *Equation 2.4* gives an approximation of the relationship.

$$\mu_{PE} \propto \frac{Z^n}{E_\gamma^{3.5}} \tag{2.4}$$

where μ is the absorption probability and n varies between 4 and 5, depending on E_γ [Kno10]. In Germanium (Z = 32), photoelectric absorption is the dominant interaction process for gamma-ray energies up to 200 keV.

2.1.2 Compton Scattering

Compton Scattering takes place when a gamma ray scatters from an atomic electron and transfers only part of its energy. An incident gamma ray with energy E_γ scatters from an atomic electron through an angle θ, this is shown schematically in *Figure 2.1 B*. The energy of the incoming gamma ray is shared between the outgoing gamma ray and the scattered electron. Due to the conservation of energy and momentum, the energy split is fixed for any given scattering angle and is given by,

$$E'_\gamma = \frac{E_\gamma}{1 + \frac{E_\gamma}{m_0 c^2}(1 - cos\theta)} \tag{2.5}$$

The probability for Compton scattering increases linearly with Z due to the increasing number of electrons as potential scattering targets, and falls with increasing gamma energy. In germanium, Compton scattering is the dominant interaction mechanism for photons of $/approx$0.2-7.5 MeV.

The distribution of angles through which gamma rays are scattered is dependent on Z and E_γ, the differential scattering cross section, $d\sigma/d\Omega$, is given by the *Klein-Nishina formula*,

$$\frac{d\sigma}{d\Omega} = Zr_0^2\left(\frac{1}{1 + \alpha(1 - cos\theta)}\right)^2\left(\frac{1 + cos^2\theta}{2}\right)\left(1 + \frac{\alpha^2(1 - cos\theta)^2}{(1 + cos^2\theta)[1 + \alpha(1 - cos\theta)]}\right) \tag{2.6}$$

where $\alpha = E_\gamma/m_0c^2$ and r_0 is the classical electron radius.

Figure 2.2, shows how the cross section predicted by *Equation 2.6* varies with angle and the energy of the incident gamma ray. The cross sections have been normalised so that $d\sigma/d\Omega = 1$ at $\theta = 0$. At low energy, scattering is close to isotropic, with a small reduction in scattering probability at 90°, but as energy increases the distribution becomes increasingly forward focused.

2.1.3 Pair Production

Gamma rays with energy >1022 keV may interact in the Coulomb field of a nucleus to convert their energy into an electron-positron pair. The incident gamma ray disappears and its energy is transformed into the rest mass of the electron-positron pair (511 keV each), any additional energy being shared between the two particles as kinetic energy. The two charged particles will then deposit the rest of their energy within a relatively small range ($< 1mm$) and, in the case of the positron, annihilate with a nearby electron releasing the rest mass as two, back-to-back, 511 keV gamma rays. This process is illustrated in *Figure 2.1 C*. The probability of pair production varies in a complicated manner, but is approximately proportional to the square of the atomic number of the absorber. The probability is small for gamma-rays below 2 MeV but, in germanium, it becomes the dominant interaction process above 7.5 MeV.

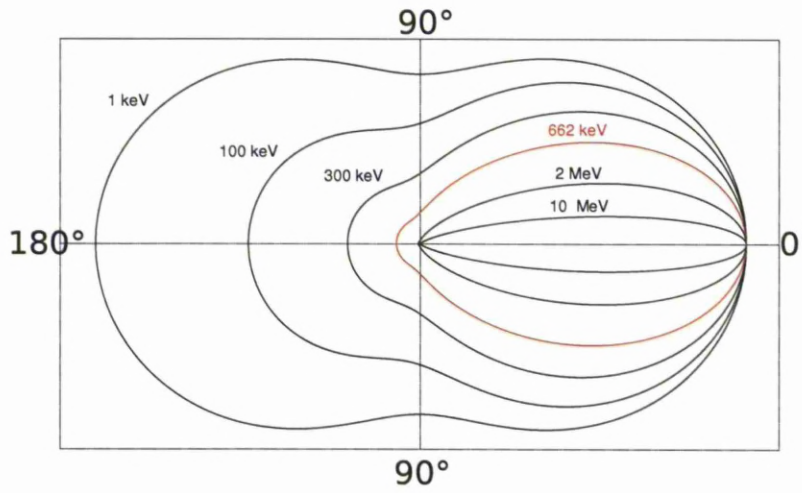

Figure 2.2: A polar plot of the differential cross section for Compton scattering as a function of scattering angle for a selection of gamma-ray energies, as described by the Klein-Nishina formula (*Equation 2.6*). Values calculated for scattering from germanium (Z = 32) and are normalised to $\theta = 0$.

2.2 Semi-Conductors as Radiation Sensors

The unique properties of semi-conductor materials make them an ideal tool for converting the ionisation produced by gamma rays into a measurable electrical signal. In addition they typically provide a higher density, and hence stopping power, relative to other commonly used detectors, e.g. gas ionisation chambers.

2.2.1 Band Structure

The wave function of an electron in a crystalline solid is not restricted to the same discrete energy levels of an isolated atom. Solving the *Schrödinger equation* for an electron in a periodic potential results in broad bands of allowed energy. Electrons in the lower, *valence band*, are involved in the bonds between neighbouring atoms in the atomic lattice and as such are unable to move freely through the material. Conversely, electrons in the higher, *conduction band* are not bound to any particular atom and can move freely through the

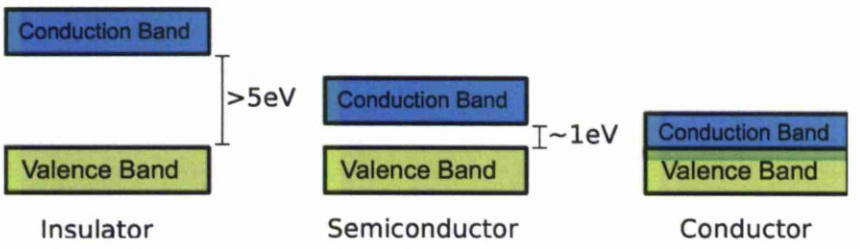

Figure 2.3: A simplified depiction of allowed electron energy bands for Insulators, Semiconductors and Conductors.

crystal lattice.

In the case of a conductor, there is either an overlap between the bands or the valence band is not completely filled; this means there are always electrons free to carry charge through the material. *Insulators* and *semiconductors* have a gap, E_g, between the bands which means an electron must gain enough energy to enter the conduction band before it can move through the crystal (*Figure 2.3*).

In the absence of impurity atoms in the crystal or thermal excitation, insulator and semiconductor materials have a full valence band and unoccupied conduction band. The large band gap in insulating materials means there is a very low probability for thermal excitation of an electron to the conduction band, this results in the high resistivity of insulating materials. In a semiconductor however E_g is small enough (0.665 eV in Ge, 1.165 eV in Si) that thermal excitation can be significant.

When an electron is excited to the conduction band, it leaves behind a vacancy, called a *hole*, in the conduction band (*Figure 2.4*). In the presence of an electric field, a neighbouring valence electron can move to fill this hole leaving another hole behind. In this manner holes can also serve as a means of conducting electric current through the material.

It is also possible to produce electron-hole pairs through ionisation induced by incident radiation; it is this that serves as the basis for gamma-ray detection with semiconductor devices.

2.2.2 The p-n Junction

If a semiconductor is entirely pure then there must always be exactly as many electrons in the conduction band as there are holes in the valence band; such a material is called an

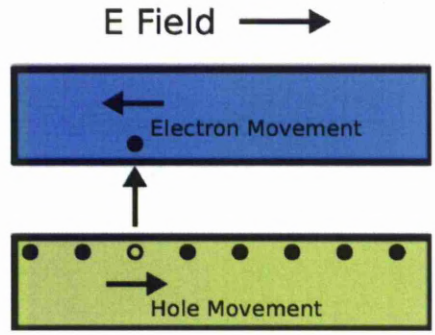

Figure 2.4: An electron excited from the valence to conduction bands allows current to be carried through the material, the vacancy or *hole* remaining in the valence band can also act as a means of conduction as an electron from nearby moves to take its place.

intrinsic semiconductor. Such levels of purity cannot however be achieved in practice and the electrical properties of real-world semiconductor materials are dominated by a small proportion of electrically active impurities.

Both silicon and germanium are Group IV elements having a tetrahedral crystal structure, each atom forms a bond with four nearest neighbours. If there is an impurity atom present from group III or V it will leave an unsaturated bond in the structure. In the case of a group V impurity, e.g. phosphorus, there will be an excess electron which sits at a 'donor' energy level just below the conduction band and is easily excited by thermal energy. Conversely if a group III impurity, e.g. boron, is present it will leave an unsaturated bond at an 'acceptor' level, just above the valence band, which allows an electron to be easily excited from the valence band leaving a hole available for conduction.

Typically, there will be impurities of both types present however one of the two will dominate the electrical properties. If there are more donor impurities, the extra electrons will move to fill any acceptor sites in the lattice and if there are more acceptors then any free electrons will move to fill these sites. A material with an excess of donor impurities is known as *n-type*, as the impurities provide negative electrons for conduction while a material with an excess of acceptor impurities is known as *p-type*, due to the positive holes available for conduction.

If there is a good thermodynamic contact at the junction of n-type and p-type semi-

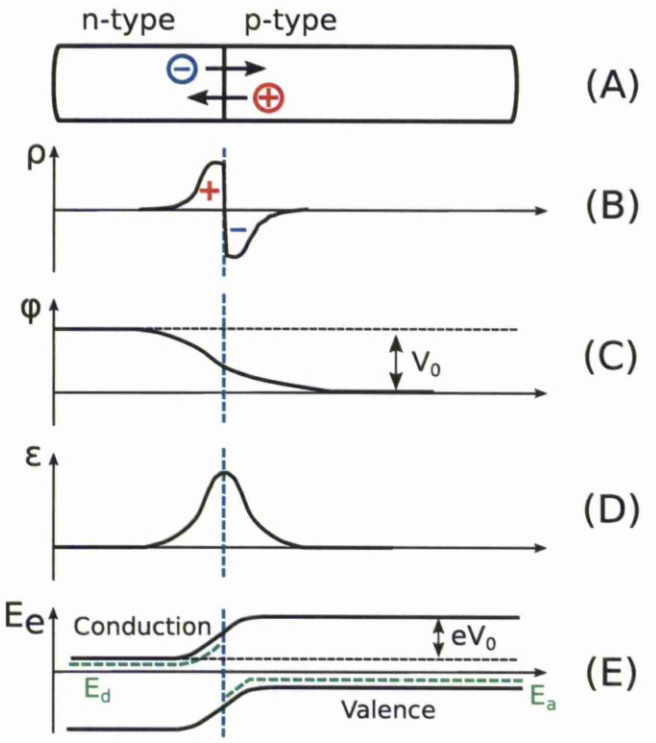

Figure 2.5: (A) A schematic of a ideal p-n junction showing the direction of hole and electron migration due to diffusion pressure. (B-D) The space charge density, electric potential and electric field respectively as a function of position across the junction when it is in equilibrium. (E) Electron energy as a function of position showing the allowed bands of energy and the energy of states provided by donor (E_d) and acceptor (E_a) impurities

conductors then the excess of charge carriers results in diffusion of electrons across the boundary, *Figure 2.5 A*. Electrons will drift across the boundary until the resulting net charge density creates an equilibrium with the drift across the boundary in one direction due to diffusion, exactly balanced by the drift in the other direction due to the electric field. As electrons move through the material, they will pair up with holes in the p-type material in a process known as *free charge annihilation*, which results in a net positive charge in the n-type material and net negative charge in the p-type material. The material either side of the junction, which no longer has any free charge carriers available for conduction, is known as the *depletion region*. The variation in space charge density (B), electric potential (C), and electric field (D), are shown in *Figure 2.5*, the greatest rate of change of charge density

and potential is found directly at the boundary and hence this is where the electric field is at a maximum. The potential across the junction at equilibrium is known as the *contact potential*, V_0.

The effect of this charge migration on the band structure of the material is shown in *Figure 2.5 (E)*, the net positive charge on the n-type side lowers the energy for electrons while the negative net charge on the p-type side has the opposite effect.

If an external potential is applied to the junction, in opposition to the contact potential (*forward bias*), the charge carriers will migrate back across the junction, closing the depletion region and allowing a conventional current to flow through the junction from the p-type to n-type material. Alternatively, if a *reverse bias* is applied, charge will be pulled further across the junction, widening the depletion region and eventually depleting the whole material of free charge carriers. This is the basis of the operation of a p-n junction diode.

A semiconductor radiation detector is operated as a p-n junction under reverse bias. In the absence of any ionising radiation, there are no free charge carriers in the detector and only a small leakage current due to surface effects can flow. If, however, incident radiation deposits energy in the detector it will excite electrons across the band gap producing electron-hole pairs which are swept by the high electric field to the detector contacts. The mean energy required to produce an electron-hole pair is constant for any given semiconductor and is determined by the band gap and, as such the total amount of charge collected at the contacts will be proportional to the deposited energy.

In any real detector there will be a small leakage current even in the absence of any incident radiation. This is the result of thermal excitation, residual minority charge carrier movement and surface effects; the total magnitude is of the order of nanoamps in a HPGe detector.

2.2.3 HPGe Detectors

Since the widespread availability of high-purity Germanium in the early 1980s, HPGe detectors have been the first choice for gamma-ray spectroscopy due to their high stopping power, large volume, and unrivalled energy resolution. Stopping power in radiation detectors is proportional to atomic number, Z, the probability for a photoelectric interaction in

particular is proportional to $Z^{\approx 4}$. While there are many detector materials with a higher Z than germanium they have significant drawbacks. High Z scintillator detectors such as bismuth germanate (BGO) have very poor energy resolution due to the relatively small number of information carrying particles produced per unit of deposited energy. Some high Z compound semiconductors such as cadmium zinc telluride (CZT) have an energy resolution much closer to that of HPGe, but they are difficult to produce in large volume due to the complex crystal structure.

A major contribution to the uncertainty on energy measured in a semiconductor detector is the statistical fluctuation in the number of electron-hole pairs produced for a given amount of deposited energy. The process of charge carrier production obeys Poisson counting statistics, such that, if N charge carriers are produced, the standard deviation on N, σ_N is equal to $\sqrt{N}$. As such, the fractional uncertainty drops with increasing N, meaning that more charge carriers equates to a smaller uncertainty on the energy. As germanium requires less energy to produce an electron-hole pair than any other semiconductor detector it has unrivalled energy resolution.

The Poisson model for charge carrier production assumes that the production of each electron-hole pair is an independent event which does not effect the probability of the production of another pair. In reality there are correlations in charge production which lead to lower than predicted energy resolutions. The *Fano factor* is the ratio of the observed statistical variance in the number of charge carriers to that predicted by the Poisson distribution. A complete model of the charge production process that would allow calculation of the Fano factor does not yet exist.

Table 2.1 compares some of the properties of silicon and germanium which are relevant to their use in radiation detection. It is important to note that the energy to create an electron-hole pair in Germanium is low enough that, at room temperature, there is significant thermal excitation of electrons into the conduction band. If bias was applied to an HPGe detector at room temperature, the leakage current due to this thermal excitation would be so great as to hide any signal due to radiation and make the detector unusable. For this reason, it is necessary to cool the detector crystal to liquid Nitrogen (LN_2) temperature, ($\approx$77K) before use.

Semiconductor detectors must be manufactured from single crystals as the borders be-

	Si	Ge
Atomic number	14	32
Atomic Weight	28.09	72.60
Stable isotopes	28, 29, 30	70, 72, 73, 74, 76
Density (300K); g/cm^3	2.33	5.32
Atoms/cm^3	4.96×10^{22}	4.41×10^{22}
Dielectric constant (relative to vacuum)	12	16
Forbidden energy gap (300K); eV	1.115	0.665
Forbidden energy gap (0K); eV	1.165	0.746
Intrinsic carrier density (300K); cm^{-3}	1.5×10^{10}	2.4×10^{13}
Electron mobility (300K); cm^2/Vs	1350	3900
Hole mobility (300K); cm^2/Vs	480	1900
Electron mobility (77K); cm^2/Vs	2.1×10^4	3.6×10^4
Hole mobility (77K); cm^2/Vs	1.1×10^4	4.2×10^4
Energy per electron-hole pair (300K); eV	3.62	
Energy per electron-hole pair (77K); eV	3.76	2.96
Fano factor (77K)	0.084 - 0.16	0.057 - 0.129

Table 2.1: Table comparing properties of Silicon and Germanium relevant to their use in radiation detection [BC68]. A range of Fano factor values are stated in the literature as there is a large variation in reported measurements due to the difficulty in accounting all other sources of uncertainty in the number of charge carriers, the range of typical values is shown here.

tween individual crystals in polycrystalline material would act as trapping sites, impeding the proper collection of charge carriers. Germanium crystals have a *face centred cubic* structure which is arranged such that there is one atom at each vertex of a cube and one atom in the centre of each face. *Miller indices* [Kit04] can be used to describe different directions through the crystal, *Figure 2.6*. Crystal orientation is important to the modelling of electron and hole collection as the electrical properties of a crystal vary as a function of direction, this will be discussed further in Chapter 3.

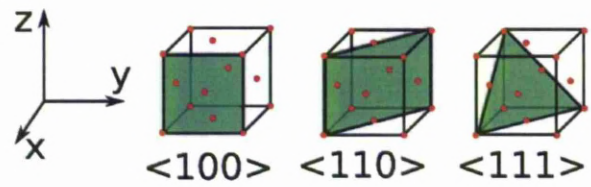

Figure 2.6: Schematic representation of a face-centred cubic unit cell as seen in Germanium crystal structure. The planes described by the Miller indices <100>, <110> and <111> are indicated.

2.2.4 HPGe Detector Fabrication

Early Germanium semiconductor detectors were doped with Lithium in order to compensate for the natural p-type impurities which allowed, for the first time, the depletion of large volume Germanium diodes for radiation detection. These devices, known as Ge(Li) detectors were a major step forward for gamma-ray spectroscopy but had the disadvantage of having to be stored, as well as operated, at liquid nitrogen temperature in order to prevent the diffusion of the Lithium ions, which are highly mobile in the crystal lattice, from the crystal [ES08].

The thickness of germanium that can be depleted with a certain applied bias is inversely proportional to the impurity concentration. In order to produce HPGe detectors of appreciable volume, the material must be refined to very high levels of purity, of the order of $10^{10} atoms/cm^3$. This level of purity became practically achievable in the 1980s with the introduction of *zone refining* techniques to detector fabrication. This process begins with bulk Germanium of already high purity which is then processed by slowly passing a heating coil, repeatedly along the length of the crystal. As the Germanium under the coil melts, impurities are preferentially dissolved in the liquid and swept along with the coils, resulting in the majority of impurities being concentrated at one end of the material which is then removed.

Once zone refining is complete the purified material is used to grow a large single crystal from a small seed crystal which determines the orientation of the crystal axis. The small number of impurities that remain tend to distribute themselves such that one end has a majority of n-type impurities and the other end has a majority of p-type. The majority carrier type of a finished detector depends on which part of the crystal they are cut from,

all AGATA detectors are manufactured from n-type high-purity germanium.

After crystal growth is complete the crystal is ground into the required shape, the hole for the central contact is drilled and n and p-type contacts are applied to the detector. *Lithium drifting* is use to produce the n-type contact, due to the high mobility of lithium ions in the germanium crystal this produces a dead layer of $\approx 600\mu m$ as the dopant diffuses into the crystal. The p-type contact is produced by *boron implantation* which produces a much thinner dead layer ($\approx 0.3\mu m$). The contact types are chosen according to the majority carrier type in the crystal such that the p-n junction is formed at the outer surface, this results in increased efficiency of n-type detectors for low energy gamma rays as there is a smaller dead layer to penetrate before reaching the sensitive volume.

Once the crystal fabrication process is completed, crystals for the AGATA project are encapsulated in a 0.5mm aluminium casing, called a capsule. Aluminium is used because of its low Z which reduces the effect on detector efficiency. The capsule is then provided to the AGATA collaboration for assembly into a cryostat and testing. Encapsulating crystals in this manner allows them to be handled outside of a clean room without contamination at the cost of a very small reduction in efficiency for photons of low energy.

2.3 Electronics

In order to operate a detector it must be coupled with electronics components to process and record the charge produced. In earlier generations of detector the only pieces of information to be extracted from the signal were energy and time, this meant the signal could be processed in such a way as the shape of the pulse was destroyed. If PSA is to be used to extract the position of interaction however, it is necessary to preserve the signal shape as much as possible. Although care has been taken when designing the electronics associated with AGATA to maintain the signal shape and record it as accurately as possible, some distortion is inevitable however and as such this must be accounted for.

2.3.1 Preamplifier

The total amount of free charge produced in a detector by a typical gamma-ray interaction is too small to be accurately measured. In order to raise the magnitude of the signal to an

appreciable level, and minimise the effect of electronic noise picked up between the detector and measurement electronics, preamplifier circuitry is employed.

A good preamplifier for radiation detection will be charge sensitive, have a high gain and low noise. If the signal shape is to be investigated a high bandwidth is also necessary to allow as large a range of frequency components to pass as possible.

The design and response of the AGATA preamplifier [PZP06] as well as a correction to the simulated signal basis will be discussed in *Chapter 3*.

2.3.2 Digitisers

If PSA is to be implemented on a detector, the rising edge of the signal must be digitised with a sufficient resolution and sampling rate to extract information on the charge collection process. Several VME based flash ADC cards have been designed for this purpose including the GRT4 card [LAB+03], the GRETINA digitiser card [DJYZ06]. These cards are optimised for the purposes of PSA with HPGe detectors with high sampling rates of 80-100MHz and 14 bit resolution but they will still have an effect on the signal shape which must be considered. All of the cards mentioned above are fitted with a NYQUIST filter to remove frequency components greater than half of the sampling frequency to remove any aliasing effects, this filter must be considered if the observed signal shape is to be understood.

The completed AGATA array will use a dedicated digitiser designed specifically for the project, the performance specifications of this device are similar to the GRETINA digitisers used in this work.

2.3.3 Crosstalk

Within the detector crystal and associated electronics there is a capacitive coupling between individual channels. This results in *crosstalk* between the channels whereby a real signal on any channel can produce an induced transient signal on each of the others. The shape of the induced signal has two components, one proportional to the magnitude of the real signal and one proportional to the differential of this signal. Electronics can be designed and shielded in order to minimise this effect, but it cannot be eliminated. A full characterisation of the crosstalk in an AGATA detector will be performed in *Chapter 6*.

Chapter 3

Electric Field Simulations

PSA in AGATA requires the creation of a pulse-shape database describing the signal shape produced by interactions at points throughout the detector's volume. Such a database can be produced experimentally, a method for achieving this is described in *Chapter 5*, but the rate of data collection is low due to the collimation and coincident triggering involved. A typical measurement with the Liverpool scanning system requires two months to collect enough data for 2000 positions [DBC+09] and a full signal basis on a 1mm grid will contain approximately 300,000 points for each AGATA crystal.

Several of the factors that determine the signal shape, in particular the crystal axis orientation and the impurity concentration, are dependent on the individual crystal. This means that a customised basis is required for each and the time required to produce experimental basis for all 180 AGATA crystals is prohibitive and effectively rules that out as a large-scale characterisation method.

There are a number of new scanning techniques which promise to increase the speed with which an experimental basis can be produced. The Orsay scanning system [AAA+11], [Ha09] is a coincidence scanning system which increases the data acquisition rate by scanning a larger number of positions simultaneously. Also, a new method of experimental characterisation has been developed, the *Pulse Shape Comparison Scan* (PSCS) [CCM+08], which promises to allow a full basis to produced in $\approx$1 week. This method is based on the comparison of signal shapes from two scans with single trigger conditions and orthogonal collimation directions. Data were collected in Liverpool from AGATA C001 using this scanning mode and collaborators in the Milano University are conducting the analysis. These

novel methods are in the development stage however and will not be considered in this work.

The alternative approach is to use an electric field simulation to calculate the required signal basis, this allows for the construction of a complete 1mm signal basis in days on a modern desktop PC or much faster if large array of parallel processors can be employed. In this chapter the basic principles of electric field simulation will be outlined, some of the results from two different simulations developed for AGATA will be discussed, and a preamplifier response function for those simulations will be described.

3.1 AGATA Simulation Packages

The *Multi Geometry Simulation* (MGS) [MSV04] is a general purpose simulation, capable of modelling any geometry of HPGe detector, it was the first simulation package developed for AGATA. It uses the *MATLAB* matrix-based programming environment for all of its calculations but it can be compiled as a stand-alone program using the freely available MATLAB library packages. A limitation of MGS is the fixed grid size, all field calculations are performed on a uniform 1mm grid of points. This approach works well for the bulk volume of the detector but results in significant errors close to the contacts where the electric field is changing rapidly.

The *Java AGATA Signal Simulation* (JASS) [Sch09b] was developed specifically for the AGATA detector geometries using the *Java* programming language. It can be run on any computing platform compatible with the *Java Virtual Machine* (JVM). JASS allows the initial grid size used for field calculations to be specified by the user and also performs 'on-the-fly' interpolation during the charge transport simulation. For this work a 0.5mm grid was used for the initial field calculations.

Figure 3.1 shows the basic steps involved in calculating the signal shape. The detector geometry and the impurity distribution are used to calculate the electric field through the solution of *Poisson's Equation*. The trajectory of the charge carriers can then be calculated from the electric field and crystal axis orientation. Shockley-Ramo theorem is used to calculate the *weighting field* for each contact from the detector geometry. Finally, knowledge of the charge trajectory and weighting fields allows the signal induced on each contact to be derived.

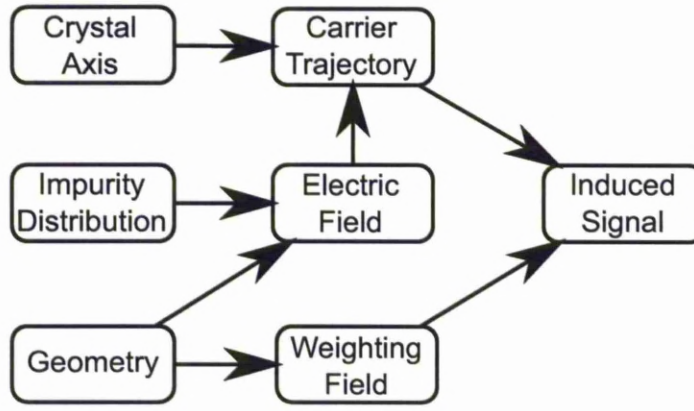

Figure 3.1: Flow chart showing the basic steps used to compute the expected signal shape. The detector geometry and the impurity distribution are used to calculate the electric field, this can be combined with the crystal axis orientation to calculate the trajectories of charge carriers following an interaction. Shockley-Ramo theorem is used to calculate the weighting field, for each contact, from the detector geometry. Finally, knowledge of the charge trajectory and weighting fields allows the signal shape to be derived.

3.2 Electric Field Calculation

The first stage in pulse-shape simulation is the calculation of the electric field inside the detector, this is determined by the geometry, applied voltage and space charge distribution. The field can be calculated by first determining the electric potential using *Poisson's equation*,

$$\nabla^2 \Phi\left(\vec{r}\right) = -\frac{\rho\left(\vec{r}\right)}{\epsilon}, \tag{3.1}$$

where $\Phi\left(\vec{r}\right)$ is the electric potential, $\rho\left(\vec{r}\right)$ is the space charge density at position $\vec{r}$, and ϵ is the dielectric constant of the material. If the volume of the detector has been fully depleted of charge carriers then the space charge density, $\rho\left(\vec{r}\right)$, will be equal to the impurity concentration at that point. When HPGe crystals are supplied to the AGATA collaboration, the impurity concentrations at the front and back faces are provided by the manufacturer, a linear gradient is then assumed between the faces and the radial distribution is assumed to be flat. Boundary conditions are imposed on solution by the contact potentials.

A simple analytical solution to *Equation 3.1* can only be found if symmetry can be used

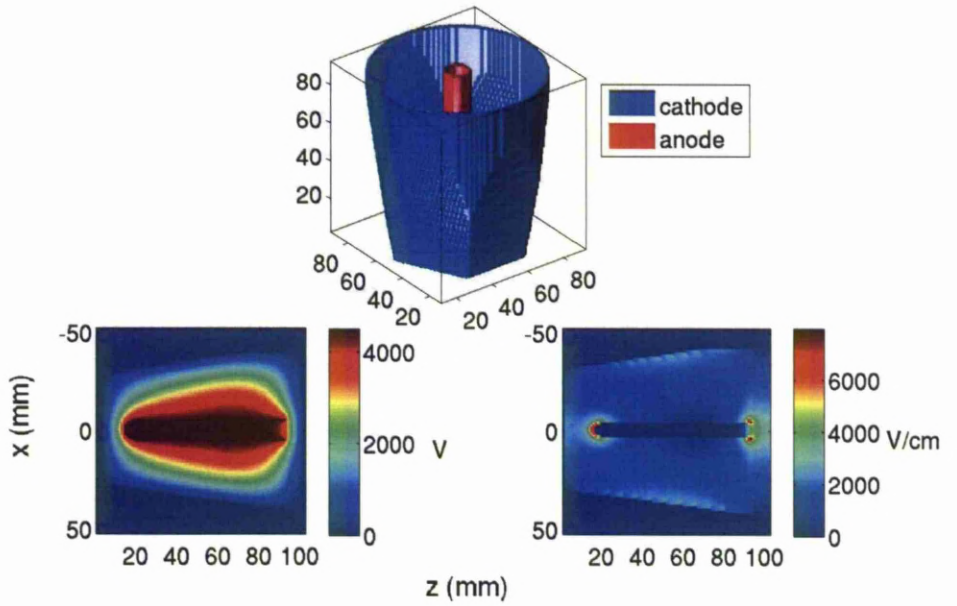

Figure 3.2: The geometry (top), electric potential (left) and electric field (right) of AGATA crystal C001, as determined by MGS

to simplify the mathematics, for a complex geometry like an AGATA detector a numerical approach must be used. Both MGS and JASS approximate the continuous fields on a finite grid and then use iterative methods to minimise the error between the grid and the 'true' solution.

MGS uses two methods, first *Successive Over Relaxation* (SOR), which is a fast algorithm with limited accuracy, and then *Relaxation* [PTVF07] to converge on the final solution. JASS uses the *Red-Black Gauß-Seidel* algorithm [Sch09b] due to its excellent memory efficiency.

Once the electric potential has been calculated the field can be determined from the gradient of the potential. *Figure 3.2* shows the geometry of AGATA crystal C001 and slices through the electric potential and field, as determined by MGS.

3.3 Charge Trajectory Calculation

In the presence of an electric field, electrons in the conduction band and holes in the valence band will undergo a net drift through the crystal. For low values of electric field the velocity

of this drift is proportional to the electric field and to the charge carrier mobility,

$$\vec{v_e} = -\mu_e \vec{E},\ \vec{v_h} = -\mu_h \vec{E}, \tag{3.2}$$

where μ_e and μ_h are the electron and hole mobilities respectively, in germanium the mobility of holes is systematically less than that of electrons resulting in slower drift velocities. As the electric field is increased however the drift velocity begins to deviate from this *Ohmic* behaviour and the velocity plateaus. This behaviour across a range of field strengths can be described by,

$$v = \frac{\mu_0 E}{\left(1 + \left(\frac{E}{E_0}\right)^{\beta}\right)^{\frac{1}{\beta}}} - \mu_n E, \tag{3.3}$$

where E is the electric field strength and μ_0, E_0 and β are experimentally determined constants. *Equation 3.3* is based on the parametrisation given by [RBP82] and [OR87] but with an added term $-\mu_n E$ to account for the *Gunn effect* which causes negative differential mobility of electrons at high fields [MGL+00].

At low field strengths the mobility of charge carriers is isotropic, as the field increases however it has long been observed that electron [Nat63] and hole [RCNO77] mobilities depend on the direction of motion relative to the crystal axis. This anisotropy of carrier requires that the scalar value of μ_0 be replaced with a tensor term to account for the angular variation.

The origin of this anisotropy lies in the band structure of the crystal. The tetrahedral structure of the germanium lattice has varying atomic spacing as the angle of a slice taken through the lattice changes. The periodic potential of the lattice thus varies as a function of angle, resulting in a different band structure for different directions of the electron wave vector, this is illustrated in *figure 3.3*.

The electron and hole mobilities, together with the other parameters required by *Equation 3.3*, have been measured by a number of investigators, the results are summarised in *Table 3.1*. *Figure 3.4* shows the velocity calculated from *Equation 3.3* using each set of parameters as a function of electric field strength. There are significant differences in the final values between the different data sources, particularly in the electron velocities, this is expected to be due to systematic errors in the measurements and definitive values have

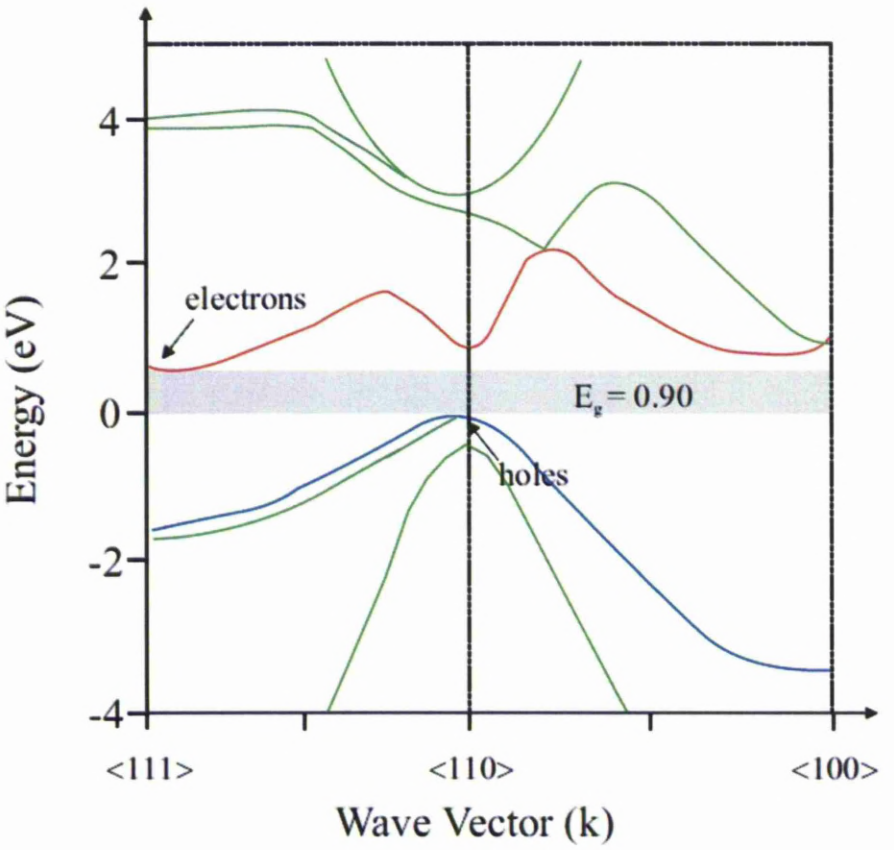

Figure 3.3: The band structure of germanium for different crystal axes. The blue line shows the maximum of the valence band while the red line shows the minimum of the conduction band. Germanium is an indirect semiconductor as the smallest energy gap between the bands requires a change in momentum.

yet to be established. Both JASS and MGS use the parameter values given by [MGL+00] and [RCNO77].

3.4 Signal Calculation

Once the trajectory of charge carriers is known, the remaining problem is to calculate the charge, Q, induced on each of the electrodes by the moving charge, q, as a function of time. A naive approach to this problem is to break the charge collection process into a

Data Source	Charge Carrier	μ_0 (cm^2/Vs)	β	E_0 (V/cm)	μ_n (cm^2/Vs)
		<100>			
[MGL+00]	e^-	40180	0.72	493	589
[BRP06]	e^-	38609	0.805	511	-171
[RCNO77]	h^+	66333	0.744	181	-
[BRP06]	h^+	61824	0.942	185	-
		<111>			
[MGL+00]	e^-	42420	0.87	251	62
[BRP06]	e^-	38536	0.641	538	510
[RCNO77]	h^+	107270	0.580	100	-
[BRP06]	h^+	61215	0.662	182	-

Table 3.1: Parameters for the calculation of charge carrier drift velocity in the <100> and <111> direction using *Equation 3.3*. The inconsistencies between the different data sources are expected to be due to systematic experimental uncertainties, no definitive measurement of these has yet been published. Both of the simulations investigated here, JASS and MGS, have adopted the parameters given by [MGL+00] and [RCNO77].

large number of small time intervals and calculate the charge induced at each interval using *Gauss' Law*,

$$Q = \oint_S \epsilon \vec{E} \cdot d\vec{S}, \tag{3.4}$$

where the integral is performed over the surface on the electrode being considered. While this method is sound, it requires the instantaneous electric field to be recalculated at each position which is computationally very expensive.

An alternative approach, *Shockley-Ramo Theorem* [Ram39], was developed for the calculation of induced charge in vacuum tubes, but its validity has also been demonstrated for systems where there is stationary space-charge present [He01]. The method gives the charge, Q, and current i induced on an electrode as,

$$Q = -q\varphi_0(\vec{x}), \tag{3.5}$$

and,

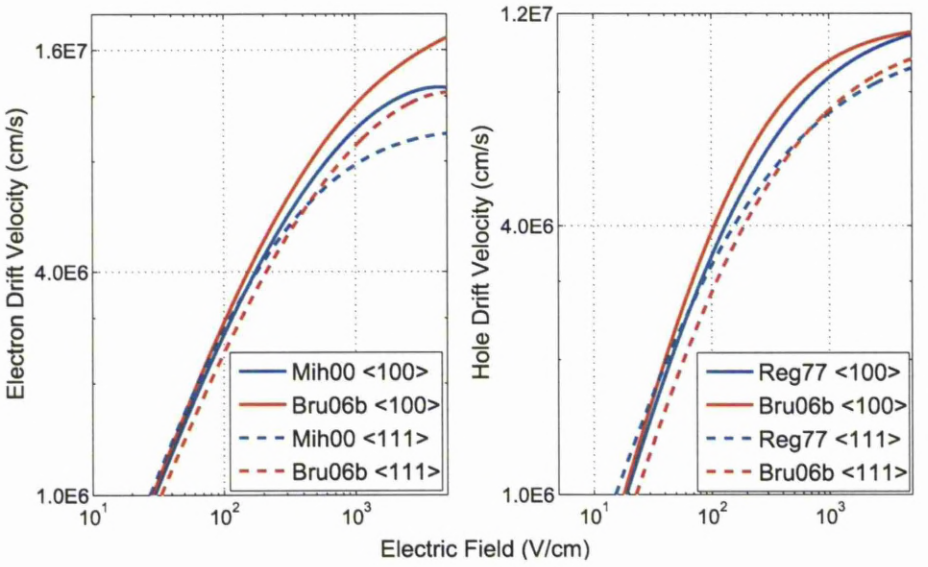

Figure 3.4: Drift Velocities for electrons (left) and holes (right) in germanium. The values shown on the plot have been evaluated using *Equation 3.3* with parameters taken from [MGL+00], [BRP06] and [RCNO77]. At low field strengths the velocity is proportional to the applied field and similar for <100> and <111> axes, as the field is increased the values for each axis diverge and the velocity for each plateaus.

$$i = q\vec{v} \cdot \vec{E}_0(\vec{x}) \tag{3.6}$$

where $\vec{v}$ is the velocity of charge q and $\varphi_0(\vec{x})$ and $\vec{E}_0(\vec{x})$ are the *weighting potential* and *weighting field* respectively. The weighting field and potential are derived for each electrode by calculating the electric field and potential that would exist under the following conditions:

- The electrode being considered is at unit potential.
- All other electrodes are at zero potential.
- All charges are removed from the detector.

Once the weighting potential has been calculated for each electrode, the induced signal can evaluated from *equation 3.5* at each position along the charge carrier trajectory calcu-

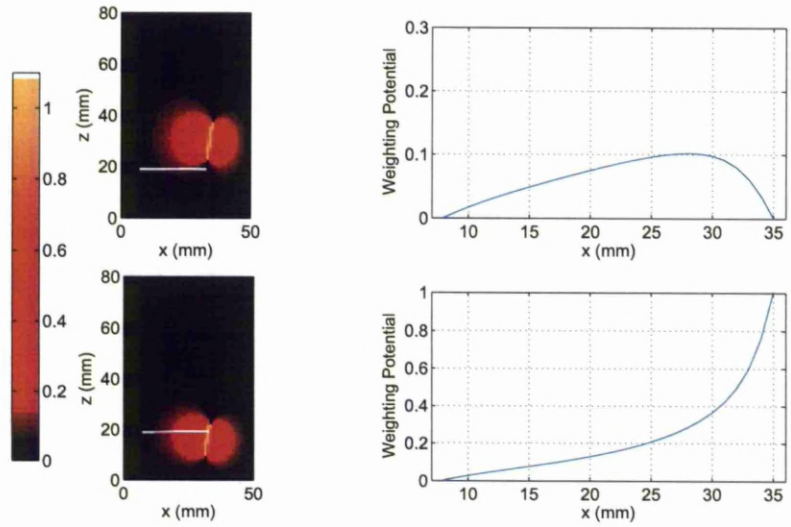

Figure 3.5: The weighting potential calculated by MGS (left) for AGATA segments A2 (bottom) and A3 (top), the white lines indicate the same positions on both. The values of the potentials at positions along the white line (right). The charge induced on a contact by a moving charge in the detector is proportional to the change in weighting potential along its trajectory. If a charge were to move along the line indicated in the plots, it would induce a real charge signal in segment A2 and a transient image charge signal on segment A3.

lated earlier. *Figure 3.5* shows the weighting potential calculated by MGS for two segments A2 and A3 in an AGATA crystal, a path through the detector is indicated in white. If a charge were to move along the indicated line, it would induce a real charge signal on segment A2 and a transient image charge signal on segment A3.

3.5 Preamplifier Correction

The AGATA preamplifier [PZP06], *figure 3.6*, is a fast low-noise hybrid charge-sensitive design, conceived specifically for use in highly segmented position-sensitive detectors. The amplifier has a gain of 100 mV/MeV, includes a fast-reset de-saturation circuit to minimise system dead time, and has a differential output for low-noise transmission to the digitiser stage.

Although every effort has been made to minimise the effect of the preamplifier on the

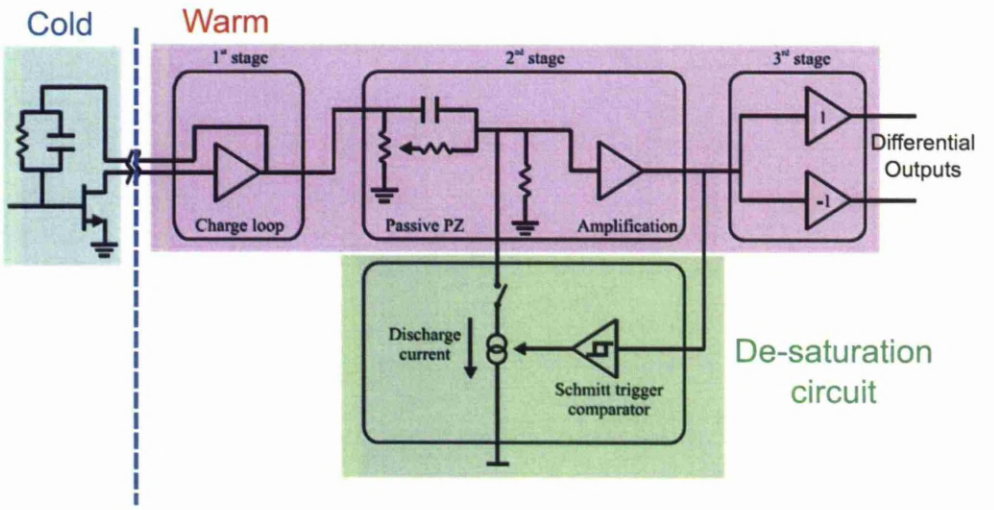

Figure 3.6: The design of the AGATA preamplifier. The cold section of the device is located inside the AGATA cryostat with the circuitry for six detector channels mounted on a single copper cooling block. The warm components are located directly behind the cryostat in the AGATA detector module with three channels mounted on a single PCB.

shape of the charge pulse leading edge, there is inevitably some degree of distortion which must be reproduced in the simulated signal basis. The simplest effect to be considered is the exponential decay of the signal height as a result of the discharging capacitor. The time constant for this decay is determined by the values of the resistor and capacitor in the preamplifier's feedback loop, for AGATA segments this is set at 50 μs. The central contact is required to run at a higher count rate than the individual segments so a shorter time constant of 15 μs is used.

The other aspect of the preamplifier response that affects the signal shape is the finite bandwidth. The charge loop cannot react instantly to changes at the input stage which has the effect of introducing a rise time of $\approx$20 ns to a square input signal.

Finally there is a further reduction in bandwidth due to the anti-aliasing filter applied at the input to the digitiser stage which acts as a low pass filter with a threshold of 50 MHz.

A response function has been developed [Sch09b] to reproduce the observed signal, $V(t)$, from the simulated input current, $I(t)$, and the preamplifier response function, $R(t)$,

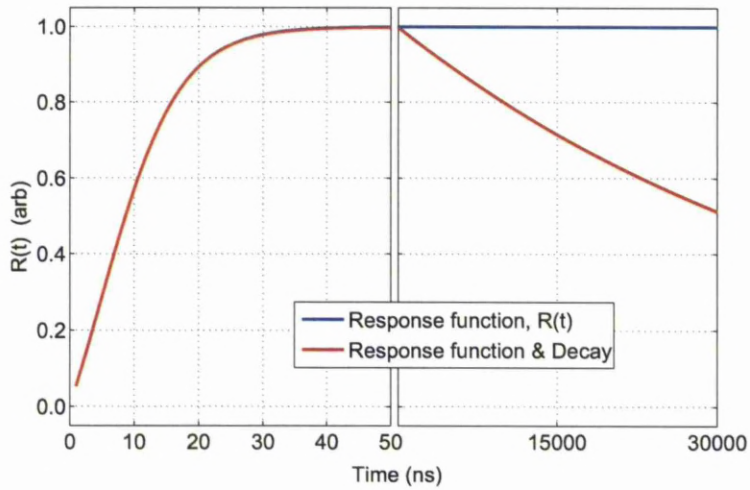

Figure 3.7: The preamplifier response function $R(t)$ with (red) and without (blue) the term due to the decay across the capacitor. Convolving this function with the simulated current signals takes account of the finite preamplifier rise time, anti aliasing filter and preamplifier decay. In order to clearly show both the rising edge and tail of the function, a broken x axis has been used with a change in scale from 50ns onwards.

$$V(t) = \int_0^t I(t-t') \cdot R(t')\mathrm{d}t', \tag{3.7}$$

where $R(t)$ is given by,

$$R(t) = g \cdot \frac{1}{1-c} \cdot \left(\frac{1}{1 + \frac{1-c}{c} \cdot exp\left(-b \cdot t\right)} - c \right) \cdot exp\left(-\frac{t}{t_d}\right), \tag{3.8}$$

The parameters used to fit this function were calculated from pulser measurements performed at IKP Cologne [Dim08]. The input to the preamplifier was a +1.0V step function with 5ns rise time, values were determined for b and c of 0.1675 and 0.3021 respectively.

The response function, $R(t)$ is shown in *Figure 3.7* in red. The blue line indicates the behaviour of $R(t)$ if the preamplifier decay term is not included. *Figure 3.8* shows the effect on the simulated charge signal. The corrected signal (red) shows how the sharpest features of the uncorrected signal are smoothed due to the finite time required for the system to respond to a change at the input stage. On a longer time scale the decay of the charge across the capacitor can be seen.

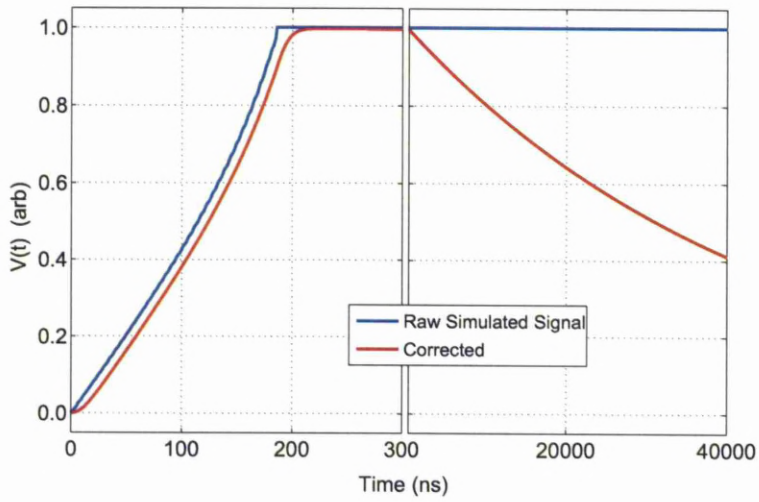

Figure 3.8: Simulated AGATA charge pulse before (blue) and after (red) the preamplifier correction. The effect of the limited bandwidth can be seen to smooth the features of the rising edge, simulating the time required for the electronics to respond to a change at the input stage. The x axis has been broken at 300ns and the scale changed to allow the effect of the capacitor discharge to be seen on a longer time scale.

3.6 Simulation Results

A full comparison of the simulated signal shapes with experimental data will be conducted in *Chapter 7*, but some of the variation of several properties with position in the crystal will be briefly considered here.

3.6.1 Potentials and Fields

Figure 3.9 shows slices at x=0mm of the electric potential and field calculated by MGS for AGATA C001. The calculations were performed on a 1mm cubic grid using the manufacturer's specified impurity concentrations of $0.65\times10^{10}\text{cm}^{-3}$ at the front face and $1.4\times10^{10}\text{cm}^{-3}$ at the back face, and a bias of +4500V applied to the core. The 10mm deep passivation layer at the back of the crystal was included in the calculations which has a significant effect on the shape of the field. The equipotential lines can be seen to curve in towards the core as they approach the back of the detector.

The electric potential is shown on the right, this is calculated on the same 1mm cubic

grid by taking the gradient of the potential. Regions of weaker field can be seen near the corners at the front face and in the passivation layer, and near to the central contact in the back half of the detector.

Figure 3.10 shows the electric potential at x=0mm calculated by JASS for AGATA C001. The calculations were performed on a 0.5mm grid using first the manufacturer's specified impurity concentrations (left) and then a reduced impurity concentration at the back of the detector of $1.2\times10^{10}\text{cm}^{-3}$, in both cases a bias of +4500V was applied to the core. The black regions within the crystal volume are predicted by the simulation to be undepleted, this region represents 2.5% of the detector volume in the case of the manufacturers impurity concentration and 0.16% in the case of the reduced impurity concentration.

The initial simulation was performed with the manufacturers specifications but the size of the depletion region was too large considering the crystal had been experimentally demonstrated to be fully depleted (see *Chapter 4*). The potential was calculated for a range of impurity concentrations at the back face and the undepleted volume measured. The aim was to select a concentration such that the crystal was just depleted, allowing us to work with the simulation in all regions of the detector but with the minimum change from the accepted impurity level. For this reason $1.2\times10^{10}\text{cm}^{-3}$ was chosen as the concentration to work with for pulse shape generation.

The passivation layer at the back of the crystal was not considered by JASS, instead a boundary condition was applied ensuring the equipotential lines were perpendicular to the back surface. This difference between JASS and MGS has a significant effect on the field and hence signal shapes produced in this region of the detector. This will be considered in more detail in *Chapter 7*.

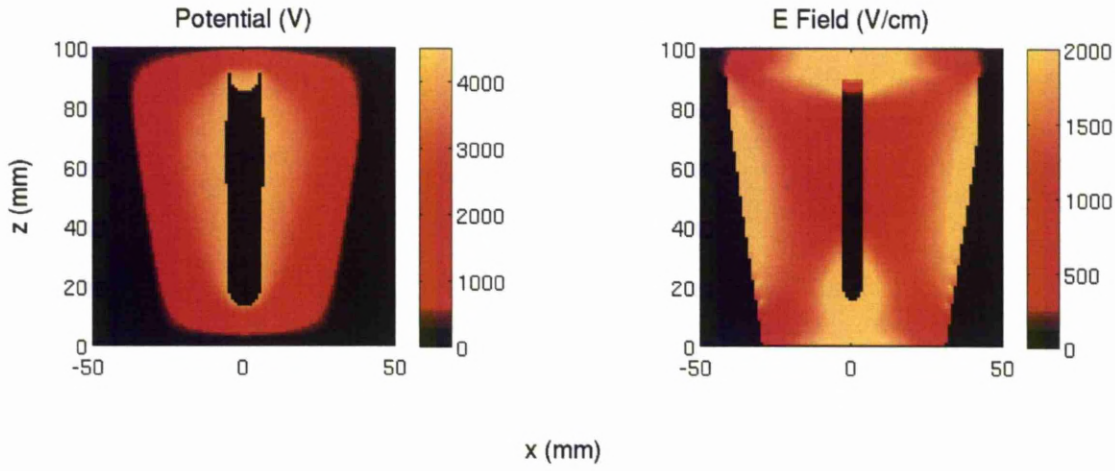

Figure 3.9: The electric potential (left) and field (right) as calculated by MGS. The potential is calculated on a 1mm basis by the solution of Poisson's equation, it depends on the geometry and impurity concentration of the crystal and the bias of +4500V applied to the central contact. The calculation includes the 10mm deep passivation layer at the back on the crystal, in this region the potential distribution differs significantly from that calculated by JASS. The electric field is calculated by taking the gradient of the potential, regions of weaker electric field can be seen near the corners of the front face, close to the core and in the region of complex field near the back of the detector.

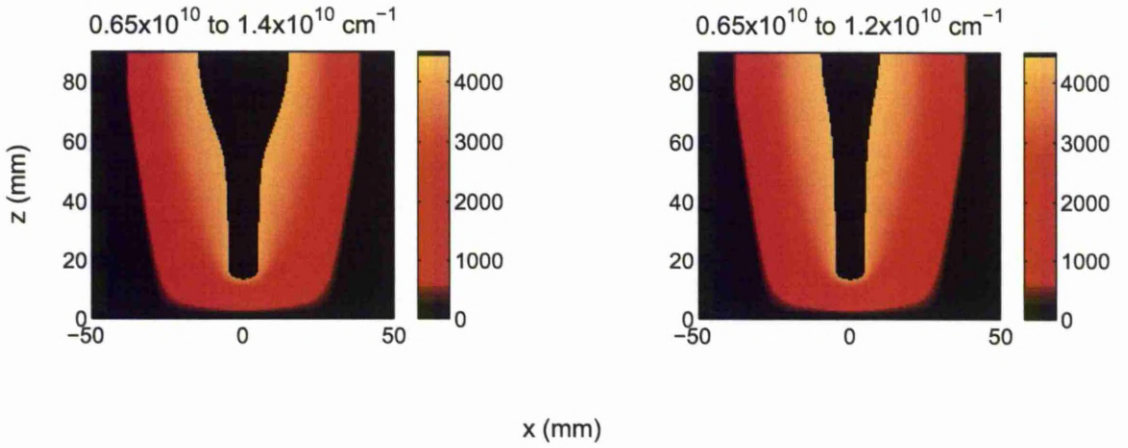

Figure 3.10: The electric potential as calculated by JASS using the manufacturers specified impurity concentration (left) and a reduced impurity concentration at the back of the detector (right). The potential is calculated on a 0.5mm basis by the solution of Poisson's equation, it depends on the geometry and impurity concentration of the crystal and the bias of +4500V applied to the central contact. The calculation does not include a passivation layer at the back, equipotential lines are all perpendicular to the crystal boundary at z=90mm. This produces a different potential distribution than that seen by MGS in this region. The black regions within the crystal volume are predicted by the simulation to be undepleted. The undepleted region represents 2.5% of the detector volume in the case of the manufacturers impurity concentration and 0.16% in the case of the reduced impurity concentration.

3.6.2 Signal Shapes

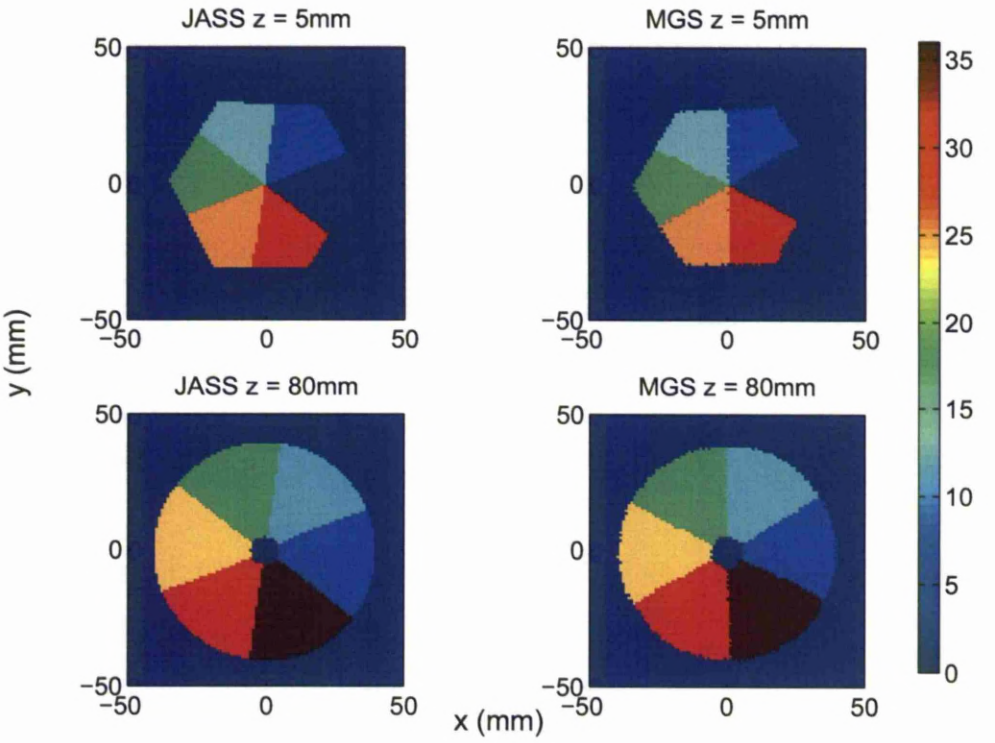

Figure 3.11: The segmentation of JASS (left) and MGS (right). The colour at each point indicates the segment in which charge will be collected from an interaction at that point. Slices of the xy plane are shown at z=5mm (top) and z=80mm (bottom), the positive x direction runs through the centre of sector A, as dictated by the official AGATA coordinate system. The area of the cross-section appears smaller in MGS due to missing points around the outside of the crystal. This is caused by the 1mm grid size in MGS which is insufficient to model the rapidly changing field near the detector contacts.

Figure 3.11 shows the segmentation of the crystal in two xy planes according to JASS and MGS. The colour at each point represents which segment the charge will be collected in for an interaction at that point. The positive x direction runs through the centre of sector A and the positive y direction along the B/C boundary, as dictated by the official AGATA coordinate system. All of the simulated and experimental data presented in this work will be translated into this coordinate frame.

The area of the cross sections appears smaller in MGS due to missing data near the

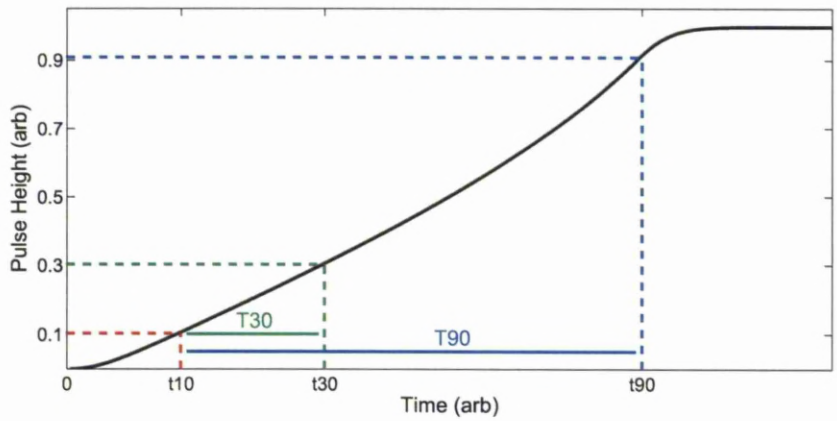

Figure 3.12: In order to avoid the difficulty in precise determination of the start of a signal, the rise time can be measured between fixed points. The time between 10% and 30% (T30) and between 10% and 90% (T90) will be considered here.

outer edge of the crystal, this is the result of the fixed 1mm grid which is insufficiently fine to represent the rapidly changing field near the segment boundaries.

When considering the systematic variation in signal shape across a detector it is useful to consider the time until the signal reaches certain fixed fractions of its maximum height. The electronic noise present in experimental data makes it difficult to determine precisely the point at which the signal started, making it difficult to perform rise time measurements. One solution to this is to consider the time for a signal to go from some small fraction of its height to some larger fraction. *Figure 3.12* shows the particular rise time measurements to be considered here, the *T30* is a measures the rise time of a signal from 10% to 30% of its final height, and *T90* is a measured from 10% to 90%. Although there is no electronic noise on simulated signals and so precise rise times can easily be measured, these parameters will be used to enable a comparison with experimental data.

Figure 3.13 shows the core T30 for slices of the detector at z=5mm (top) and z=80mm (bottom), according to JASS (left) and MGS (right). As the radius of an interaction increases the T30 becomes larger, this is due to the weighting potential of the core which is changing most quickly close to the contact. The variation in T30 with changing azimuthal angle is dominated by the four fold symmetry of the crystal lattice, charge collection is fastest in the <100> direction. The values calculated by JASS are larger than MGS at the

front of the crystal, but the difference is very small. At the back of the crystal there is much greater variation between the two simulations, the JASS values are smaller than MGS near the outer contact and larger near the core.

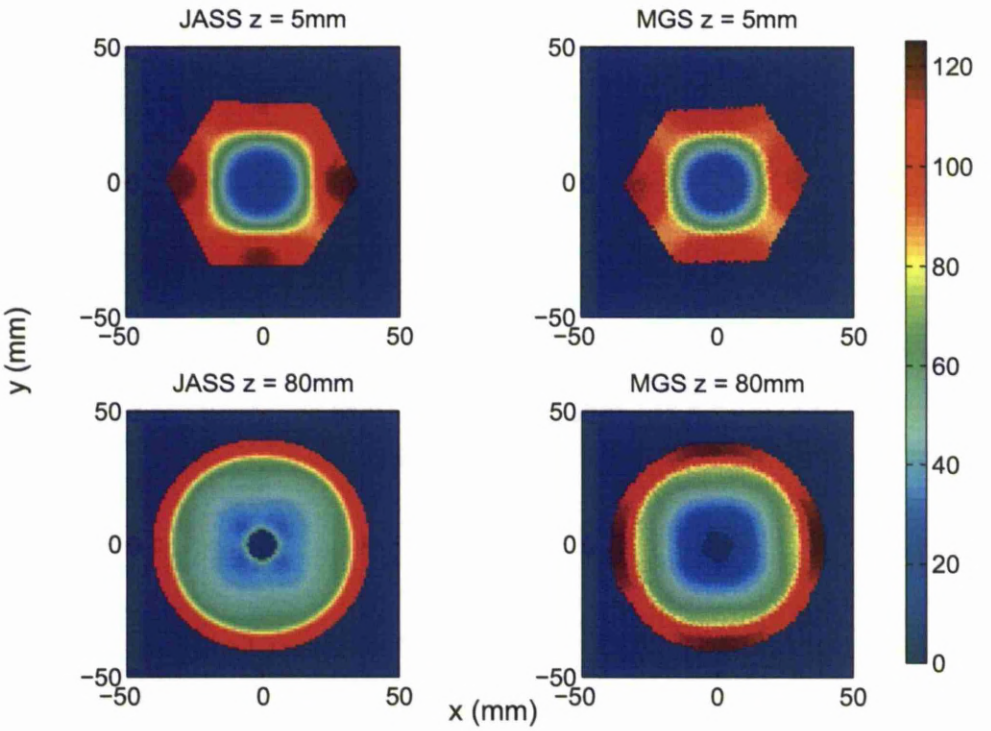

Figure 3.13: Core T30 (ns) for slices of the detector at z=5mm (top) and z=80mm (bottom), according to JASS (left) and MGS (right). The fastest times are found near the centre of the detector, closest to the core contact. The four fold symmetry of the germanium crystal can be seen in the azimuthal variation, with the fastest rise times being found along the <100> axis. The MGS signals are slightly faster than JASS at the front of the detector. At the back of the detector the MGS signals are slower at large radius and faster at small radius.

Figure 3.14 shows the core T90 for both simulations at the same z positions. At the front of the detector, the JASS distribution is dominated by discontinuities in the rise time distribution centred on the <110> axis directions. The sudden change of around 50ns rise time with 1mm change in position seems unphysical, the signals from these positions will be considered in more detail in *Chapter 7*. Further back in the detector, the JASS basis shows the typical behaviour of T90 in a coaxial detector, the minimum rise time is at intermediate

radius when both holes and electrons have equal drift time. To either side of this position the rise time increase as one charge carrier, holes at small radii and electrons at large radii, dominate the signal.

At the front of the detector, MGS produces the longest rise time along the x axis when the <110> axis is aligned with the segment corner. Further back in the detector the MGS rise time is significantly less than that seen in JASS, also the systematic behaviour is different, with the minimum value being much closer to the core. These differences in behaviour at the back of the crystal are likely the result of the differences in electric field in this region, discussed in the previous section.

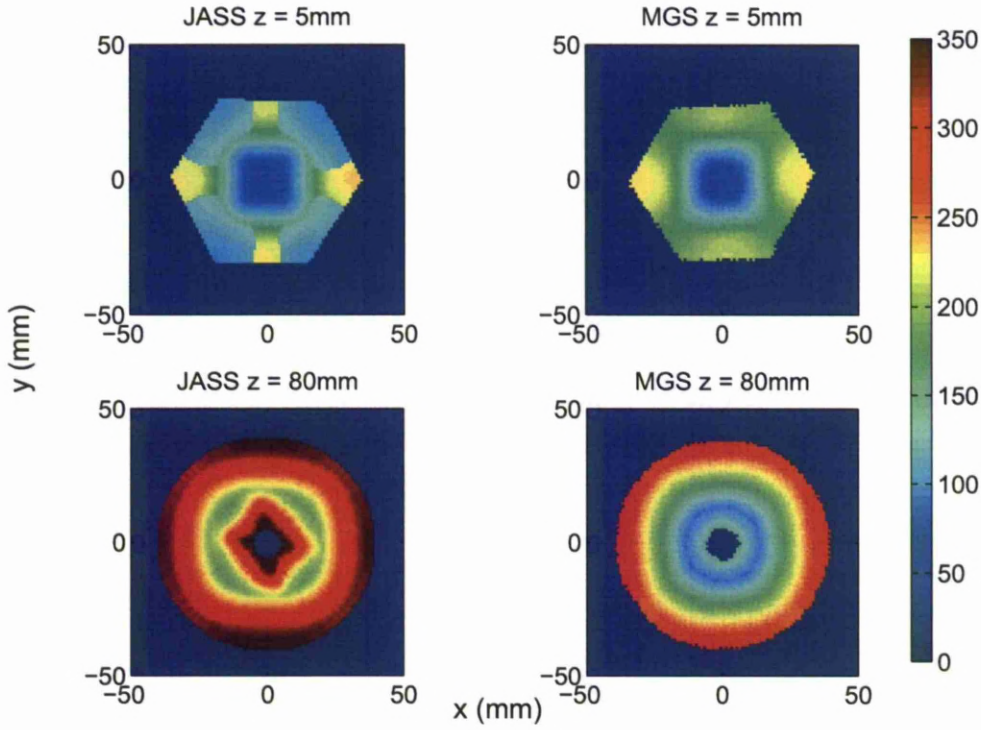

Figure 3.14: Core T90 (ns) for slices of the detector at z=5mm (top) and z=80mm (bottom), according to JASS (left) and MGS (right). At the front of the detector, the JASS T90 has some striking discontinuities centred on the <110> axis directions that dominate the distribution. Towards the back of the detector, the JASS basis shows the typical behaviour of T90 in a coaxial detector, the minimum rise time is at intermediate radius when both holes and electrons have equal drift time. At the front of the detector, MGS produces the longest rise time along the x axis when the <110> axis is aligned with the segment corner. Further back in the detector the MGS rise time is significantly less than that seen in JASS, also the systematic behaviour is different, with the minimum value being much closer to the core.

Chapter 4

Singles Measurements

Characterisation measurements were performed on the AGATA crystal C001 while it was mounted in a test cryostat. The first measurements, described in this chapter, were performed using a single trigger condition, specifically that the energy recorded on the detector central contact was greater than a fixed threshold level. First the detector efficiency and the energy resolution of each segment were studied using an analogue data acquisition system which recorded only the energy deposited by each gamma interaction. The results from these measurements were compared with the performance specified by the crystal manufacturer. Following this the detector was connected to a digital acquisition system which stored the digitised signal traces for each channel (36 segments + core). The Liverpool scanning system was then used to interrogate the detector with a highly collimated source. Data were analysed to investigate the crystal geometry and orientation, the rise time distribution, and the depletion behaviour.

4.1 Analogue Measurements

Each encapsulated detector crystal, supplied by the crystal manufacturer Canberra, must meet minimum standards for efficiency, energy resolution and crosstalk if it is to be accepted by the AGATA collaboration. Additionally, whenever the crystal is transferred to a new cryostat or transported between labs, the performance must again be checked.

Upon the arrival of the test cryostat containing C001 in Liverpool, the Dewar was filled with LN_2 and the crystal temperature monitored using the PT100 platinum thermistor

attached to the side of the capsule. The temperature reached the operating level of 88K after 3 hours but the system was left overnight to equilibrate before any measurements were made.

For initial testing the detector was connected to an analogue acquisition system consisting of an ORTEC 671 spectroscopy amplifier with 6 μs shaping time and an ORTEC 927 multi-channel analyser. Energy resolutions were measured separately for all 37 detector channels at gamma-ray energies of 60 keV and 1332.5 keV using ^{241}Am and ^{60}Co sources. The ADC provided conversion over 16k channels and the amplifier gain was chosen so as to spread the energy region of interest across the full range of channels. The energy resolution of the central contact was measured to be 1.29 keV and 2.27 keV at 60 keV and 1332.5 keV respectively, the energy resolutions of the segments are shown in *Figure 4.1*. The energy resolution of all channels fell within the manufacturer specifications of 1.3 keV and 2.3 keV.

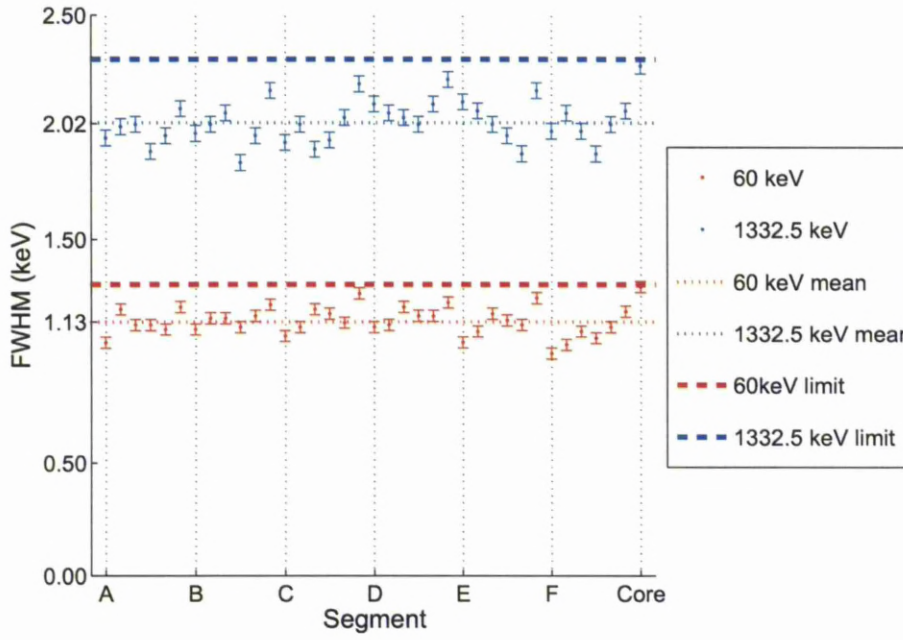

Figure 4.1: Energy Resolutions measured for all C001 segments at 60 keV and 1332.5 keV using analogue electronics. The mean indicated on the plot has been calculated from the segment resolutions only, as the core has a higher value due to its larger capacitance. The segments are numbered according to the official AGATA numbering scheme (see *Figure 1.5*).

The energy resolution measurements performed earlier by Canberra are shown in *figure*

4.2 for comparison [AQP05]. These were performed using the same encapsulated crystal but mounted in a different cryostat and coupled to different electronic components. Due to the large time required to collect sufficient counts for an accurate measurement, only selected segments were measured at 1332 keV.

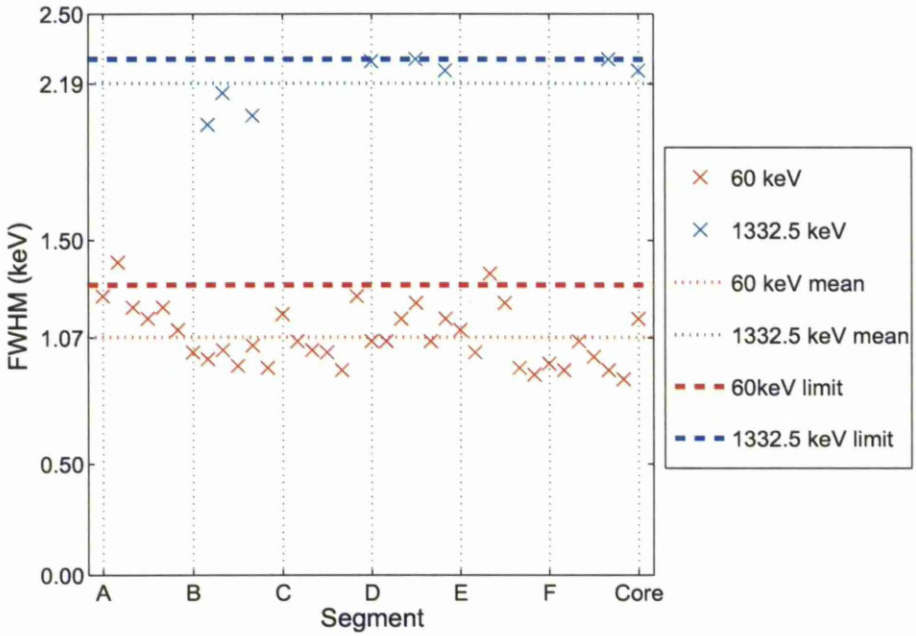

Figure 4.2: Energy Resolutions measured for all C001 segments at 60 keV and 1332.5 keV, performed by Canberra before the capsule was shipped to the AGATA collaboration [AQP05]. The mean, calculated from the segments only, and the guaranteed specification values, are also shown.

The absolute photopeak efficiency measurements were performed using a ^{152}Eu and ^{241}Am sources placed 25cm from the centre of the crystal's front face. Spectra were built for each source using the signal from the central contact and the same analogue acquisition system used for the energy resolution measurements. *Figure 4.3* shows the variation of absolute efficiency with gamma-ray energy, statistical errors are indicated on the plot but systematic uncertainties have been ignored. The systematic error is dominated by the uncertainty on the source position, the expected uncertainty of $\pm$0.5cm leads to $\approx$8% additional uncertainty on the stated efficiencies.

Finally the relative efficiency [Kno10] was measured using a ^{60}Co source, also placed 25cm from the crystal front face and found to be 83$\pm$2%. The relative efficiency quoted by

the manufacturer was 78.9%, a check for consistency cannot be performed as no uncertainty was quoted on the manufacturer measurement.

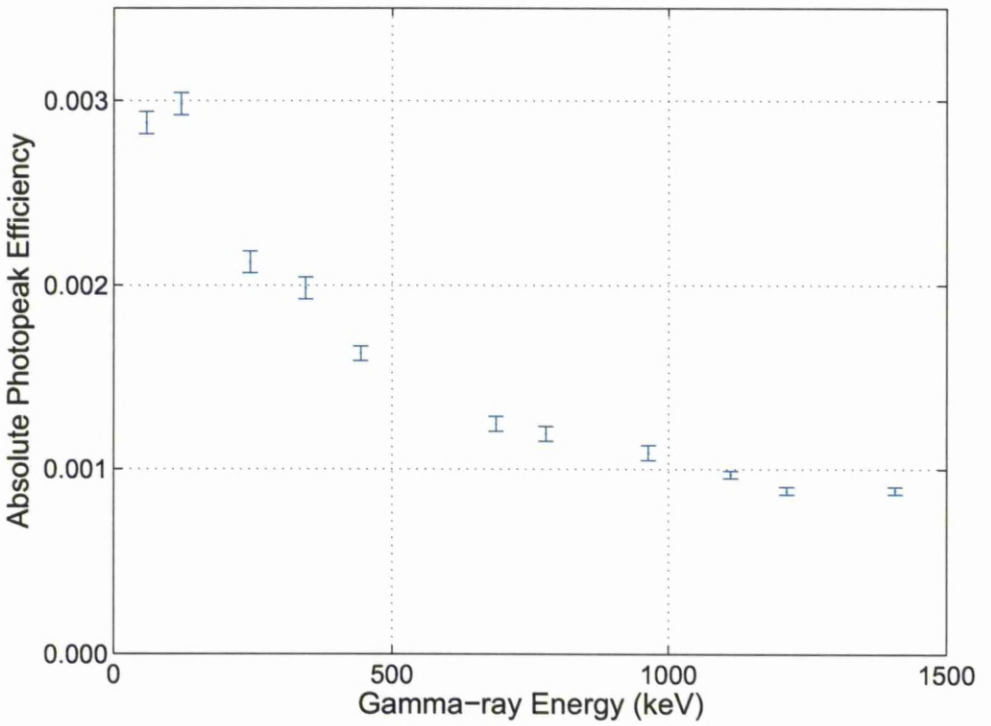

Figure 4.3: The absolute photopeak efficiency for ^{241}Am and ^{152}Eu sources placed 25cm from the crystal front face. The uncertainties shown on the plot represent the statistical variance only. There is some degree of systematic error across the range of values due to uncertainty in the source position, this has been estimated as ±8% of the stated values.

4.2 GRETINA Digitisers

Digital data acquisition was performed using four, 10-channel GRETINA digitisers [DJYZ06] mounted in a 64bit VME-X crate. Each card combines 10 100MHz flash ADCs (10ns sample size) with 14bit precision, and a powerful FPGA to perform analysis on the digitised signal. In order to avoid aliasing effects, the input stage of each channel incorporates a Nyquist high-frequency filter.

The digitisers sample the signal continuously and write the results into an on-board

FIFO memory buffer. On receiving a trigger signal the cards pause the sampling process while the contents of the FIFO and are written to disk, for this experiment we chose to write 128 samples of each signal for each event. A *pre-trigger* value can be set in the digitiser's registry, this tells the card how far back to look in its FIFO to account for the finite processing time of the triggering system. The value was tuned during set up to ensure the rising edge of the charge pulse was centred in the 128 sample range. The on-board FPGAs implement a series of digital signal processing (DSP) algorithms on each signal:

- Leading Edge Discrimination
- Constant Fraction Discrimination
- Pole-zero Correction
- Trapezoidal Filter [Jor94]

The two discriminators each provide time-stamps, the pole-zero correction accounts for the pre-amplifier decay, and the trapezoidal filter, also known as a *Moving Window Deconvolution* (MWD), provides an accurate measure of the integrated charge which is proportional to the energy deposited in the detector. The time-stamps and energy values for all signals were written to disk along with the signal traces.

The firmware on the cards does allow for automated trigger logic using the discriminator functions but for this work we used an external trigger which was propagated to the cards by a Silena ADC controller. In order to maintain correct time alignment of the signals, a common clock signal is shared between all cards.

Along with the energy value provided by the trapezoidal filter, we also calculated the deposited energy from the signal trace. In the first stages of our analysis the mean of the first 30 and of the last 30 samples in the trace were calculated, the difference between these was recorded as the *Baseline Difference* energy. Both methods of calculating the deposited energy were subject to the variation in gain of one channel relative to the next, this effect was accounted for by performing careful gain-matching before and after the experimental run. Spectra were collected for each channel using ^{152}Eu and ^{241}Am sources which provide a range of gamma-ray energies between 59.5keV and 1408keV and the value returned by the cards and baseline difference were recorded for each peak. A least-squares fitting algorithm

was then used to establish the relationship between the true deposited energy and values we measured using each method. All results in this thesis have been corrected for this variation in gain.

4.2.1 Missing Data

During offline analysis, after all data collection had been completed, it was noticed that for a proportion of events the data from one or more digitiser cards were missing. The problem was caused by a bug in either the GRETINA card's firmware or the data acquisition system interfacing with the cards.

This problem was found to affect 5 - 10% of events, depending on the particular experimental run being considered. A simple gate was applied as the first stage in all analysis codes to check there were 37 digitised traces and 37 MWD energy values, before processing each event. This meant that the events that were analysed included data from all detector channels, but it reduced the number of events in the data set.

4.3 Scanning Electronics

The electronics used for the singles measurements are shown in *Figure 4.4*. The AGATA preamplifiers, shown within the dashed blue box, were located inside the cryostat. The 37 preamplifier channels each had gain of $\approx$100mV/MeV and provided differential output signals for low noise transmission to the digitisers.

Preamplifier signals were passed through LVDS cables to the CWC converter boxes, which were manufactured at TU Munich and IKP Cologne and installed within a standard NIM crate. The converter boxes recombined the differential signals, providing one single-ended output for each segment and three identical outputs for the core. All segment signals and one of the core signals went straight to the GRETINA digitiser cards, and were not involved in triggering the system.

One of the remaining core signals was used for an analogue measure of the deposited energy, an ORTEC 671 spectroscopy amplifier with 6μs shaping time was used to shape the signal, and a CAEN V785 ADC to measure the height. This provided an additional check on the measured energy which was included in the data written to disk every time the system was triggered.

The remaining core signal was used as a trigger to determine when the *Data Acquisition System* (DAQ) should pause to write the values from the GRETINA and CAEN ADCs to disk. A combination of an ORTEC 474 Timing Filter Amplifier (TFA) and an ORTEC 584 Constant Fraction Discriminator (CFD) was used to determine if the appropriate energy threshold had been met. The logic pulse produced by the CFD was passed to a Phillips Scientific 795 Gate & Delay generator which provided the 50μs wide, 1V high pulse required to trigger the Silena ADC Controller (SAC).

The SAC fulfilled the dual function of propagating the trigger signal to all of the data collecting components, and inhibiting further triggers while the system was in the process of writing data. If a trigger request signal was received while a disk write operation had not been completed it was ignored.

For the singles measurements the trigger threshold was set to 400keV, at this threshold the number of requested triggers was $\approx$1100cps if the collimated source was pointed into the thickest part of the HPGe crystal. The finite time required to write data to disk limited the accepted rate to 420cps, this resulted in a high deadtime for all the digital measurements with a single trigger condition.

4.4 The Liverpool Scanning System

The Liverpool scanning system, *Figure 4.5*, was used to provide a collimated beam of 662keV gamma rays which could be positioned accurately in the x-y plane, perpendicular to the detector front face. The Parker scanning table consists of two independent stepper motors capable of positioning the table, to 100μm precision, within a range of 30cm in each dimension. The stepper motors work by counting the number of steps from a home position which it can find using a magnetic switch that activates only at this position. The scanning table could be programmed from the DAQ to move through a series of steps and hold each position for a specified time. The x and y positions, together with the step number, were recorded in the data stream for every event.

On top of the scanning table was an assembly of lead blocks with a 920MBq ^{137}Cs source at its centre. A 160mm deep by 10mm diameter tungsten collimator with a 1mm collimation profile, produced a beam of gamma rays normal to the x-y plane in which the table moved. The collimation resulted in a divergence in the gamma-ray beam of 0.179°,

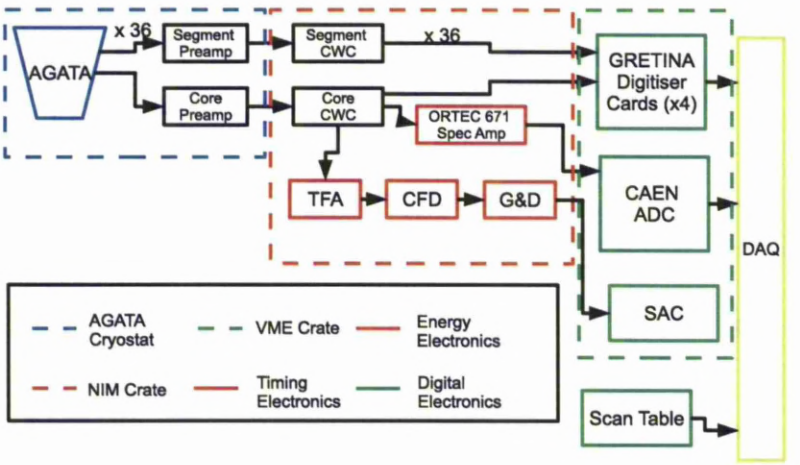

Figure 4.4: The electronics components used in the C001 singles scan. The 36 differential signals from the segment preamplifiers were converted to single ended signals and passed directly to the GRETINA digitisers. Three copies of the core signal were produced at the converter box, one was passed to the GRETINA digitisers, one was used for an analogue energy measurement, and one was used for testing the trigger condition which was that at least 400keV was deposited in the detector.

resulting in a beam spot size of 1.1mm diameter at the front face of the crystal and 1.6mm at the back (see *Figure 5.2 (top)*).

A steel frame was constructed around the scanning table so as to allow the detector to be supported without interfering with the movement of the table. The steel frame supported the AGATA test cryostat and a large storage Dewar which allowed enough LN_2 to be held to keep the detector cool for 7 days without filling. A steel plate was suspended from the frame by threaded rods, this supported the scatter collimators and scintillation detectors required for the coincidence measurements, discussed in *Chapter 2*.

4.5 Front Face Singles Scan

The front face singles scan consisted of 7569 scan positions on a 1mm square grid covering the entire front profile of the detector. The collimator was held for 60s at each position resulting in approximately 20,000 accepted triggers. For every event triggering the system a 128

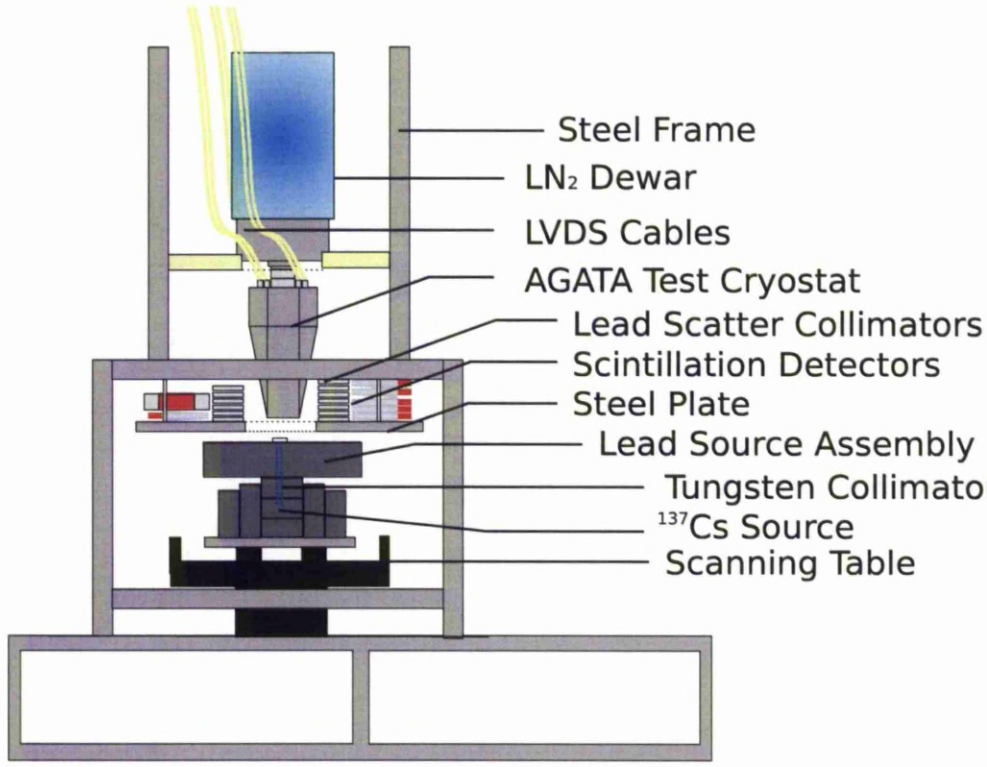

Figure 4.5: The Liverpool Scanning System [DBC+09]. The Parker scanning table was able to move the lead assembly, containing a collimated 920MBq ^{137}Cs source in the x-y plane. The steel support frame held the AGATA test cryostat in position and supported a steel plate, on which the scatter collimators and scintillator detectors were placed.

sample trace for each detector channel was written to disk along with the associated MWD energy values and timestamps, the analogue core energy and the scan table information.

The apparatus was controlled using the MIDAS data acquisition software, data were analysed and spectra produced online using the MTSort [CS] analysis system and functions written in C. Further offline analysis was performed using MTSort, C and MATLAB analysis codes.

The orientation of the cryostat relative to the scan table was determined during set-up by the position of the cryostat handles, these were orientated so as to allow the cryostat to be supported by the steel frame. This orientation was such that a line from the centre of the crystal to the boundary between contacts for sectors C and D was aligned with the

positive x direction of the scan table. The official AGATA coordinate system specifies that the positive x direction should be aligned with the centre of sector A. *Figure 4.6* shows the position of the C001 crystal in the scan table frame (blue) and the AGATA frame (red), a translation and a 150° anti-clockwise rotation is required to transform between the two. This transformation has been applied to all of the front face scan matrices presented in this chapter, where the rotation has required the interpolation of the raw data a bilinear interpolation has been used.

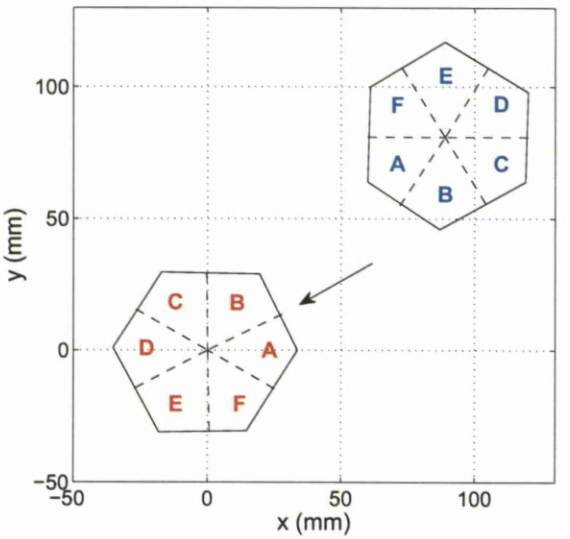

Figure 4.6: The position of C001 in the scan table frame (blue) and the official AGATA frame (red). A transformation between these frames has been applied to all of the front face singles scan and coincidence scan data. During the front face scan the collimator was directed into the page; the black arrow indicates the direction of the collimator, in the AGATA frame, during the singles side scan.

The most significant limitations of the singles scan results are the Compton scattering of gamma rays and the lack of constraint on the depth of interaction. The collimator position can determine the x-y position of the first interaction but not of any subsequent interactions. By applying gates on the deposited energy and number of segments hit we can increase the number of single site interactions and reduce the mean separation of multiple interactions, but we cannot remove all multiple site interactions from the data. Similarly without any

constraint on the depth of interaction, the data will always reflect a mean of the different possible interaction depths within the ring being considered.

4.5.1 Intensity Matrices

Although several pieces of useful information can be extracted from the singles scan data, the primary purpose of performing the measurement was to allow the coordinate system of the scan table to be orientated relative to the crystal. Plotting the intensity of counts as a function of collimator position, while applying carefully chosen gates to the data, allows us to locate the positions of the crystal edges, central contact, and segmentation boundaries.

To generate the plots found in this section, gates have been applied to the *energy* and *fold*. Energy gates have been applied to the central contact MWD energy, in the case of photopeak gates they have been set such that E_γ =662±2keV. There are two related concepts which are referred to as fold, the *true fold* and the *segment fold*. The true fold refers to how many gamma-ray interactions have occurred in the crystal, this cannot be measured by a simple technique and so cannot be gated on in this data. The segment fold refers to the number of segments the deposited energy is shared over, it can been calculated by examining the baseline offset of the individual segment charge pulses. Here a segment is classified as containing deposited energy if the baseline shift seen in the segment is greater than three times the RMS baseline noise ($\approx$ 10keV). The term fold, when used here, refers to the number of segments that pass this threshold for a given event. Due to the difficulty in deconvolving very small energy depositions from the electronic noise, the fold calculation will be incorrect if one of the segments contains $<\approx$30keV.

Figure 4.7 shows, on the left, the total number of accepted triggers for each position in the scan. The hexagonal profile of the front parts of the detector can be seen superimposed on the larger, circular outline of the back as a region of increased count rate due to the greater depth of germanium. The circular area of lower intensity in the centre is due to the small depth of germanium here due to the hole drilled for the central contact. In the thickest parts of the detector $\approx$17000 counts are recorded at each position, this drops to $\approx$12000 counts in front of the core contact. As there is no gate applied to the energy deposited in the detector, this measurement is very sensitive to background and scattered gamma rays. The square profile of the actual range of scanned positions is visible due to the significant

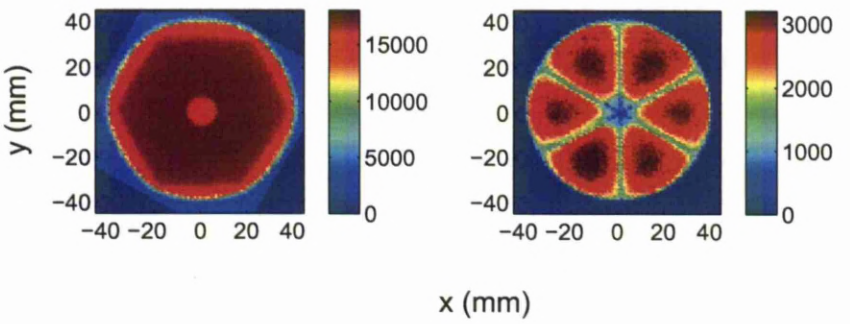

Figure 4.7: Number of accepted trigger requests as a function of position (left). Number of photopeak events with the energy confined to a single segment as a function of position (right). In the image on the left there are no software gates applied data so the intensity in the matrix represents the number of events passing the trigger condition of >400keV deposited in the crystal. The image on the right shows only photopeak events (E = 662±2keV) with all of the energy in a single segment. This condition is more less likely to be satisfied when the collimator is positioned near a segment boundary due to scattering between segments, this causes the segmentation boundaries to become visible.

background rate when the collimator is pointed outside of the detector, this illustrates the rotational transformation that has been applied to the data.

Figure 4.7 shows, on the right, the total number of fold 1 photopeak events at each position in the scan. Applying a photopeak gate reduces the overall number of events counted but this affects the background counts more than the true counts, resulting in more sharply defined boundaries in the image and a suppression of count rate when the collimator is outside of the crystal. Near the boundary of segments the fold gate has a significant effect, at these positions, the probability for a gamma ray to scatter and deposit part of its energy into a neighbour segment is high. Near the centre of the segments the effect of the fold gate is much less, any scattered gamma ray has a significant chance of being absorbed in the same segment before passing into another. This results in a drop in counts from ≈3500 at the centre of a segment to ≈1500 near the boundaries which allows us to establish the position and orientation of the segments.

Figure 4.8 shows a similar photopeak, fold 1 intensity plot but with the events split between six matrices, one for each of the six rings. This allows three further important observations to be made:

- The attenuation of gamma rays through the depth of the detector is apparent in the bulk volume of the segments. The count rate at the centre of ring 1 segments is ≈1300, this drops to ≈200 at the same position in ring 6. The highest rates however, are at the back of the detector when the taper of the crystal directly exposes rings five and six to the collimated beam. The high count rate here is due to the back rings having the largest depth of germanium and also to the reduction in dead time as the system does not have to deal with triggers from the front rings.

- The centre of segmentation in ring one is not aligned with the centre of the central contact. The segment boundaries in the front ring are determined by the boundaries of the electrical contacts applied to the outside of the crystal, these are not aligned with the centre of the hole drilled to produce the central contact. For the coincidence measurements, discussed in *Chapter 5*, it was necessary to pick a central point, about which to define our scan positions, the ring 1 segmentation centre, rather than the central contact centre, was chosen for this purpose.

- In rings two to five, the segment boundaries on opposite sides of the detector are, in general, not aligned with each other. Due to the anisotropy of charge carrier drift velocity with respect to the crystal lattice, charge carriers tend to move preferentially along the axis with higher mobility. This means charge collection is not in general on a line direct from the point of interaction to the central contact unless this direction is aligned with one crystal axis. The B/C, E/F boundary, parallel to the y axis on the plot is straight as the electric field along this boundary is aligned with the <100> crystal axis.

4.5.2 Rise Time Matrices

In order to investigate the systematic variation of the signal shape as a function of interaction position, matrices of T30 and T90 (see *Section 3.6.2*) have been produced. The same photopeak and fold 1 gates applied to generate the intensity matrices above have been applied to each individual event. For each each scan position the mean T30 and T90 of all events passing the gates has been calculated at each position and the results entered in a matrix for each detector ring. To suppress the number of background events when

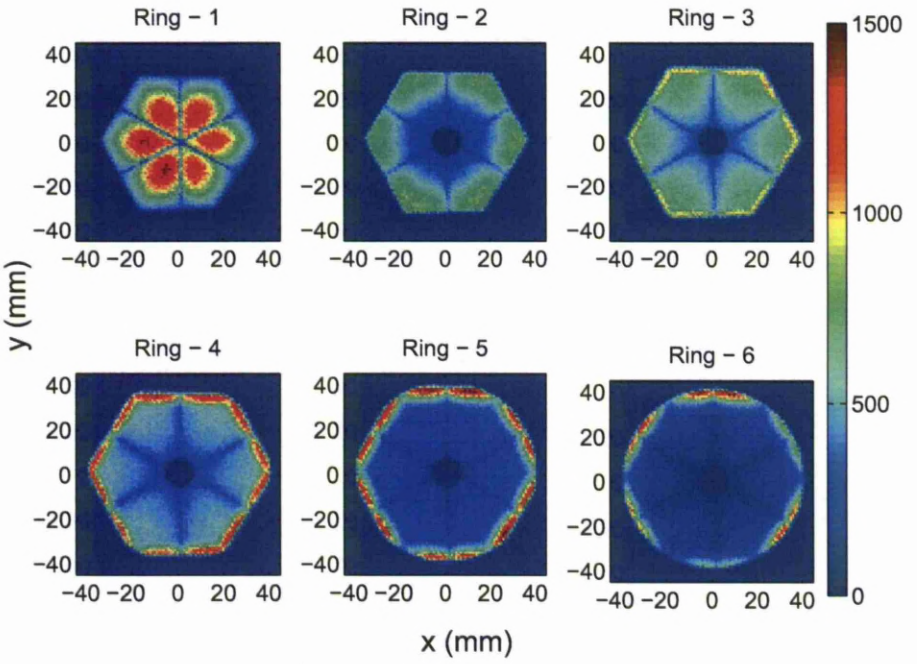

Figure 4.8: The intensity of photopeak fold 1 interactions for each ring in the detector. The segmentation boundaries can be seen due to increased probability that the energy will be shared between segments if the collimator is positioned near the boundary. This information is used to orientate the detector relative to the scan table axes.

the collimator is outside of the crystal a threshold has been applied to the number of events contributing to the mean. Combinations of position and ring for which fewer than a threshold number of events passed the energy and fold gates have been set to zero in the matrix. The threshold was set independently for each ring due to the varying count rate through the depth of the detector. Towards the back of the detector it became more difficult to set a threshold that would suppress the background outside the crystal without also suppressing some positions within the crystal, this resulted in points being recorded outside the crystal at some positions in rings 3 to 6. Due to occasional drops in the data acquisition rate there are scattered points within the crystal volume which also failed this test.

Figure 4.9 shows the T30 for the central contact signal.

- The general trend in the radial direction is for T30 to increase with distance from

the core, this is the result of the weighting field gradient being steepest close to the contact. The electrons produced from an interaction near the outer contacts have a long way to move before they induce a significant signal on the central contact. Along a radial line, the T30 typically varies between 40ns and 100ns.

- With changing angle the trend is dominated by the four-fold symmetry of the crystal lattice, the T30 is faster along the <100> direction than the <110>, this pattern repeats for every 90° rotation. This variation with direction will be exploited to measure the crystal axis orientation in *Section 4.5.3*.

- The longest T30 times in the crystal (≈140ns) are found near the regions of weaker electric field in the corners of ring 1. In theses regions, the charge carrier drift velocity is not immediately saturated which lengthens the overall rise time.

Figure 4.10 shows the T90 for the central contact signal.

- The T90 typically varies between 150ns and 350ns in the coaxial region of the detector. Shorter times of ≈ 80ns are seen in the region immediately in front of the core, this is a unique region of the crystal where the charge collection is in the <111> direction and over a very short distance which leads to a small T90.

- The T90 measurement is approaching the total charge collection time and so the signal induced by both holes and electrons must be considered in order to understand the radial trend. If we were able to measure the complete charge collection time from 0% to 100%, we would find a minimum, in the radial direction, at the point when hole and electron drift times were equal. As the drift velocity of electrons is greater than that of holes, this minimum would be closer to the outer contact than the positive central contact. As we are measuring the charge collection to 90% only, there is a shift in the position of the minimum toward the contact on which the rise time is measured, in this case the core. Either side of this minimum there is a trend of increasing T90 toward both contacts.

- The longest rise times are seen near regions of weaker field, at the corners of ring 1, and at the extremes of radius in rings 5 and 6, where the total drift distance is

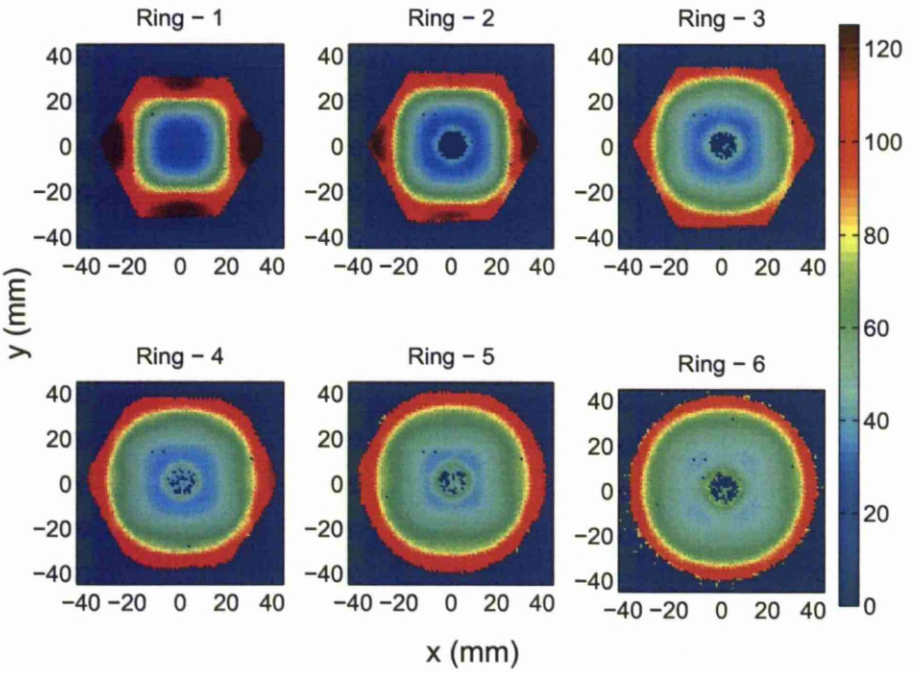

Figure 4.9: The time (ns) for the core charge pulse to rise from 10% to 30% of its maximum height for fold 1 photopeak events in rings one to six. The general radial trend is of increasing T30 with increasing distance from the central contact due to the weaker core weighting field at large radii. In addition the four fold symmetry of the crystal lattice can be seen to influence the variation in rise time profile with charge collection direction, the shortest rise times are along the <100> axis and longest along the <110>.

greatest. In ring 1 there is a circular region of very small T90 directly in front of the central contact.

Figure 4.11 shows the T30 distribution measured for the outer contact signal. The radial trend seen here is the inverse of that seen in the core T30, the longest times are seen near the central contact where the outer contact weighting field is weakest while the shortest times are next to the outer contact. The radial trends for the segment T90, shown in *Figure 4.12*, are again similar to the core. The shortest values are seen at intermediate radii where the hole and electron drift times are equal and the value increases as the radius of interaction moves toward either contact.

The angular trend however is unlike that seen in the core in two ways, firstly the trend

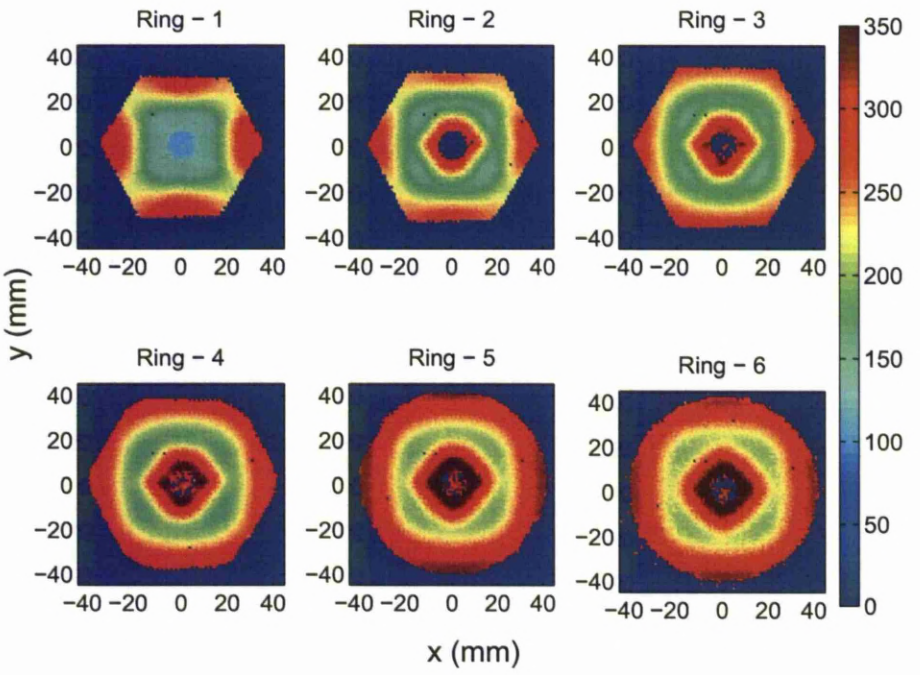

Figure 4.10: The time (ns) for the core charge pulse to rise from 10% to 90% of its maximum height for fold 1 photopeak events in rings one to six. The minimum T90 values are found at intermediate radii, where the electron and hole drift times are similar, at positions either side of this the time is dominated by the collection of the carrier with the longest drift time. The longest T90 values are found near regions of weak field in ring 1, and at the extremes of radii in rings 5 and 6, where the total drift distance is longest.

is dominated by the six fold symmetry of the crystal shape rather than the four fold lattice symmetry, and secondly the trend is different for the T30 and T90 distributions. The longest segment T30 rise times are seen in directions where the holes will be collected at the centre of one of the crystal faces. It is proposed that this is due to a weakened electric field at these points due to the gap between the outer contacts. The segment T90 distribution has the opposite angular trend, with the shortest rise times being in the direction of the centre of a face. This is due to the shorter overall charge collection distance in these directions which, when looking at the total collection time, dominates the weaker trend due to the spacing between contacts.

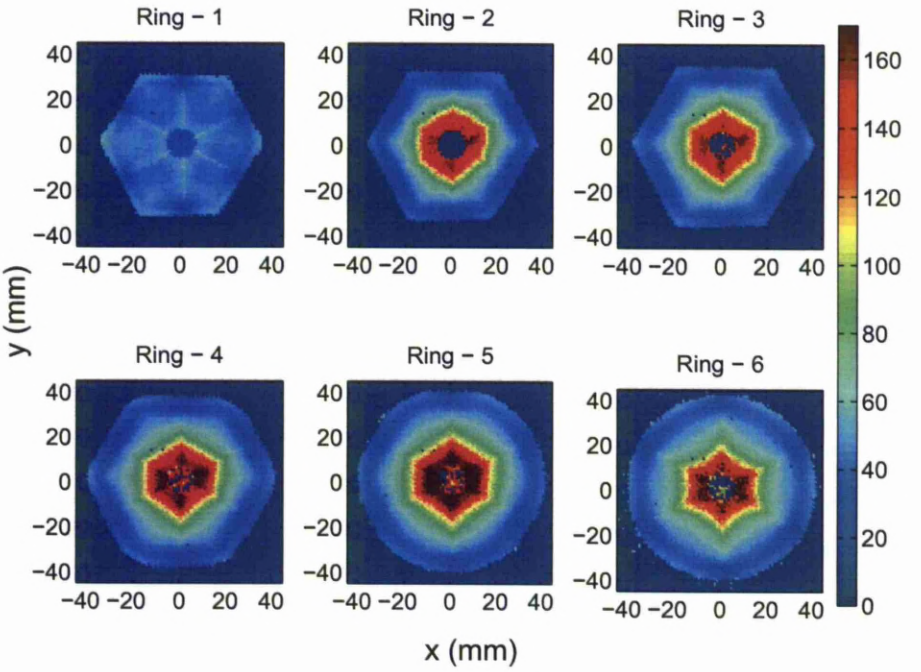

Figure 4.11: Segment T30 (ns) for fold 1, photopeak events in rings 1-6. The radial trend is of increasing T30 as the distance of the interaction from the outer contact increases, this is due to the weaker segment weighting field at these positions. The angular trend is dominated by the six fold symmetry of the crystal, with longer rise times found when charge is collected toward the centre of a face due to the spacing between contacts producing a weaker electric field at these points.

4.5.3 Crystal Axes

The core signal is used to establish the crystal axis orientation as its variation with angle is dominated by the crystal structure rather than the six fold detector symmetry. Similarly the T30 has been used rather than T90 as it is less dependent on the total charge collection distance,which varies with the crystal shape, than the T90. *Figure 4.13* (left), shows the core T30 as a function of angle, measured at 28mm radius, for each of the six rings. The values have been extracted from the core T30 matrix for 360 positions separated by 1° increments. A mean has then been formed from each pair of consecutive values to reduce the statistical fluctuation and the resulting 180 values plotted.

The distribution has four minima, corresponding to charge collection along the <100> axis and four maxima, corresponding to collection along the <110>. The mean position

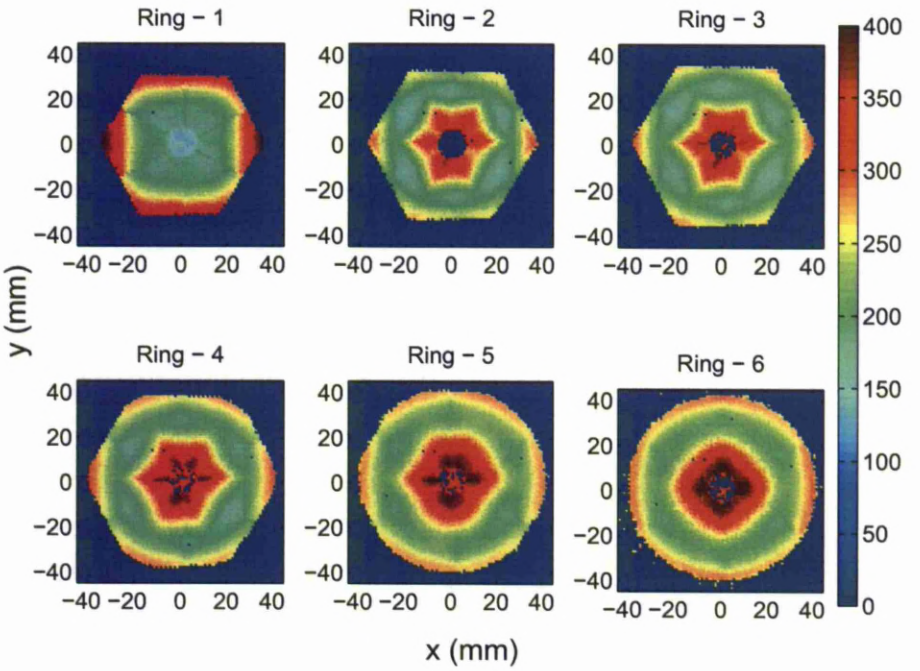

Figure 4.12: Segment T90 (ns) for fold 1, photopeak events in rings 1-6. The radial trend here produces the shortest rise times when the charge collection times for electrons and holes is equal at intermediate radii, T90 increases from here toward either contact. The angular trend follows the six fold crystal symmetry with the shortest rise times found toward the centre of each face, where the charge collection distance is greatest.

of each minima, across each of the six rings, has been calculated and plotted as a black dashed vertical line. The plot on the right shows the T30 distribution for ring 3, as shown previously in *Figure 4.9*, the points used for the left hand plot are highlighted in red and the first <100> and <110> axes have been indicated by black arrows.

The detector specification agreed between the AGATA collaboration and the crystal manufacturer, Canberra, states that the <100> axis should align with the centre of sector A, which lies on the x axis in the AGATA coordinate frame used here. It is clear from this data that for C001 the axes are in the opposite configuration to that which was agreed.

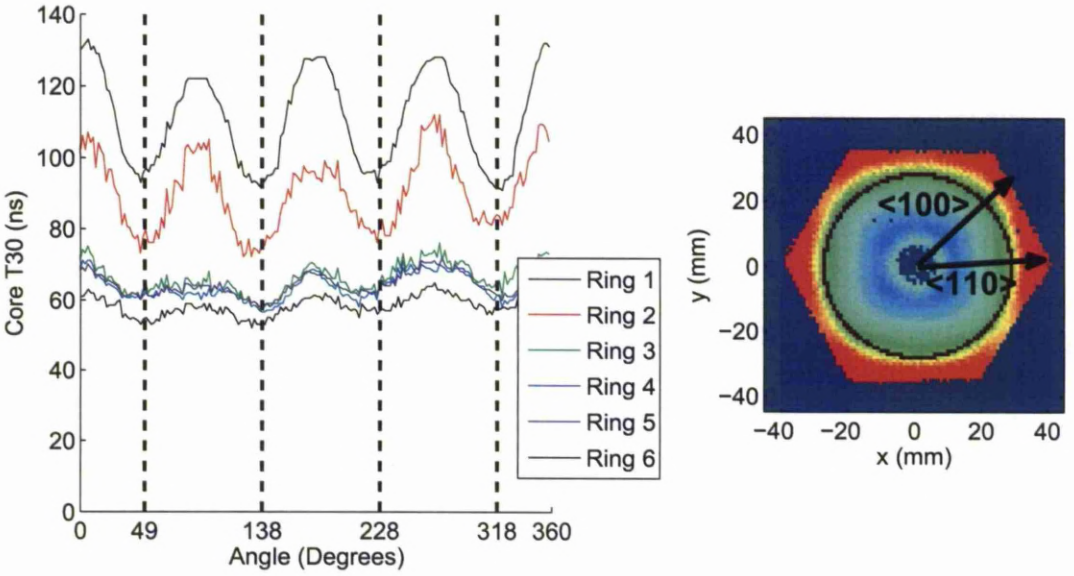

Figure 4.13: The variation in core T30 as a function of angle for each detector ring, measured at 28mm radius (left). The mean position of each minimum is shown as a dashed black line. The ring 3 core T30 map (right), indicating the positions used to plot the angular change in dark red and the first <100> and <110> axes directions as black arrows.

4.6 Side Singles Scan

After the completion of the front face singles and coincidence scans, the scintillation detectors were removed and the test cryostat reorientated to allow scanning from the side as shown in *Figure 4.14*. Once the detector was secure in this orientation it was scanned on a 1mm grid across its side profile for 30s per position over a total of 8075 positions. The trigger condition was again >400keV measured on the central contact. As with the front face scan the main limitations of this method are events that Compton scatter and deposit energy in multiple locations, and the uncertainty of the interaction position in the direction parallel to the collimator.

During the set up of the side scan, a loose connection to segment D1 was accidentally detached. This segment is missing from all of the side scan matrices presented below.

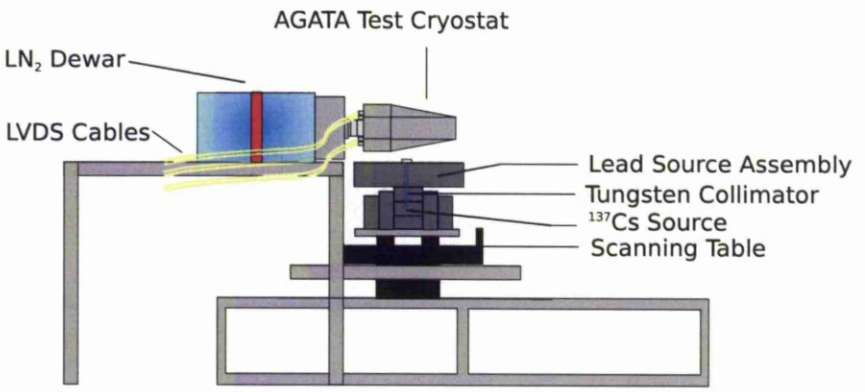

Figure 4.14: The Liverpool Scanning System [DBC+09] in side scan configuration. The AGATA cryostat is mounted and secured on a table with the HPGe crystal suspended over the scan table. The detector was orientated with the A/B segment boundary closest to the collimator and parallel with the collimation direction.

4.6.1 Intensity Matrices

Figure 4.15, shows the intensity of accepted triggers (left) and the intensity of fold 1 photopeak events (right) for the side scan. Despite variation in the thickness of the detector, the intensity of accepted triggers is roughly uniform with ≈10000 counts per position throughout the crystal. This is due to the limited rate of accepted triggers, which was reached when the collimator was pointed into any part of the crystal. A drop in count rate is seen near the outer boundary when the bean divergence starts to reduce the number of photons impinging on the detector.

The intensity of fold 1 photopeak events reveals the segmentation boundaries due to the decreased probability for energy to be confined to a single segment if the first interaction was near the boundary. The number of counts typically varies between ≈2000 in the centre of the thickest segments to ≈800 at the segment boundaries. The boundary between rings 1 and 2 is less well defined as its position varies with z due to the slopping field in the region. The sloping boundary also reduces the total number of counts here due to the increased probability of scattering between the rings.

Figure 4.16, shows the fold 1 intensity distribution for each sector in the detector. The variation in count rate between sectors is dominated by the attenuation of the beam as it passes through A and B before reaching sectors D and E. Sectors C and F are exposed

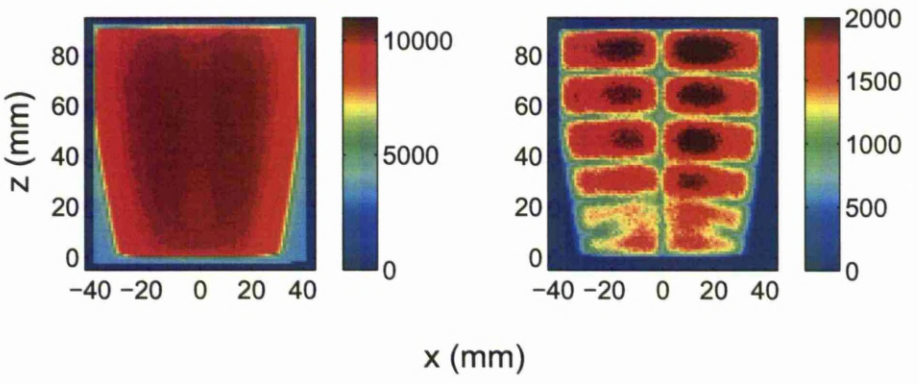

Figure 4.15: Number of accepted triggers for positions in the C001 side scan (left). Number of photopeak events confined to a single segment for the C001 side scan (right). This plot reveals the detector segmentation boundaries due to the reduced probability of the energy being confined to a segment when the collimator is close to a boundary. The boundary of rings 1 and 2 is less well defined due to the sloping electric field in these regions which results in the position of the boundary changing with z.

directly to the beam in the outer region, at larger distances from the core contact, but shielded from exposure in the inner section. In the intensity profile for sectors A and B, the boundary between segments in the coaxial region of the detector appear straight and parallel to the front face. In the sectors further from the source however, the segmentation boundaries appear to slope towards the back of the detector as they approach the core. This is the result of the slope of the electric field toward the back of the detector. The effect is hidden in the intensity spectra for sectors A and B as the majority of interactions are near the outside of the detector, where the segmentation is fixed by the boundaries of the contacts.

The sloping field can be seen more clearly in *Figure 4.17*, which shows the fold 1 photopeak intensity for each individual segment in sector A. There is a clear region of ≈10mm in z where rings 1 and 2 overlap, the size of the overlap then becomes less for each segment as the field becomes less sloped. Again, the total number of counts is much reduced in rings 1 and 2 relative to the others due to scattering between them.

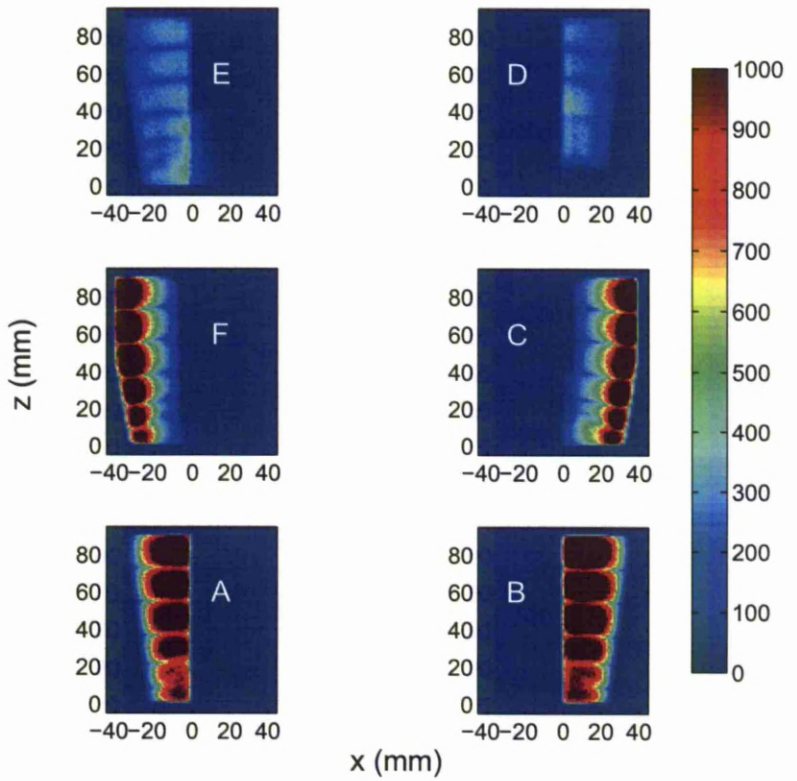

Figure 4.16: Number of photopeak events confined to a single segment for each AGATA sector. Sectors A and B were closest to the collimator, this means the beam had to pass through them to reach sectors D and E resulting in the low count rate there. The sloping electric field in rings 1 and 2 results in a degree of overlap in the intensity profile, obscuring the boundary between the two.

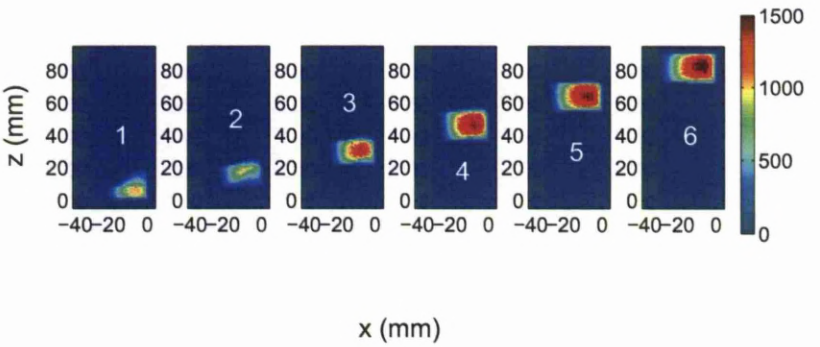

Figure 4.17: Number of photopeak events confined to each segment within sector A for the C001 side scan, the segment numbers are shown in white. The slopping electric field at the front of the detector is evident in the large region of overlap between the first two rings. Further back in the coaxial region the segment boundaries are parallel to the collimation direction and hence sharp boundaries are seen in the intensity distribution.

4.6.2 Rise Time Matrices

Figure 4.18 shows the core rise time distribution revealed by the side scan for sectors A and B. The T30 and T90 distributions are shown on the top and bottom respectively.

As seen earlier in the front face scan, the T30 varies between 40ns and 100ns in the bulk volume of the detector. It is largest near the outer contact where the moving charge starts farthest from the core where the weighting field is changing slowly, as the interaction position approaches the core the T30 becomes smaller. The largest T30 values of ≈120ns are found at the corners of ring 1 where the electric field is weakest, resulting in a unsaturated drift velocity for some proportion of the drift of the electrons toward the core.

The T90 distribution has a minimum of ≈220ns at intermediate radius, where the charge carriers have equal drift times before being collected at their respective contacts. Moving towards either contact results in a longer T90 as one of the charge carriers continues to drift after the other has been collected.

The trends in both T90 and T30 are less sharply defined in the side scan data than the front face scan. This is sue to the charge collection direction being in different directions relative to the collimated gamma-ray beam, for different positions in the crystal. For a given collimator position, gamma rays will interact at sites with a range of rise time characteristics.

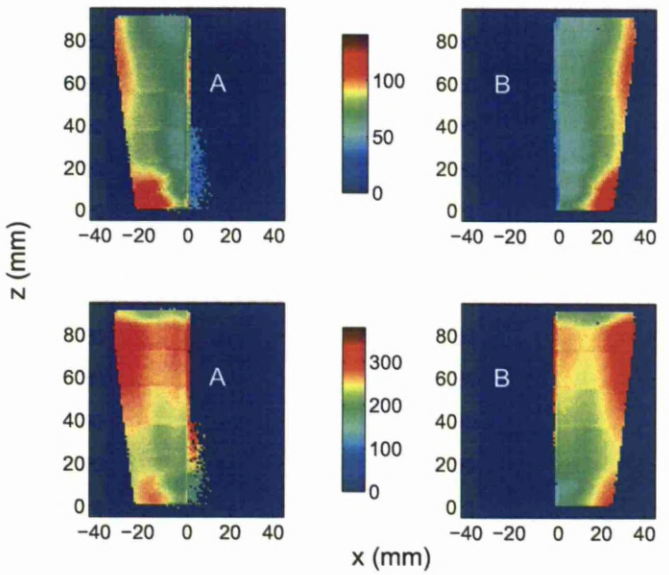

Figure 4.18: Core T30 (top) and T90 (bottom) for fold 1 photopeak events in sectors A (left) and B (right). The core T30 is generally larger near the outside of the detector, this is due to the shallower slope of the core weighting potential in this region. The maximum values are seen near the corners of ring 1 where the electric field is weakest. The T90 distribution has the smallest values at intermediate radii where the holes and electrons have equal collection time, and increases toward either contact. The true degree of this pattern is hidden due to the collimated beam passing through parts of the crystal covering a range of radii.

4.7 Depletion Surface Scanning

When the detector was first mounted on the scanning table a series of fast singles scans on a 2mm basis were carried out at a range of bias voltages. This allowed us to study the depletion surface as it moved, with increasing voltage, from the outer contact of the detector to the core. *Figures 4.19 to 4.21* show the resulting intensity matrices for rings 1,4 and 6 respectively.

The method for generating these plots was the same as for the full bias intensity plots described earlier. A collimated source was scanned across the front face of the detector and all events for which the core energy passed the CFD threshold were digitised and written to disk. As the gain of the detector varies with applied bias the CFD threshold had to be readjusted for each new bias voltage, it was set to approximately 150keV for each run.

The data were sorted offline and position matrices incremented for all events for which the photopeak energy was confined to a single segment. Gain matching data was not recorded for all voltages due to time constraints, so the photopeak energy gates had to be set independently for each segment and each bias voltage.

Figure 4.19 shows the intensity matrices for ring one. There is already a significant count rate throughout this ring at 50V applied bias, because the detector depletes from the outer contact inwards. This means the front face of the detector has a depleted layer just beneath the surface even before bias is applied due to the natural depletion region. As the bias increases, the penetration of this region into the crystal grows and a higher number of gamma rays interact in the active volume, resulting in increasing counts in the intensity matrix.

The increasing count rate in ring 1 reaches a maximum at 750V, before dropping again at higher voltages. This effect is not due to movement of the depletion surface within the ring but to an increase in the system dead time as other rings become depleted. Initially, all of the recorded counts at smaller radii are due to interactions in ring 1 near the front face. As rings further back become depleted, the maximum accepted count rate of 420cps must be divided between trigger requests due to interactions elsewhere.

Figure 4.20 (Ring 4) and *Figure 4.21* (Ring 6) show the behaviour of the bulk volume of the detector. Initially, at 50V there is only a thin depleted layer near the surface of the detector. As the applied bias increases, this region spreads towards the core. The depletion

surface moves more quickly through ring 4 than ring 6 as the impurity concentration is lower, this means the electric field required to deplete the detector of all free charge carriers is less.

These measurements allowed us to ensure that the detector was fully depleted by the time it reached its full operating voltage of 4500V. In addition, it provided a check on the impurity distribution, a crystal with its purest end at the back of the detector would have

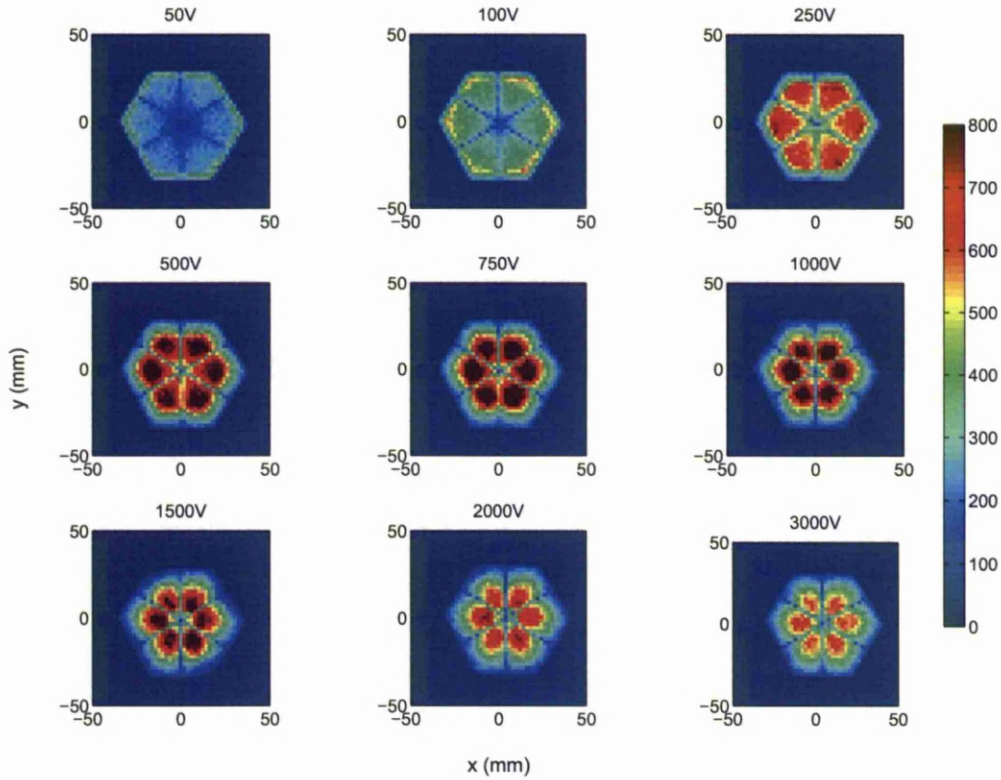

Figure 4.19: The ring 1 photopeak intensity matrices for a range of applied bias voltages. The intensity of photopeak events for which the deposited energy is confined to a single segment, for a range of bias voltages. The detector depletes from the outer contact, in ring 1 there is already a significant depleted depth throughout the radial range at 50V bias. The intensity increases with bias until 750V when a maximum is reached. This is due to the system dead time increasing as the depletion surface spreads through the detector and the accepted count rate must be shared between more segments.

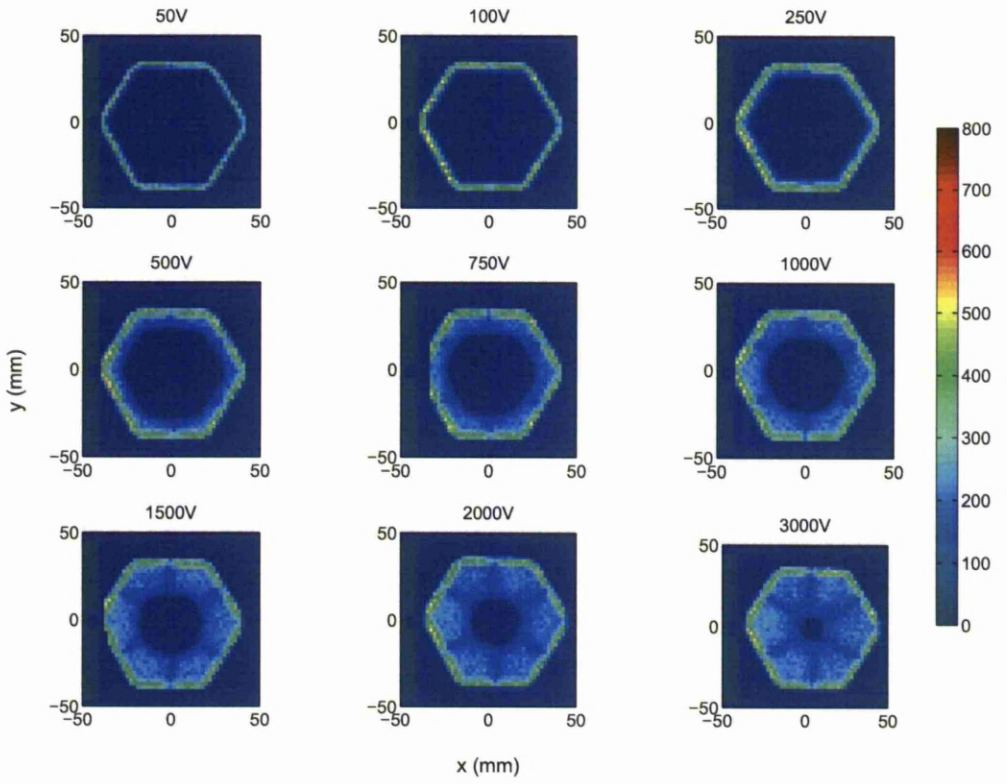

Figure 4.20: The ring 4 photopeak intensity matrices for a range of applied bias voltages. The intensity of photopeak events for which the deposited energy is confined to a single segment, for a range of bias voltages. At 50V applied bias only a small region of germanium near the outer contact is depleted of free charge carriers. As the bias increases this depleted volume spreads into the crystal toward the core.

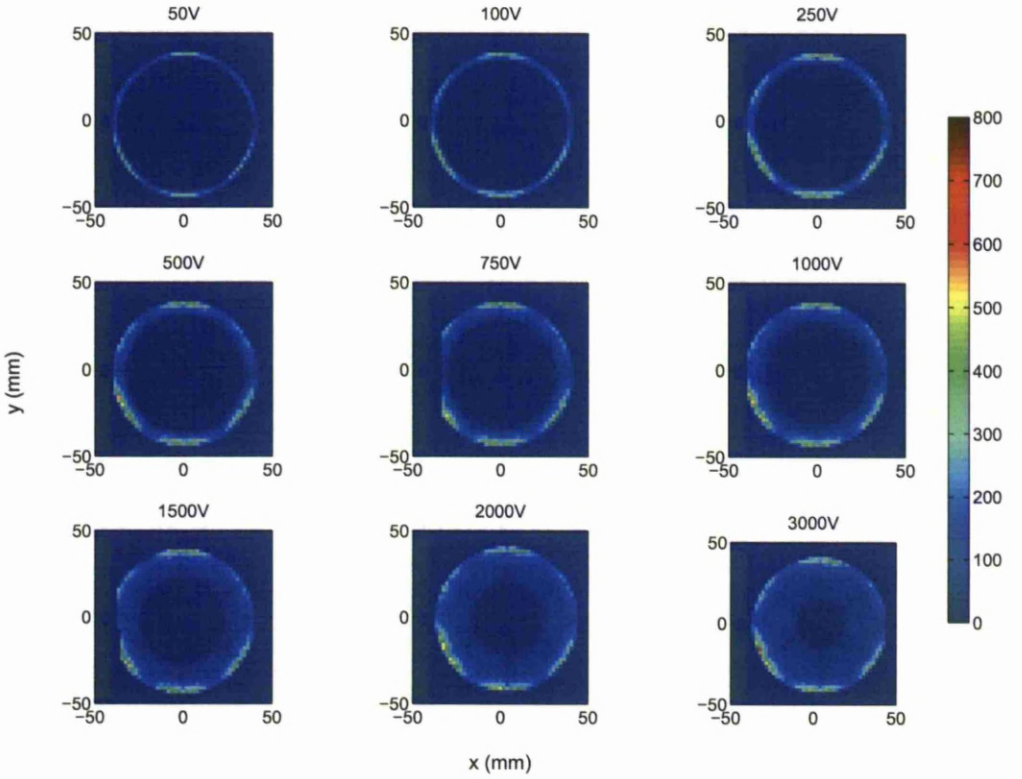

Figure 4.21: The ring 6 photopeak intensity matrices for a range of applied bias voltages. The intensity of photopeak events for which the deposited energy is confined to a single segment, for a range of bias voltages. At 50V applied bias only a small region of germanium near the outer contact is depleted of free charge carriers. As the bias increases this depleted volume spreads into the crystal toward the core.

Chapter 5

Coincidence Measurements

The central motivation for the characterisation measurements performed on AGATA detector C001 was to test the accuracy of the simulated signal shapes. To achieve this goal it is necessary to observe the signal produced by the detector for gamma-ray interactions at precisely determined single sites within the crystal. The coincidence scan provides a method of identifying such interactions by combining the two-dimensional localisation provided by the collimated source, with a secondary scatter collimator and detector.

5.1 Coincidence Scanning Method

A beam of 662 keV gamma rays, perpendicular to the detector front face, was positioned using the Parker scanning table, as described in *Section 4.4*. A series of secondary lead collimators were positioned around the AGATA cryostat, these allowed scattered gamma rays to escape if the scattering angle was close to 90° and the interaction occurred at one of six narrow ranges in the z axis. NaI and BGO scintillation detectors were positioned to cover the gaps in the secondary collimators and detect any scattered gamma rays, the arrangement is shown in *Figure 5.1*. By *Equation 2.5*, a gamma ray scattering in this manner will deposit 374 keV in the AGATA HPGe crystal and 288 keV in the scintillator. *Table 5.1* shows the position of each collimator along the z axis and the ring with which each was aligned. The positions of the collimation gaps were measured to 0.1mm precision with vernier callipers, there was a greater degree of systematic uncertainty in the position relative to the crystal which will be assessed in *Chapter 7*. The collimator openings were

1.5mm wide at the first three depths but were widened to 3mm further back to compensate for the reduced count rate due to attenuation of the incoming gamma ray beam at the expense of precision in the position.

Depth (mm)	AGATA Ring	Width (mm)
4.3	1	1.5
16.1	1&2	1.5
31.7	3	1.5
49.3	4	3.0
66.4	5	3.0
85.1	6	3.0

Table 5.1: The position of each secondary collimator depth along the z axis, parallel to the core. Most of the collimators were aligned with a single ring in the detector however, due to the sloping electric field near the front of the detector, the collimator at 16.1mm was aligned with rings 1 and 2. The collimator widths were increased towards the back of the detector to increase the count rate at the expense of precision in position. The positions and widths were measured to 0.1mm precision however there is some systematic uncertainty in the position of the collimator array relative to the detector crystal.

The finite width of the collimators results in a divergence of the incoming and scattered gamma rays. *Figure 5.2* shows the variation in spot size projected by the primary collimator (top), and the height of the region from which gamma rays can reach the scintillation detectors (bottom). The figures are based on a simple geometric approximation and assume that the collimators function perfectly i.e. no gamma rays pass though any part of the collimator material. It is assumed that a scattered gamma ray takes the shortest path through the crystal to the scintillation detector.

A total of 40 BGO detectors were used to cover the secondary collimator gaps. Due to the limited number of available preamplifier and ADC channels the signals were summed in groups of 3-5 resulting in 12 BGO channels to be instrumented. Care was taken during set up to ensure BGO groups at lower z positions only covered the collimators from a single depth. This allowed the scintillators to be used to identify which depth the interaction occurred at. This was important for interactions in AGATA ring 1 which lined up with more than one collimator depth. The three NaI detectors were each instrumented separately and each

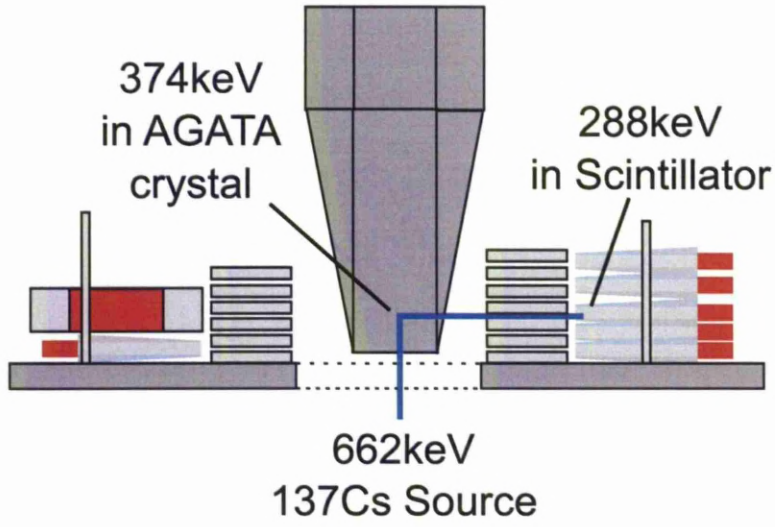

Figure 5.1: The precise location of gamma-ray interactions is established in the coincidence scan by requiring that the gamma-ray photon passes through the source collimator and into the AGATA crystal before scattering, via a secondary collimator, into a scintillation detector. A series of scintillation detectors and secondary collimators were used to allow six different depths to be scanned at the same time. The scattering angle of 90° determines that a 662 keV gamma ray will deposit 374 keV in the AGATA HPGe crystal and 288 keV in the scintillation detector.

covered the three secondary collimator depths at the back of the detector. The overlap was not a problem in this region as each AGATA segment lined up with a separate collimation depth.

Through the course of two months, the primary collimator was held for three hours at 362 different x-y positions, arranged in a series of azimuthal and line patterns (*Figure 5.3*). Data were collected simultaneously from each of the six depths, resulting in a total of 2172 interaction positions.

This coincident scanning system, combined with the trigger electronics described in *Section 5.2*, was designed to maximise the fraction of events made up by the single site interactions of interest. Despite the selectivity of the trigger system, the single-site, 90° scatter events made up less than 1% of the accepted triggers. To identify the correct events from the data a series of software filters were applied, this process is described in *Section 5.3.1*.

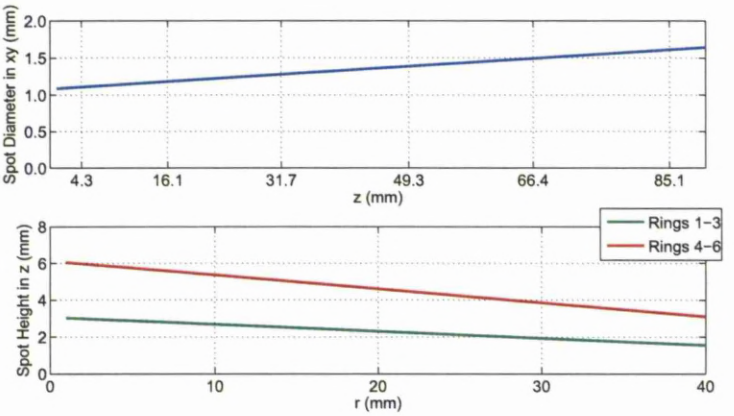

Figure 5.2: The divergence of the incoming and scattered gamma rays results in a variation in the collimator spot size as a function of position. The plot shows an estimation of the position precision based on simple geometric considerations. The top plot shows the diameter of the beam in the x-y plane, as a function of depth in the crystal. The lower plot shows the height of the region from which scattered gamma rays can reach the scintillation detectors as a function of the distance from the centre of the detector. The two lines represent the 1.5mm collimator gap used in the front three rings, and the 3mm gap used in the back three rings.

The signal from the detector included a noise component, the magnitude of which was dependent on the electrical and mechanical conditions. When the cryostat was mounted on the scan table the noise magnitude was greater than that achievable in optimum conditions due to the lengths of cables required and the microphonic effects induced by vibrations in the frame. The standard deviation of the noise was measured to be 7mV RMS on the core and 4mV RMS on the segments. The discrepancy between these values is the result of the larger capacitance of the core contact.

In order to minimise the noise, and reveal the underlying true signal, a mean response was formed from the signals at each position. The methodology used in forming the mean response is discussed in *Section 5.3.2.*

5.2 Scanning Electronics

Figure 5.4 shows the arrangement of electronics used for the coincidence scan, the details of each component are listed in *Table 5.2.* AGATA and the scintillation detectors are shown

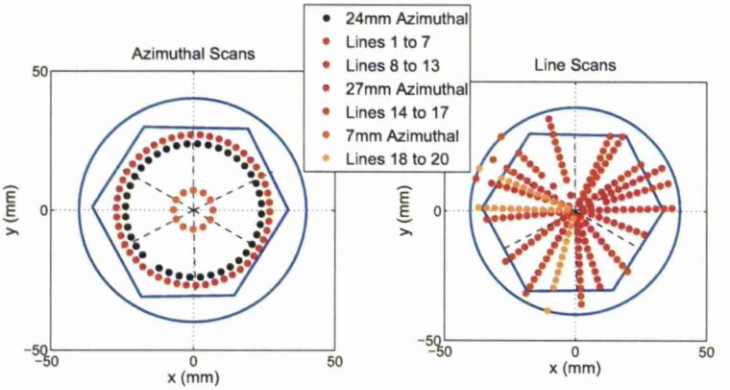

Figure 5.3: During the coincidence scan data were acquired from each of the primary collimator positions shown on the plot above, and from each of six depths defined by the secondary collimator positions. The acquisition was divided into seven runs, a limited singles scan covering only the centre of the detector was used between each run to check the alignment.

on the left in blue boxes. Preamplifiers were used to increase the gain of AGATA and the BGO scintillators however the photomultiplier tubes coupled to the NaI detectors were already of sufficiently high gain. BGO scintillator detectors have a very fast signal suitable for precision timing singles, however the preamplifiers used were slower which increased the rise time to ≈100ns.

The remaining electronic components are coloured to indicate that their output provides, a linear signal shaped to optimise energy measurement (red), a linear signal shaped to optimise timing (orange), or a digital signal to be recorded by the DAQ (green).

The ORTEC 671 amplifier and CAEN ADC were set up to measure the core energy in the same manner as for the singles scan. In addition to this, the CAEN spectroscopy amplifier and CAEN ADC measured the energy for each of 15 scintillator channels. The shaping time on the CAEN spectroscopy amplifier was set to 6μs. The lower level discriminator was set on each ADC channel to eliminate counts due to baseline noise.

The triggering of the system was controlled by the AGATA core signal and the 15 scintillator signals. The scintillator channels were first passed to a timing filter amplifier which increased the gain on the signal, while maintaining the fast rising edge. Leading edge discriminators were then used to check if the signals passed a critical threshold of ≈60

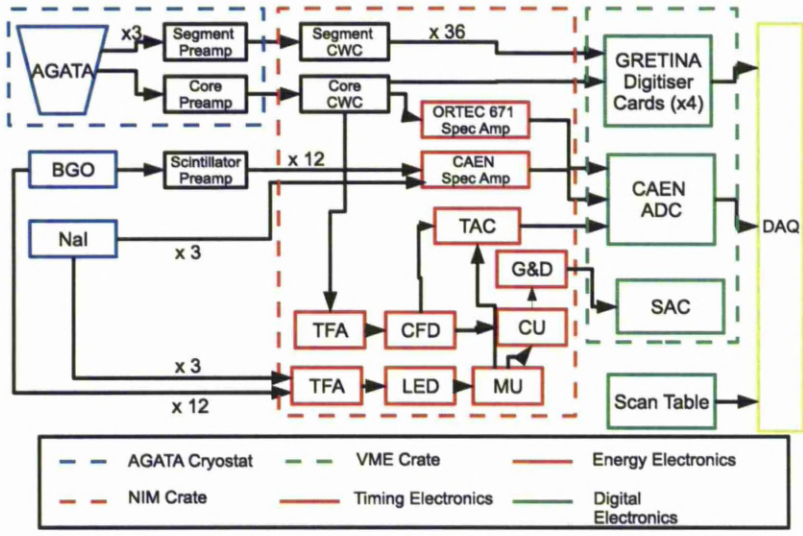

Figure 5.4: The electronics used during coincidence scanning. In addition to the readout and triggering electronics used for the singles scan, BGO and NaI scintillator detectors are used to detect gamma-rays scattered from the AGATA crystal. Analogue thresholds are applied to these detectors using leading-edge discriminators, after which a multiplicity unit is used to produce a logical OR signal. This is then combined in a logical AND with the AGATA trigger signal resulting in a final trigger signal which only accepts events with energy in AGATA and any one scintillator. The specific components indicated by each label are listed in *Table 5.2*

keV and produce a logic output signal for any that did. The multiplicity unit was set to produce an output when any one or more input signal was measured. The unit then acted as a logical OR of all the scintillator signals.

The trigger from the AGATA core was handled in the same way as the singles scan using a TFA and CFD, the CFD threshold was set to a lower value of 60 keV. A coincidence unit was then used to produce the logical AND of AGATA and the scintillator logic signal. The combined effect of these timing units was to produce a logic signal whenever both the AGATA core and any of the scintillators measured greater than 60 keV deposited. The width of the logic signals from the CFD and multiplicity unit were tuned to have a width of 50ns, which determined the coincidence window of 100ns.

The gate and delay generator was triggered by any signal from the coincidence unit, and produced a positive logic output of 20μs width, as required by the Silena ADC controller

(SAC). The SAC functioned in the same way as in the singles scan, monitoring the state of the other VME cards and accepting incoming triggers only if they were not busy writing the data from an earlier event.

The DAQ wrote to disk all of the data from the GRETINA digitisers and CAEN ADC, together with the position of the scan table, on an event by event basis.

Component	Label on Figure 5.4	Model
Coincidence Unit	CU	LeCroy 465
Constant Fraction Discriminator	CFD	ORTEC 584
Gate and Delay	G&D	Phillips Scientific 794
Multiplicity Unit	MU	LeCroy 380A
Time to Amplitude Converter	TAC	ORTEC 566
Leading Edge Discriminator	LED	LeCroy 821
Timing Filter Amplifier	TFA	ORTEC 863/474
ADC Controller	SAC	Silena S9418
Analogue to Digital Converter	CAEN ADC	CAEN V785
GRETINA Digitisers	GRETINA Digitiser	Berkeley Labs
Spectroscopy Amplifier	ORTEC 671 Spec Amp	ORTEC 671
Spectroscopy Amplifier	CAEN Spec Amp	CAEN N568
Converter Boxes	Core/Segment CWC	-

Table 5.2: The electronic components used for the coincidence scan. The specific layout is shown in *Figure 5.4*.

5.3 Data Filtering and Analysis

5.3.1 Initial Filtering of Raw Data

Once the data acquisition was complete, the event by event data were sorted offline to identify the ≈1% of events that constituted single site interactions at the correct position. The process began by checking if each event passed the following gates:

- **Energy** The requirement that a 662 keV gamma ray scatters through an angle of 90° imposes specific conditions on the energy deposited in each detector. *Figure 5.5* shows

a matrix of the energy observed on AGATA and the scintillation detectors, together with the individual energy spectra. The region corresponding to the 90° scattering events of interest can be seen at $E_{AGATA} = 374$ keV, $E_{Scintillator} = 288$ keV, and is highlighted in black.

A tight energy gate of 7 keV width was applied to the AGATA energy. The energy resolution observed on the scintillator spectrum was 138 keV FWHM. Both the poor intrinsic resolution of the BGO detectors, and gain drift observed between individual tubes summed to the same electronics channel, contributed to this. As a result of this poor resolution it was necessary to apply a gate of 150 keV width. Simulations performed by other members of the AGATA collaboration [Sch09a] have suggested that this should not influence the outcome as the selection of events based on energy is dominated by the tight gate applied to the AGATA energy. The combination of both energy gates reduced the total number of events to 1.6% of the accepted triggers.

The energy spectra in *Figure 5.5* have been compressed to 4 keV per channel to reduce the memory required to process the large 2D spectrum. Other features visible in the matrix include the ^{137}Cs photopeak at 662 keV, the annihilation peak at 511 keV, and the lead X-rays at 72 keV and 85 keV.

- **Segment Fold** If a gamma ray interaction occurred at a single site, all of the charge produced would be collected in a single segment. A gate was applied to reject all events where the energy was shared between more than one segment.

- **Scintillator Number** The scintillators and secondary collimators were arranged such that it was not possible for a 90° scatter event between certain combinations of scintillator channel and AGATA segment. If an event appeared to represent such a combination then it was filtered from the data.

The combination of all of the above gates reduce the number of events to 0.96% of the initial CFD triggers accepted by the DAQ. A large proportion of the remaining events were the correct single-site interactions of interest, however some random events remained. The final stage of filtering was a similarity test. As the events of interest for a particular position occurred at the same site, the signal shape was similar. Any remaining random events were distributed through the volume of the segment and had different signal shapes. In order

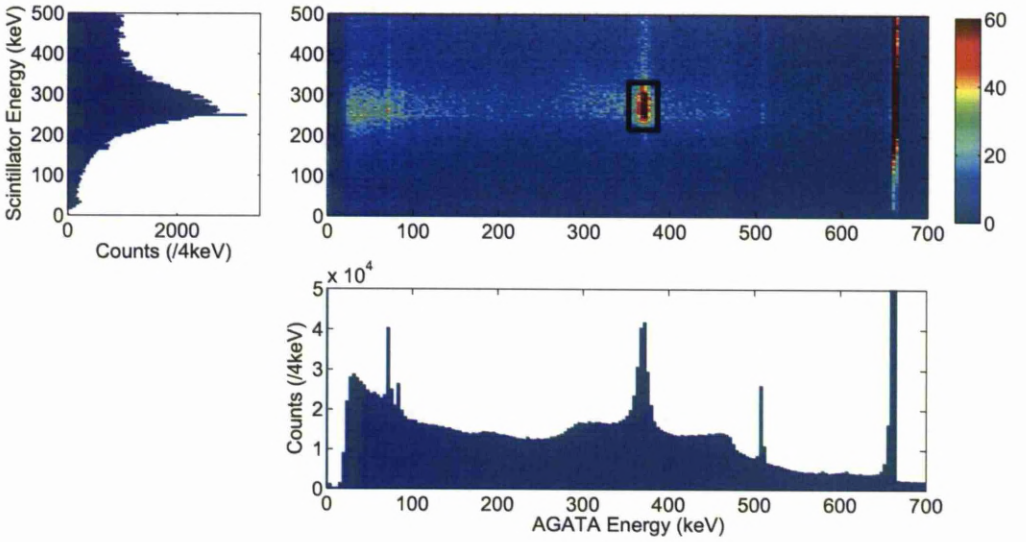

Figure 5.5: A matrix showing the energy deposited in AGATA and in the scintillator for all accepted triggers during the coincidence scan. Projections of the AGATA energy (bottom) and scintillator energy (left) are also shown. The region of interest, corresponding to 374 keV in AGATA and 288 keV in the scintillator, can be seen in the centre of the matrix. An increased rate of random coincidence is observed at AGATA energies corresponding to Pb-Xrays (≈80 keV), the annihilation peak (511 keV), and the ^{137}Cs photopeak (662 keV).

to identify the random events a preliminary mean signal was formed from all of the events that passed the initial gates. Each individual event was then compared with the mean and those that differed significantly were discarded before a final mean signal was formed, this method of filtering was also applied to previous coincidence scans performed using the AGATA symmetric prototype detectors [Dim08].

5.3.2 Mean Signal Formation

The position of each signal, within the range of digitised samples, varied due to the effect of baseline noise and variation in rise time on the CFD trigger point (known as *jitter* and *walk* respectively). This is illustrated in the leftmost panels of *Figure 5.6*. Before the mean response could be formed it was necessary to correctly align the signals.

Before alignment, the signals were normalised so that the maximum height of the real

charge pulse was 1. All image charge signals were scaled by the same factor as the hit segment signal. In order to improve the quality of the alignment the signals were interpolated to reduce the sample size to 2ns. A linear interpolation was first performed between each pair of successive samples. A smoothing algorithm was then applied which replaced every sample in the interpolated signal with the mean of itself and the two neighbouring samples.

Three methods of aligning the interpolated signals were considered, *t10*, *t90*, and *Difference Minimisation*, the resulting aligned signals are shown in *Figure 5.6*.

The t10 and t90 methods both relied on aligning the signals to a fixed fraction of their maximum height. The performance of this method depends on how quickly the signal is rising at the chosen point. In *Figure 5.6* the t10 method works best for the segment signal, which has a fast initial rise, but less well for the core signal which rises more slowly at the beginning. This situation is reversed for t90 alignment. A method was required that would perform well for all signal shapes.

The difference minimisation aligns the first signal to a fixed point. Each subsequent signal is then shifted relative to this and the RMS difference measured at each position. The alignment with the minimum difference was selected as correct. To minimise the effect of electronic noise on the alignment, only the core, interaction segment, and four immediate neighbours were used to calculate the difference and the measurement was only performed between the t10 and t90 points. Once all signals were aligned the initial, preliminary mean signal was formed.

Each event was then considered again and compared with the preliminary mean signal. A minimisation method was again used for alignment, this time to align each individual event with the preliminary mean signal. The minimum difference between each individual event and the mean was calculated and any events with a difference exceeding 0.04 in one segment, or exceeding a total of 0.2 across the six segments being considered were discarded. *Figure 5.7* shows histograms of the fit parameter measured for each important segment, for all the events in one experimental run, the cut off for individual segments is marked in red. The limits were chosen by a process of trial and refinement until the accepted signals looked sufficiently similar.

Figure 5.8 shows the formation of the mean signals for two real charge signals and an image charge, from a single position. Individual signals contributing to the mean are shown

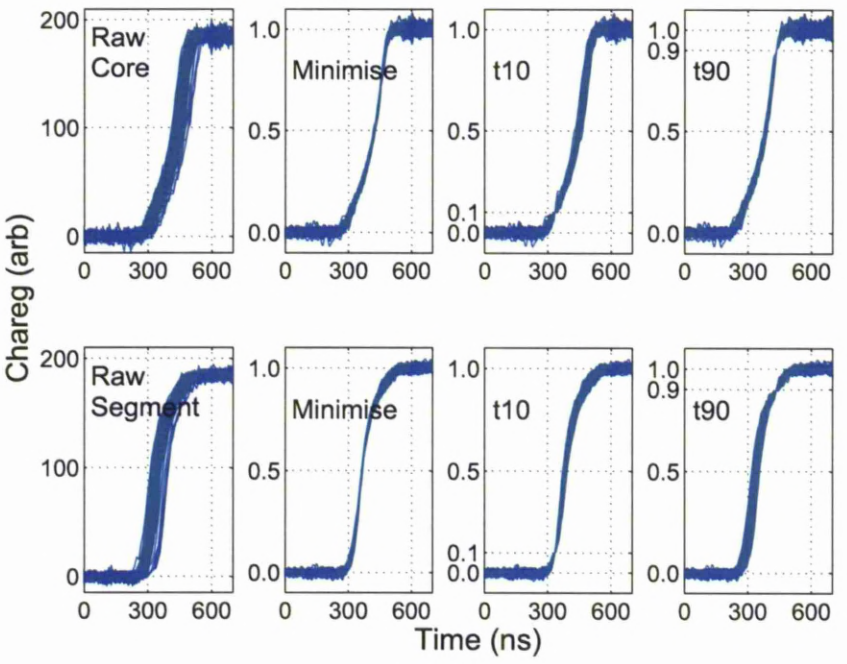

Figure 5.6: Three methods of aligning the signals before forming the mean were considered, *difference minimisation*, *t10*, and *t90*. The figure shows the three methods applied to the core (top) and hit segment (bottom) signals from a single interaction position. The raw signals (leftmost) have a range of positions due to *rise time walk* and *noise jitter* in the CFD trigger point. The t10 and t90 alignment methods each work well when the signal is rising quickly at the point of alignment (t10 in the case of the segment signal, t90 for the core). The difference minimisation method provides good alignment in all cases.

in blue, those that were rejected because they did not match the initial mean sufficiently closely in red, and the final mean in green.

5.3.3 Statistics and Uncertainty

The number of events remaining to form the mean signal after filtering varied with position in the crystal. *Figure 5.9 (left)* shows how magnitude of the baseline noise on the mean signal varied as a function of the number of events used to form the mean. The noise magnitude dropped sharply with the first few events, but this effect diminished with increasing number of events.

The minimum number of events used in the final mean was two as there was no way

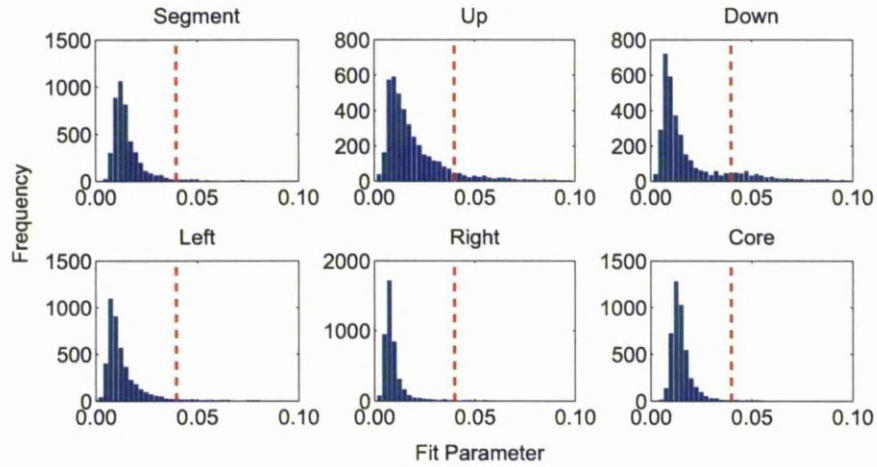

Figure 5.7: The fit parameter measured for all events in one experimental run. The parameter is calculated as the RMS difference between each signal and the initial mean formed from all signals. The alignment of each signal with the mean is varied until the minimum fit is found. If any signal had a fit parameter greater than 0.04 (red dashed line) then the whole event was excluded from the final mean. The total fit across all segments was also tested and required to be less than 0.2 for the event to be included in the mean. The total fit was normalised if the interaction occurred in rings one or six where only five segments are considered.

to perform the similarity test if only one event passed the initial gates. A maximum of 200 events were used for each position, this limit was imposed by disk space considerations when exporting the data from the DAQ. *Figure 5.9 (right)* shows the frequency of positions where different numbers of events were obtained, this distribution falls sharply from an initial maximum for two events and very few positions with more than 100.

Figure 5.10 shows how the number of events varied as a function of position in the crystal. The top row shows, for each ring, the number of events that passed the initial energy gates on AGATA and the scintillator, the second row shows the remaining events after the segment fold and similarity tests had been applied. Several factors play a part in determining this distribution:

- The attenuation of the 662keV gamma rays from the source leads to a general reduction in count rate as a function of depth in the detector.
- The attenuation of the scattered 288keV gamma ray leads to a drop in count rate as a

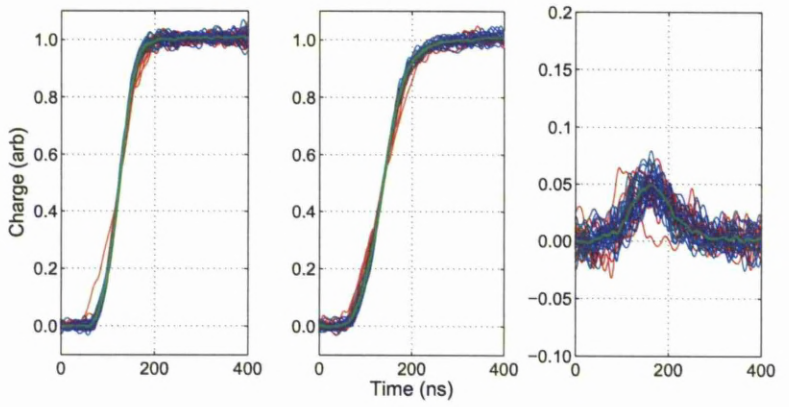

Figure 5.8: Mean signal formation for the core (left), hit segment (centre), and an adjacent segment (right) for a single position. Individual contributions are shown in blue, those that were rejected because they did not match the initial mean sufficiently closely in red, and the final mean in green.

function of distance from the outside of the detector. This effect is more pronounced than the attenuation through the depth of the detector due to the lower energy of the scattered gamma ray. At a fixed (x,y) position, this effect is more significant at high z due to the increasing width of the crystal.

- There is sporadic variation in the rate with the azimuthal angle. This is due to variation in how well the secondary collimator gaps were covered by scintillation detectors. Every effort was made to ensure the coverage was uniform but there were some physical limitations imposed by the geometry of the detectors and detector support frame.

- There is a drop in count rate at some positions near segment boundaries. The divergence of the gamma ray beam leads to events at some positions being divided over two segments. This reduces the number of events able to be formed into a single mean signal.

Finally, the third row shows the number of events, for each detector ring, passing the initial energy gates (1), that occurred in the correct segment (2), had all of their energy confined to that segment (3), and that passed the similarity test (4). These plots reveal that with increasing depth in the crystal, not only does the number of events drop, but also the fraction of events that remaining after filtering is complete. The explanation for this is

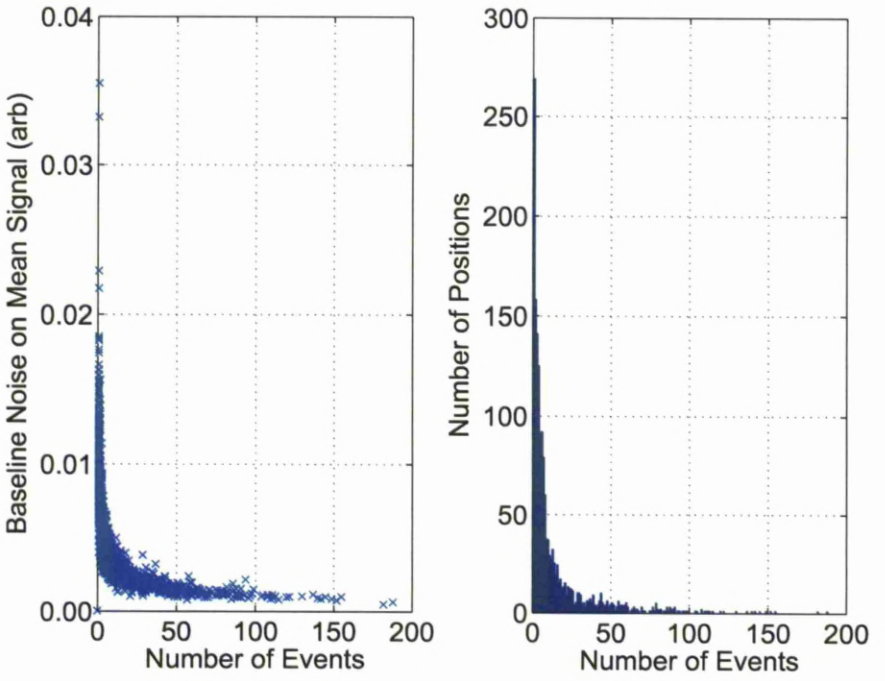

Figure 5.9: The variation in the magnitude of noise on the mean signal as a function of the number of events used to form it (left). The frequency of positions with certain numbers of events (right).

that while the rate of true, single site events drops as the interaction depth increases, the number of random background events is approximately uniform. This effectively reduces the signal to noise ratio of the measurement with increasing depth.

5.4 Mean Experimental Signals

The coincidence scan covered 2172 positions in the AGATA crystal, the key features of the mean signals from a selection of those will be reviewed in this chapter. Further evaluation of the results will be covered in *Chapter 7*, where a comparison between the mean experimental signals and the simulated signals will be made. *Figure 1.5* shows the relative positions in the crystal of each segment mentioned in the discussion below.

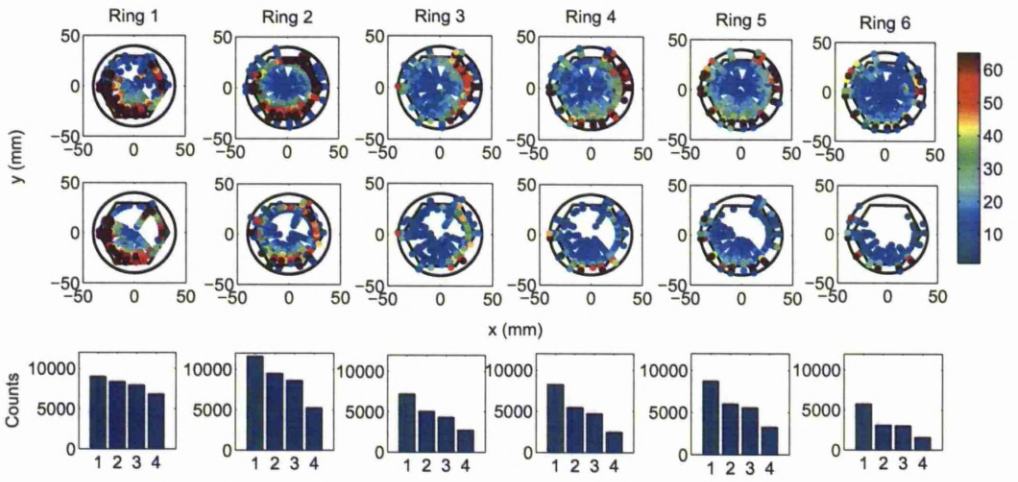

Figure 5.10: The top row shows the number of events, as a function of position, that passed the AGATA and scintillator energy gates applied in the first stage of sorting, for each of the six rings. The second row shows the number of events included in the final mean signal, after all stages of filtering were completed. The bottom row shows, for each ring, the total number of events at all positions that passed the initial energy gates (1), that occurred in the correct hit segment (2), that had the energy confined to a single AGATA segment (3) and that passed the test for similarity to the initial mean signal (4).

5.4.1 Line Scans

The 20 line scans each consisted of 13 points, equally spaced in a straight line, from the centre of the detector to the outside. The main source of variation in the signal shape along these lines if the change in drift distances of electrons and holes.

Figure 5.11 shows a line through segment F1, in the front detector ring at z=4.3mm, immediately adjacent to the boundary with segment E1.

- At points close to the centre of the detector, shown on the plot in black and dark red, the rise time of both the core and segment signals is very fast. The T90 for these signals is ≈70ns, which is faster than any other region of the detector. This is due to the short charge collection distance between the front face of the detector and the front of the core.

- The initial rise of the segment signal is very fast for all of the positions in this line.

This part of the signal is dominated by the collection of holes at the front surface of the detector which is less than 5mm from the interaction site.

- At larger radii, the final 40% of the segment rise is slower as the electrons are collected over a large distance at an angle sloping back into the detector.
- The core rise time gets longer at larger radii due to the increased charge collection distance for electrons.
- The image charge character for all the neighbours changes from positive, to bipolar, and then to negative as the radius of the interaction site increases. At small radius, the charge collection is dominated by the movement of holes towards the front face, this induces a positive signal on neighbouring segments. At larger radius the longer collection of electrons dominates the induced signal, resulting in slower, negative signals. At intermediate radii, the two charge carriers dominate at different points, resulting in a bipolar signal.
- The image charge magnitude is significantly greater for the left segment due to the proximity of the charge collection path.

Figure 5.12 shows a line scan through segment F5, in the fifth detector ring at 66.4mm depth, part way between the centre of the segment and the boundary with segment E5. These interaction sites are in the central bulk volume of the detector, the signal shape follows the classic pattern of more regularly shaped coaxial detectors.

- The core T90 in this line varies between ≈170ns and ≈260ns. The longest rise times are seen at small radius where the there is a sharp initial rise as electrons are collected at the core, but then a long slow drift of holes to the outer contact. The points of longest rise time are missing from the plot as there were not enough events to form a mean signal. Data from the singles scan suggests T90 values in excess of 350ns are to be expected at positions closer to the core. The fastest rise times are at intermediate radii when the drift time is equal for electrons and holes. Due to the higher drift velocity of electrons, this point is closer to the outer contact than the core.
- Segment T90 has a similar range and pattern to that of the core signal, with the slowest signals found for interactions near the core and the fastest for interactions at

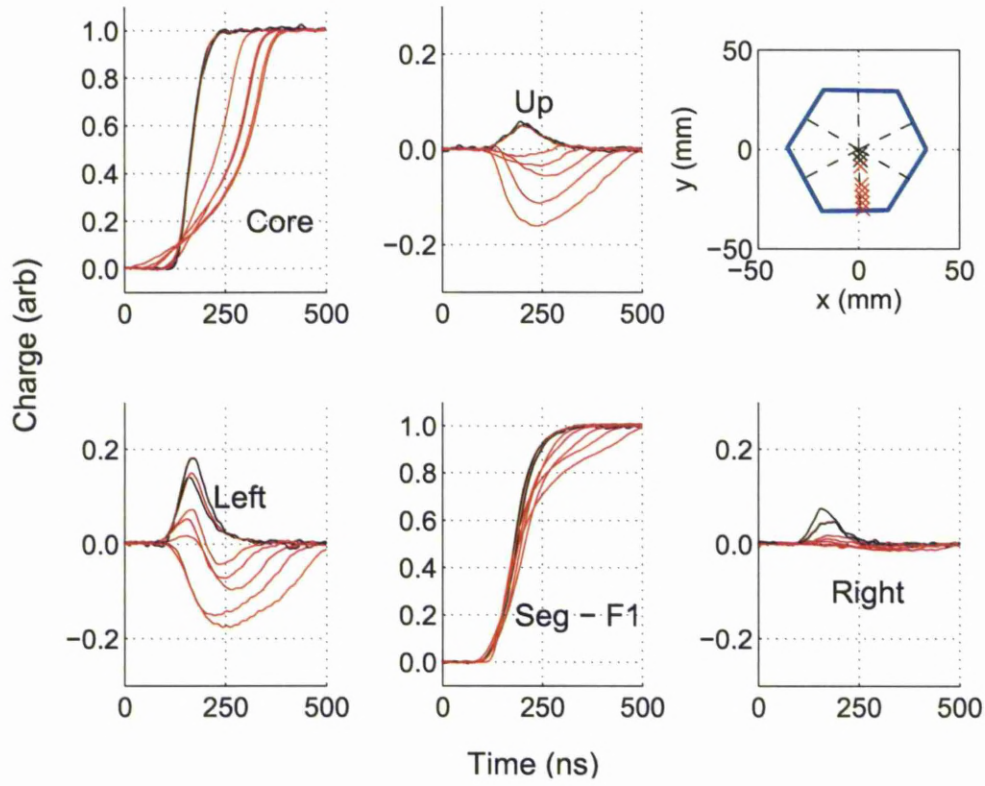

Figure 5.11: Line scan 9, through segment F1 at z=4.3mm, near the boundary with E1. The fastest rise times in the detector are seen at small radii here, where the charge collection distance, between the detector front face and core, is very small. The character of the image charge signals can be seen to vary as the relative collection distance of electrons and holes changes.

intermediate radii. The pattern for the initial rate of rise is reversed however. At large radii the segment has a very fast initial rise (T30≈ 30ns) as the holes are quickly collected, but at small radii the initial rise is very slow as the charge carriers have to drift a long way before the segment weighting field is sufficiently strong for them to induce a large signal (T30≈120ns).

- The image charge character shows the same variation from positive to negative as seen at the front of the detector. The left and right image charges are both small in this case as the charge trajectory is close to the centre of the segment.

- The image charge signals are much larger in segment F6 above then in segment F4

below. This is due to the closer proximity of the charge trajectory. The interactions are at 66.4mm which is only 5.5mm from the boundary with ring 6 at 72mm but 12.5mm from the boundary with ring 5 at 54mm.

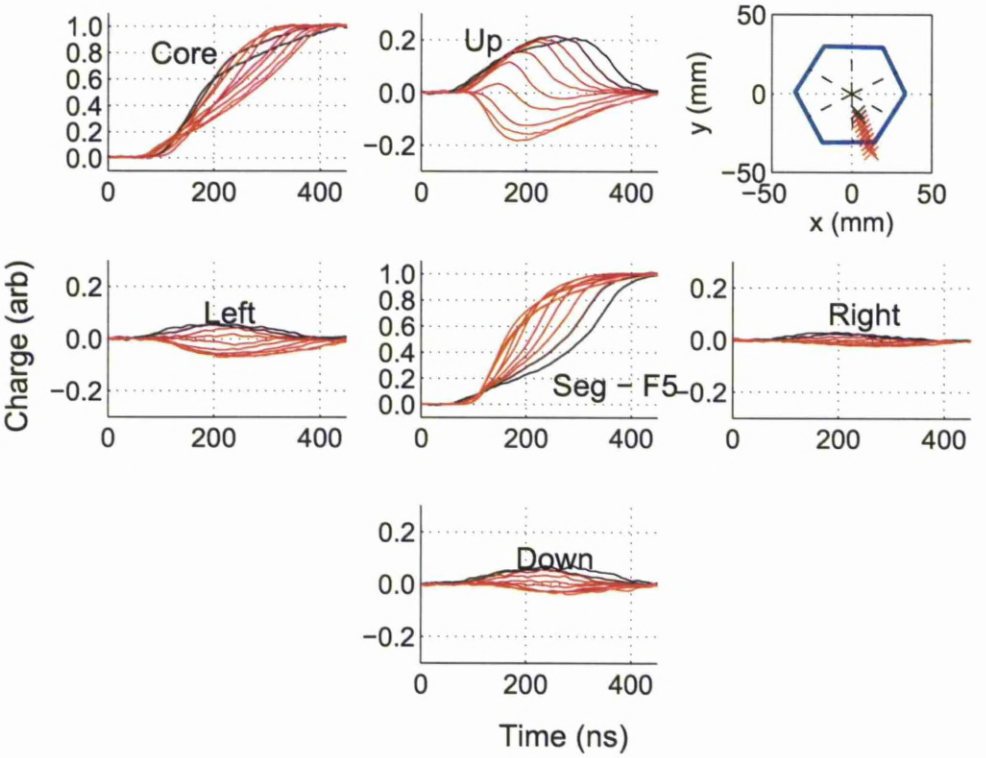

Figure 5.12: Line scan 17, through segment F5. There is large variation in the shape of the real charge signal due to differences in the drift distance of holes and electrons. The fastest rise times are seen in the region where charge collection time is equal for electrons and holes. The character of the image charge signals varies from positive, to negative, to bipolar as the dominant charge carrier changes.

5.4.2 Azimuthal Scans

The three azimuthal scans consisted of rings of points at constant radius. The main sources of variation in these signals are the proximity of the moving charge to the neighbouring segments, and the angle of charge collection relative to the crystal axis.

Figure 5.13 shows the section of the 27mm azimuthal scan passing through segment D1, in the front detector ring at a depth of 4.3mm.

- The core T90 varies between 170ns and 200ns through the range of positions plotted here. As the hole and electron drift distances are equal for all of the interaction sites, the variation is due to the direction of charge collection. The slowest rise time is seen at the centre of the segment which confirms the findings of the singles scan that this is the location of the <110> axis.

- The segment T90 follows the crystal axis in the same pattern as the core. The initial rise of the segment signals is faster due to short distance for holes to travel relative to electrons.

- The magnitude of the left and right image charges varies according to the proximity of the interaction site to each of the neighbour segments.

Figure 5.14 shows the section of the 27mm azimuthal scan running through segment A3 in the third ring of the detector at 31.7mm depth.

- The core T90 for these positions varies between 160ns and 175ns. As with the previous positions discussed, this is due to the variation in charge collection direction rather than differences in drift distance of charge carriers.

- The fast rise times and the strongly bipolar nature of the image charge in the segment above indicate that these positions are very close to the position of equal drift time for electrons and holes. This was not the case for the points in ring 1 on the same azimuthal scan discussed previously. This is due to the difference between the centre of segmentation and the centre of the central contact. The scan positions were defined around the segmentation centre which means that the position of the interaction along the line of charge transport varies with the azimuthal position.

- The magnitude of the left and right image charges is significantly smaller here than expected. This will be investigated in more detail in *Chapter 7*.

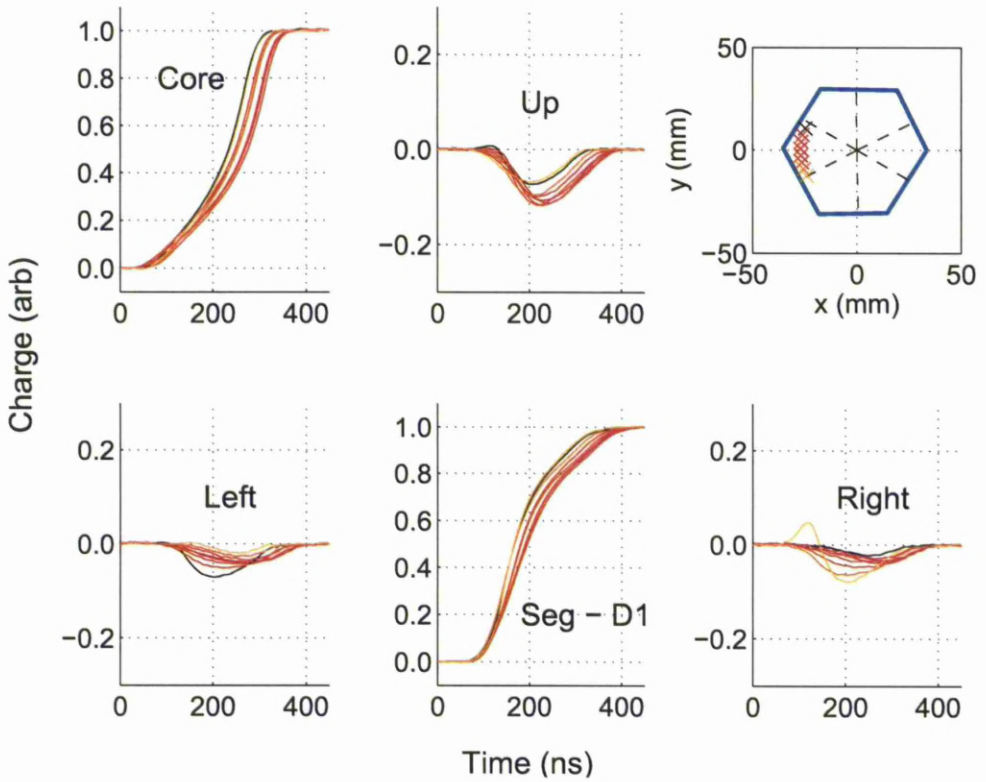

Figure 5.13: Mean Signals for positions on the 27mm azimuthal scan in segment D1. The variation in rise time is the result of varying angle of charge collection relative to the crystal axis. The left and right image charge magnitudes vary with the proximity of the interaction to the segment boundary.

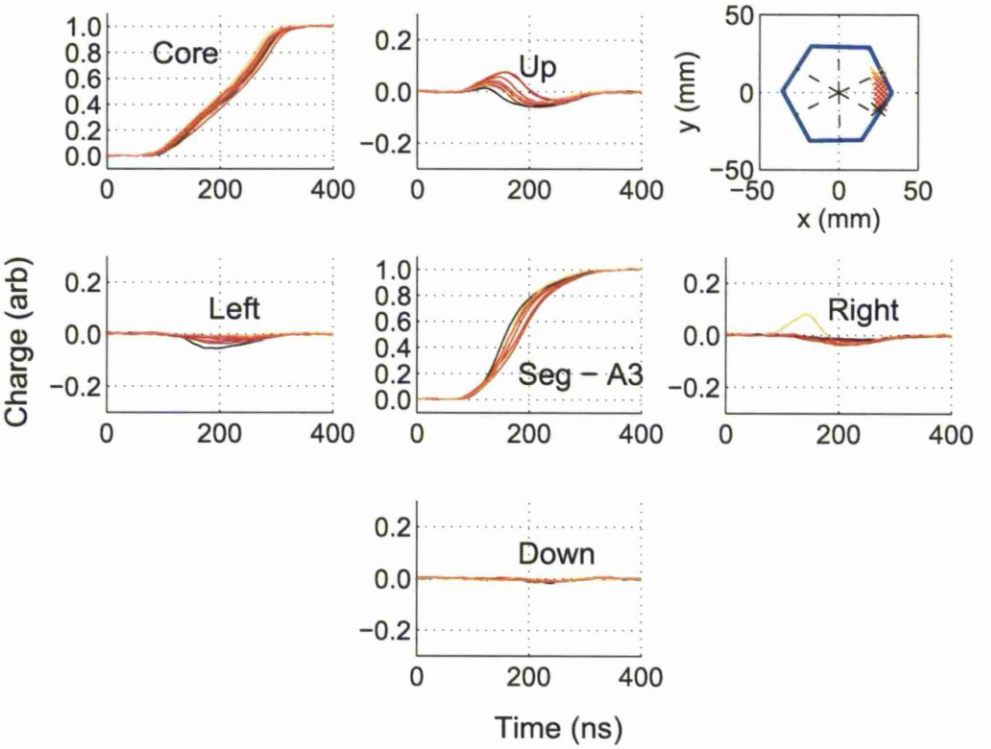

Figure 5.14: Mean signals for positions on the 27mm azimuthal scan in segment A3 at a depth of 31.7mm into the AGATA crystal. The variation in rise time of the charge pulses is due to the changing angle of charge collection relative to the crystal axis. The magnitude of signals induced to the left and right of the hit segment is smaller than expected here.

Chapter 6

Crosstalk Calibration

6.1 Crosstalk Introduction

Crosstalk is a spurious signal induced on one electronic channel due to a real signal on another. It is generally caused by a capacitive or conductive coupling between electronics channels. In segmented semiconductor detectors, there is a capacitive coupling between segments through the detector crystal itself. In addition, both the AGATA test cryostat and the AGATA triple cryostat [WHB+10], have a high density of internal electronic components. Although care has been taken in design and assembly to effectively shield the components, there is inevitably some degree of coupling between electronics channels.

It has been observed [Vet00], [Bru08], that the effect of this coupling in segmented detectors can be characterised using two components, *Proportional Crosstalk* and *Differential Crosstalk*. *Figure 6.1* shows the typical shape of the combined crosstalk signal.

Proportional crosstalk involves a net flow of charge from the hit segment to another. This results in the energy measured in the hit segment being smaller than the amount deposited. If the deposited energy is confined to a single segment, this effect is automatically compensated by the gain matching performed routinely on every channel. For higher fold interactions however, the total energy observed on all segments is reduced by a factor proportional to the number of segments in which real charge is deposited; in AGATA this amounts to $\approx$0.1% per segment. *Figure 6.2* shows segment-sum energy spectra collected using a ^{60}Co source both before (top, bottom left) and after (bottom right) a correction has been applied.

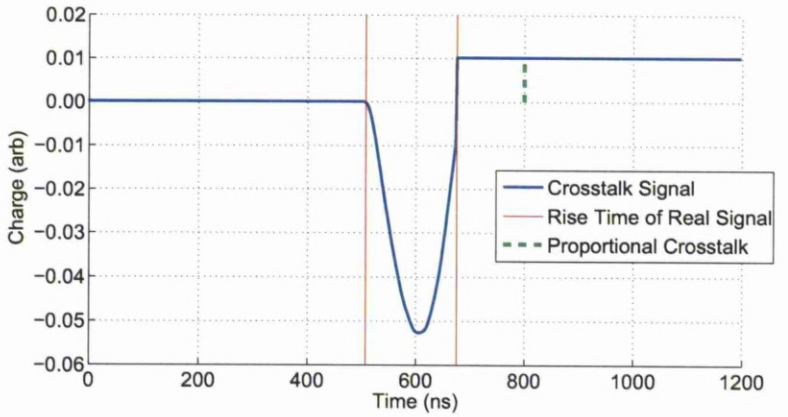

Figure 6.1: A schematic illustration of a signal induced by crosstalk between detector channels. The proportional component results in a net collection of charge in the segment, thereby affecting the energy measured by the detector. The residual signal due to this charge provides a simple means of measuring the proportional crosstalk but also means that a correction is vital in order to provide an accurate measure of deposited energy. The differential crosstalk component is proportional to the differential of the inducing signal. As this drops to zero once charge collection is complete, the signal is transient and leaves no residual once charge collection is complete.

As the magnitude of proportional crosstalk is dependent on the particular combination of segments, it also results in an additional source of uncertainty in core and segment energies. This causes an increase in the FWHM of peaks in the resulting gamma-ray spectra.

Two independent methods have been employed to measure the proportional crosstalk of AGATA C001 in the test cryostat, one based on observing the sum of the segment energies for fold 2 interactions, *Section 6.3*, and one based on the baseline offset of all segments for fold 1 interactions, *Section 6.4*.

Differential crosstalk induces a signal on each segment proportional to the differential of the signal on the segment being considered. As the differential drops to zero once charge collection is complete, this signal is transient and leaves no residual charge. If pulse shape analysis is not to be applied to the signals then this transient signal can be ignored as it does not affect the measured energy. For AGATA however it is necessary to quantify the degree of differential crosstalk if the observed signal shape is to be understood and fully characterised. An attempt has been made here to measure the differential crosstalk using

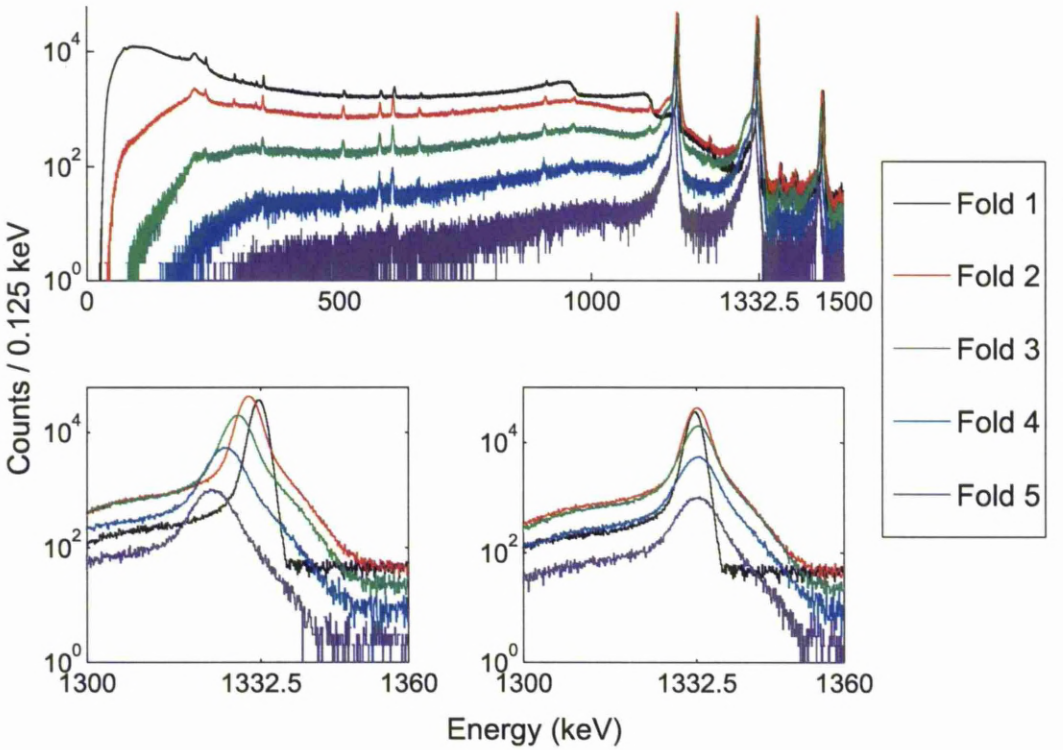

Figure 6.2: Segment-sum MWD energy spectra for a ^{60}Co source placed in front of the detector front face. The top plot shows the uncorrected full spectrum for events with energy spread over one to five detector segments. Spectra on the bottom show the region around the 1332.5 keV peak before (left) and after (right), a correction for proportional crosstalk is applied.

a technique developed for the GRETA collaboration [Rad10], *Section 6.6.*

An alternative method of differential crosstalk measurement [BRP06] has been employed elsewhere. This relies on using a low energy gamma ray source to look at the signals for interactions at a position on the surface of the detector, at the boundary of two segments. For the boundary of any two given segments (A & B), the signal produced on all other segments should be identical, as the charge collection trajectory is the same. Any differences between the signals observed on other segments when the charge is collected at A or B is due to the different crosstalk magnitude. This relationship can be used to extract the differential crosstalk parameters between A and B and each of the other segments.

6.1.1 Experimental Data

The three techniques employed here to measure the electronics response were all performed using the same dataset. The AGATA test cryostat was hung vertically from a large LN2 storage Dewar. Scattering material, such as the lead collimators used for the coincidence scan, and background sources were removed as far as possible from the detector. A 54kBq ^{60}Co point source was then placed 25.0±0.5cm from the centre of the detector front face.

The electronics arrangement was the same as that used for the singles scan, *Figure 4.4*. GRETINA FADCs were used to digitise the signals from all 37 detector channels at a sampling rate of 100MHz. The additional signals from the core preamp were used for a analogue energy measurement and to trigger the system. A trigger threshold of ≈40 keV on the central contact was set using a CFD.

The requested trigger rate was 2.1kHz, the accepted trigger rate was limited to 420Hz by the maximum data rate of the VME crate. A total of 5.6 x 10^7 events were collected over a period of two days producing 584GB of data.

6.2 Gain Stability and Linearity

An accurate measurement of the crosstalk in a detector requires both precise determination of the energy deposited in each segment and a large number of events over which to average the results. Meeting both of these criteria requires that the gain of the system is stable over the period required to collect sufficient statistics. In the particular case of the baseline offset method, it is also vital that the energy calibration is accurate to values as low as a few keV. Before the final crosstalk analysis was completed, a number of tests were made to ensure these conditions were met.

To investigate the stability of the detector gain, the data were divided into batches of 5x10^6 events. For each batch, an energy spectrum was created using the gain matched MWD value for the core and another was filled with the hit-segment energy. The core and segment photopeak centroids were then found for each individual batch. *Figure 6.3* shows the results organised according to the time of the measurement.

The variation with time is thought to be due to the ambient temperature variation in the lab. The temperature of electronic components can affect the preamplifier gain, while

variation in the crystal temperature can affect the average energy required to produce an electron-hole pair. The black dashed lines on the plot show the extremes observed during a similar measurement at IKP Cologne [BRW+09a], the greater variation is thought to be due to the LN_2 fill method. The Liverpool set up had the AGATA Dewar filled continuously from a large storage Dewar, while in Cologne, the AGATA Dewar was filled by hand at irregular intervals. As the AGATA Dewar was always full for the Liverpool measurement, the variation in gain was due solely to the ambient temperature variation and not to the fill level of the Dewar.

A correction for this gain variation was implemented on an event by event basis according to the batch number of the event being considered.

The baseline offset method of crosstalk calibration requires that small changes in the baseline position are measured for each segment whenever energy is deposited in another segment. In order for the measurement to be completed with sufficient precision, it is necessary to ensure that the ADCs used to measure the signal have a linear response down to this range.

Once all measurements on the AGATA detector were completed, the linearity of the GRETINA ADCs at low energy was measured using a Agilent 33220A programmable pulser. The pulser output was connected to two channels of one GRETINA card and programmed to provide a square pulse of the fastest possible rise time (2ns). The rate of the pulser was kept at 500cps which left a large separation ($\geq 1\mu s$) between each rising edge. The height of the signal was varied between 1 and 80 mV and both MWD and baseline offset energies were calculated for each pulse size. *Figure 6.4* shows the resulting spectra for one of the channels.

Once collection of the pulser data was completed, the peaks were fitted and a least squares fit to a quadratic polynomial was performed between the peak centroids and the pulser magnitudes. The results of these fits are shown in *Table 6.1* and plotted in *Figure 6.5*. To within the fitting error, the quadratic components of the fits, for both MWD and BD values, were zero. This indicates that, to within the range of pulse heights considered, the ADCs have a linear response.

Measurements using the GRETINA digitisers up to high pulse magnitudes have shown that there is some degree of differential non-linearity at the upper end of their range, but

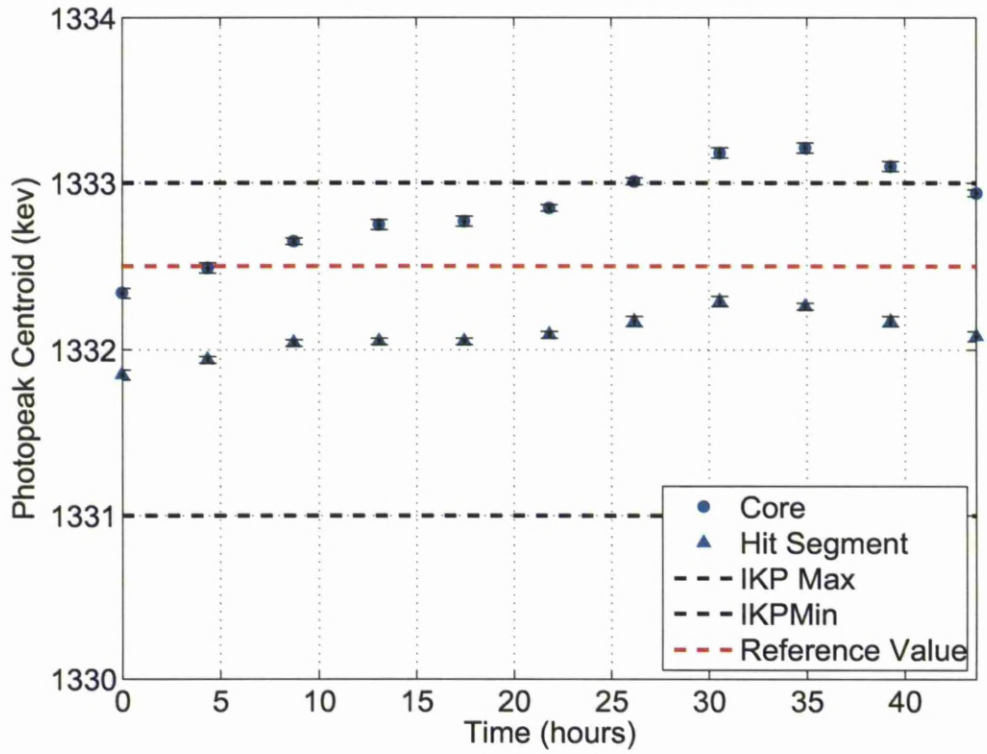

Figure 6.3: The position of the core and segment photopeaks for each batch of 5 x 10^6 events in the ^{60}Co crosstalk data. The movement in the centroid position is thought to be due to the gain variation due to ambient temperature changes. The data were corrected for this variation before the crosstalk analysis was conducted. The range of gain variation seen was less than that observed in a similar measurement at IKP Cologne [BRW+09a], this difference was due to the LN2 fill method. In Liverpool the AGATA Dewar was continuously filled from a large storage Dewar while in Cologne it was filled by hand at irregular intervals.

this was not relevant at the energies considered here.

6.3 Proportional Crosstalk - Energy Add-back Method

The energy add back method [BRW+09a] has been the primary method of crosstalk correction since the first segmented detectors. It allows the calculation of the mean crosstalk between pairs of segments but cannot deconvolve the individual contributions in each direction. It works by selecting fold = 2 events and measuring the average sum energy for

Channel	A	dA	B	dB	C	dC
Ch0 MWD	0.2×10^{-1}	0.2×10^{-1}	0.177×10^{-1}	0.2×10^{-3}	0.37×10^{-8}	0.5×10^{-7}
Ch9 MWD	-0.3×10^{-1}	0.2×10^{-1}	0.176×10^{-1}	0.3×10^{-3}	-0.2×10^{-7}	0.7×10^{-7}
Ch0 BD	0.4×10^{-1}	0.2×10^{0}	0.10×10^{0}	0.2×10^{-2}	0.1×10^{-6}	0.2×10^{-5}
Ch9 BD	0.6×10^{-1}	0.3×10^{-1}	0.99×10^{-1}	0.3×10^{-2}	0.3×10^{-5}	0.5×10^{-5}

Table 6.1: A table showing the values of the parameters for a fit of $y = A+Bx+Cx^2$ to the centroid channel and pulser magnitude. The values of the quadratic component of the fit are close to zero, showing that the ADC is linear within the range measured (1mV to 80mV).

every pair of segments.

The data analysis procedure was as follows:

- All energy values were gain matched.
- All events with segment fold = 2 were selected for the analysis. The mean of the first and last 30 samples were calculated from the digitised trace for each segment. If the change from the beginning to the end of the trace was greater than three times the standard deviation of the baseline noise, the segment was considered to have been hit.
- A gate is placed on the core MWD energy, only those events where the total deposited energy falls within the 1332.5 keV photopeak were considered.
- For each event passing these conditions, the sum of the energies of the two hit segments was calculated.
- A running average was kept of the segment sum energy for each pair of segments.

Figure 6.6 shows the resulting segment sum energies for all segment combinations. The numbering on the plot is organised such that all combinations involving segment A1 are listed in numeric order of the second segment, then all combinations involving A2 etc (A1-A2,A1-A3,...A1-F6,...F6-F5). Each combination has two entries in the plot, one for each ordering of the two segments.

The first noticeable feature of this plot is the greater than expected degree of crosstalk measured. The mean segment sum energy is 1326.8 keV which equates to crosstalk of 0.43%, significantly higher than the expected 0.1%. *Figure 6.7* shows the fractional crosstalk for

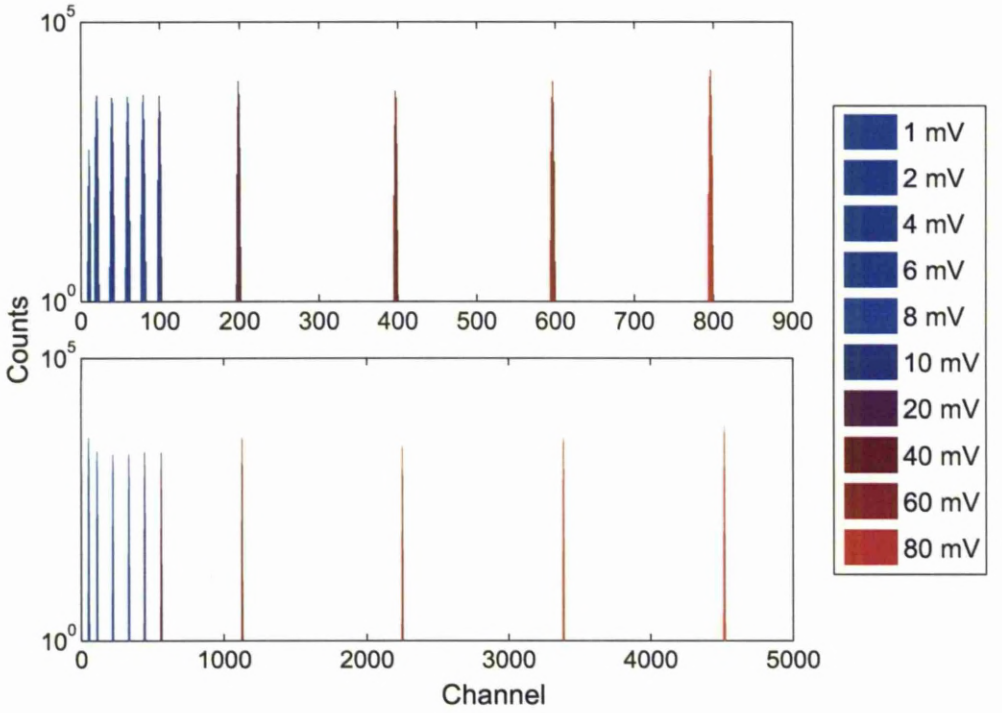

Figure 6.4: Spectra showing the baseline difference (top) and MWD (bottom) energy for a range of square pulse inputs to one channel of a GRETINA digitiser. The pulser signal had a rise time of 2ns and was repeated at a frequency of 500Hz until there were approximately 1000 counts in each peak centroid. The baseline difference energy was calculated in software from the digitised traces, the MWD energy was calculated by the GRETINA card's on-board FPGA.

each segment pair. The segments have been renumbered according to ring number on this plot, and each pair of segments have been recorded twice i.e. (x,y) and (y,x).

The diagonal lines either side of the central diagonal show the crosstalk for vertical neighbour segments. These values are significantly lower than the average, this is due to the mutual crosstalk between the two segments which reduces the magnitude of the reduction in sum energy. Other expected trends however, such as the reduced crosstalk in ring 2 due to smaller segment capacitance, are not visible.

The reason for this anomalously high crosstalk lies in the MWD calculation on-board the GRETINA digitiser cards. *Figure 6.8* shows the MWD energy on the AGATA core plotted against the energy measured from the same signal using the analogue spectroscopy

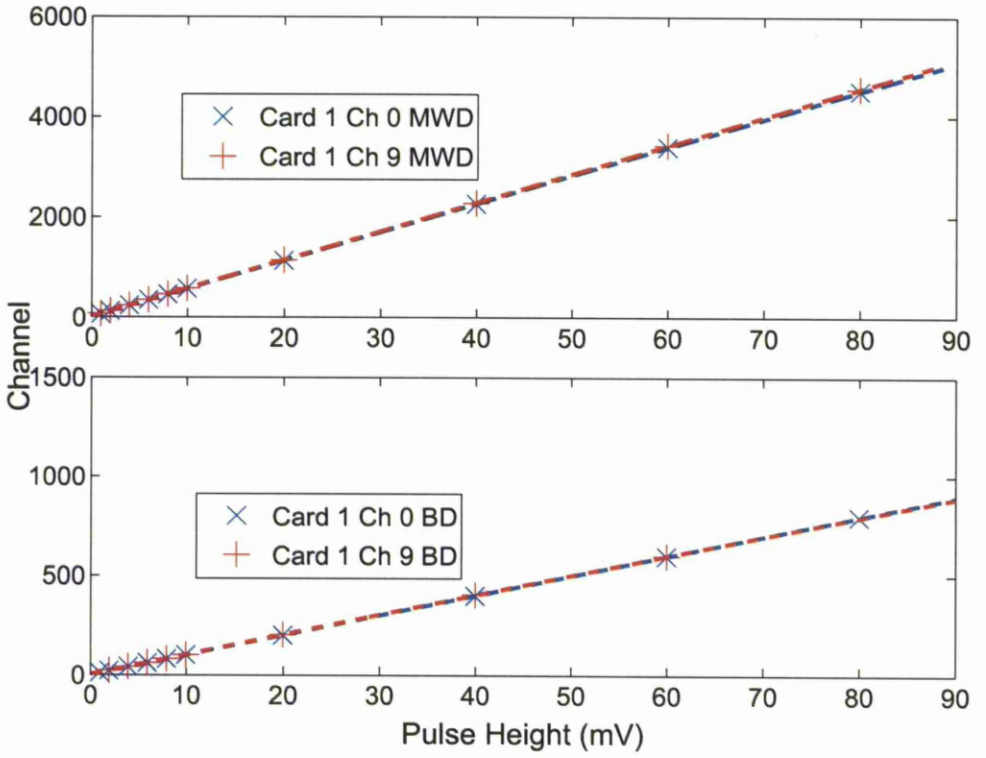

Figure 6.5: The results of a least squares fit of the MWD (top) and baseline difference (bottom) energy values to the pulse height of the input signal. Two GRETINA digitiser channels were tested and found to have excellent linearity down to the minimum pulser height of 1mV.

amplifier. The left hand plot shows the full range and the right hand plot shows the region around the photopeaks. Approximately 92% of the events lie on the line indicating equal energy measured by both methods. The remaining 5% however show a reduced MWD energy relative to the analogue measurement. The strong lines showing photopeak energy for the analogue system but a continuum below the photopeak for the corresponding MWD energy indicate that this is a problem with a reduced MWD energy, rather than an increased analogue energy.

Once this problem was identified, filters were added to all of the sort procedures used in this thesis to reject those events for which the two energy measurements differed. There was no way to implement this for segments however, as we had only one analogue energy measurement connected to the DAQ. As such, an accurate crosstalk calibration was not

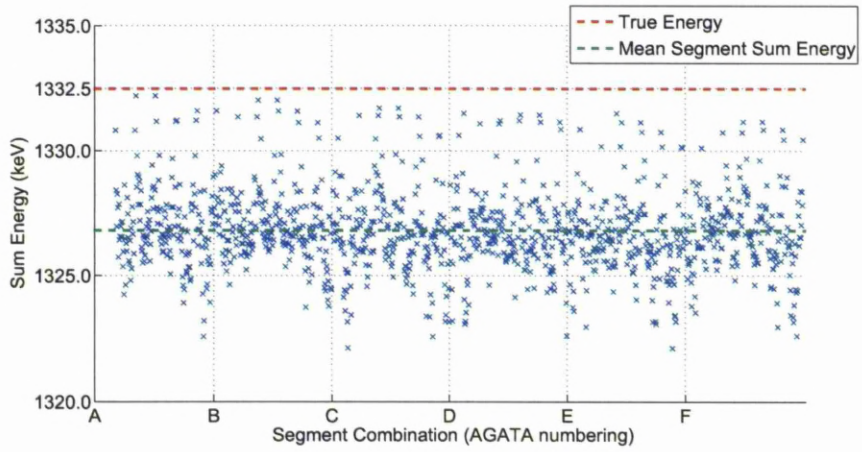

Figure 6.6: A plot of the segment sum energy for all fold 2 events. The position on the x-axis indicates the combination of hit segments using the AGATA numbering scheme, first all combinations with A1 (A1-A2,A1-A3...A1-F6) then all combinations with A2, etc. Duplicate entries are shown i.e. (x,y) and (y,x). The true gamma-ray energy is shown by the red dashed line. All combinations are expected to fall below the true energy due to crosstalk, however, the difference measured here is greater than the expected magnitude of $\approx$0.1%.

possible using the energy add-back method and another approach had to be considered.

6.4 Proportional Crosstalk - Baseline Offset Method

An alternative approach to crosstalk calibration is described in [BRW+09b]. This method is based on selecting events with the energy confined to a single segment and then measuring the baseline offset of each of the other segments. Using this procedure, the symmetry between segment pairs is broken. Capacitive coupling between segments is symmetric but each will have a different coupling to the core, this results in an effective difference in the exchange of charge when one or the other is hit. The energy add-back method of crosstalk calibration does not distinguish the direction of crosstalk, so a mean of the crosstalk in each direction is measured. When using the baseline offset method however, the crosstalk is measured independently in each direction between a segment pair.

The analysis procedure was as follows:

- All energy values and digitised traces were gain matched.

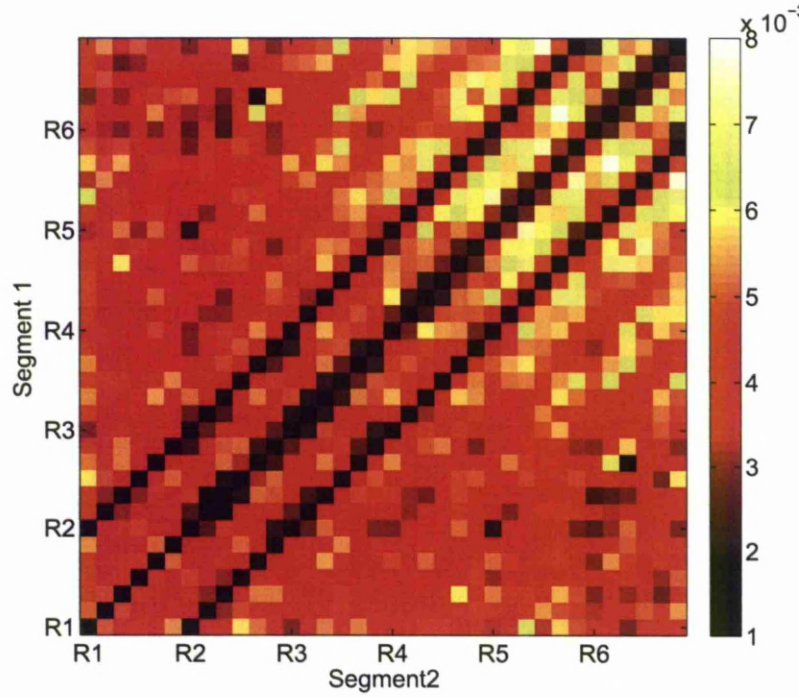

Figure 6.7: A plot of the fractional crosstalk measured for all segment combinations using the energy add-back method. The segments are numbered here according to ring number first (R1-R6), then sector (A-F). Entries for each segment pair have been mirrored to fill the entire matrix. The values vary up to 0.8% which is greater than the expected value of ≈0.1%. The strong lines of low crosstalk, parallel to the central diagonal, show the reduced effective crosstalk due to mutual exchange of charge between vertical neighbours. Other expected trends such as the reduced crosstalk to ring 2 are not visible.

- All events with segment fold = 1 were selected for the analysis. The mean of the first and last 20 samples were calculated from the digitised trace for each segment. If the change from the beginning to the end of the trace was greater than three times the standard deviation of the baseline noise, the segment was considered to have been hit.
- For each segment, 35 2D spectra were created, one for each of the other segments. The spectra were incremented with the energy on the hit segment vs the baseline shift measured in each of the others.
- From these spectra the mean baseline offset, as a fraction of deposited energy, was

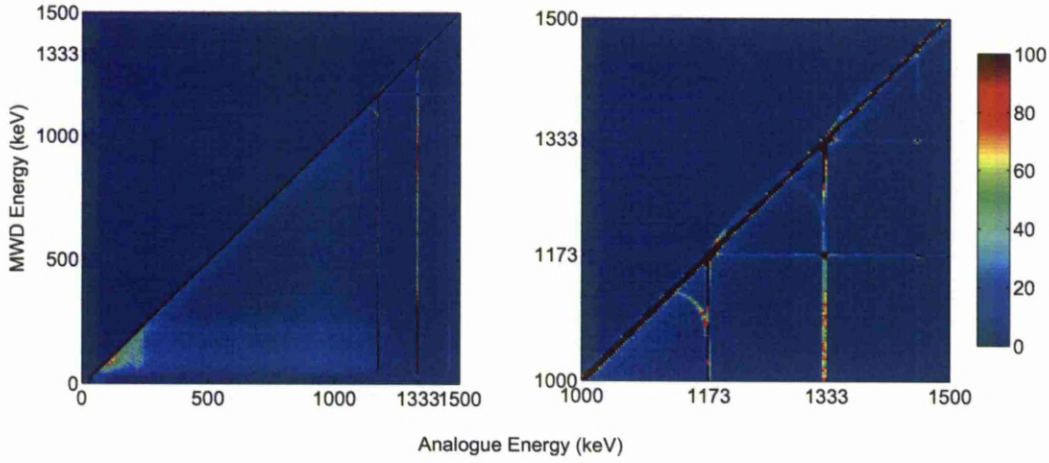

Figure 6.8: A plot showing the energy measured on the core by the MWD algorithm and by the analogue spectroscopy amplifier and ADC. For ≈5% of events the MWD algorithm measures a lower energy than the analogue system. The strong lines on the plot with the analogue energy at the photopeaks and the MWD energy somewhere below, indicate that the MWD energy is in error. All of the data presented in this thesis has been filtered to ensure the core energy matched for both MWD and analogue measurements. Such a correction could not be implemented for other segments as there was no analogue channel available.

calculated for each combination of segments.

The resulting fractional crosstalk values are shown in *Figure 6.9*, the segments are again arranged according to ring number. There are several noteworthy features in this data:

- Due to the small segment volume, and hence capacitance, in ring two, there is significantly reduced crosstalk from other rings. This is shown in the broad vertical band on the figure.
- Diagonal lines show the reduced effective crosstalk between segments in the same sector due to mutual exchange of charge. These lines are most pronounced in the two lines either side of the central diagonal, these represent nearest vertical neighbours. Either side of these lines are less pronounced lines indicating the next to nearest vertical neighbours.

- Higher than expected crosstalk is seen in segments R1-3, R3-3 and R5-1 (C1,C3 and A5 by AGATA labelling). The gain matching and later analysis for these segments was reviewed but the effect remained, suggesting this is a real phenomena. The likely cause is additional crosstalk due to the particular electronic wiring within the cryostat.

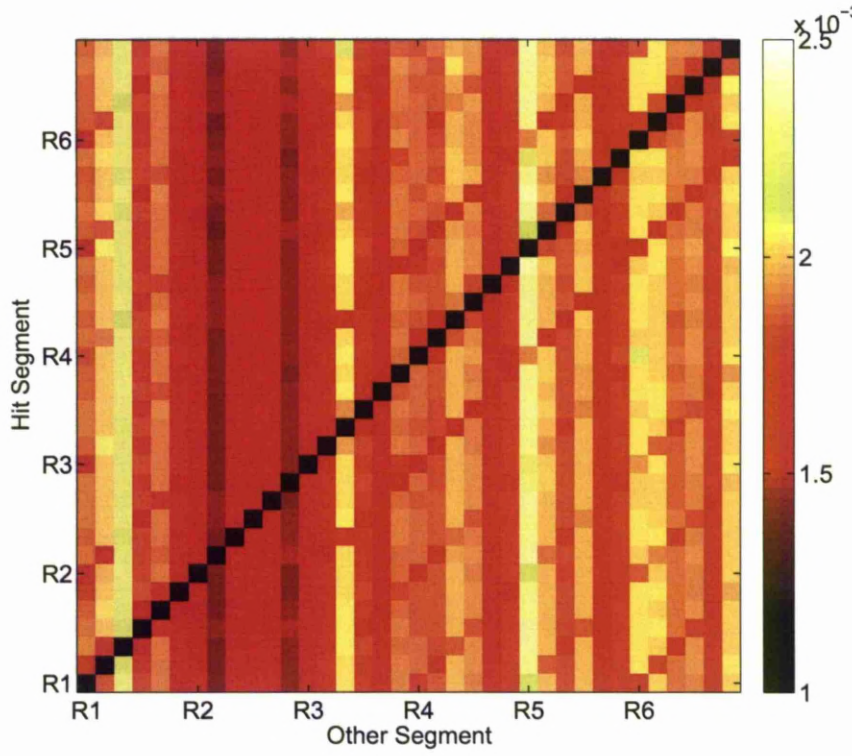

Figure 6.9: A plot showing the fraction of proportional crosstalk observed between pairs of segments using the baseline offset method. The segments have been numbered by ring rather than sector to highlight features. The smallest fraction is seen in ring 2, which has the smallest segment size and hence smallest capacitive coupling with the core. The diagonal lines show the mutual crosstalk between nearest neighbour segments.

Figure 6.10 shows a matrix with the mean crosstalk for each segment pair, as calculated by this method. The pattern seen here is what would be expected from the energy add back method if it were not for the problems with the MWD energy values.

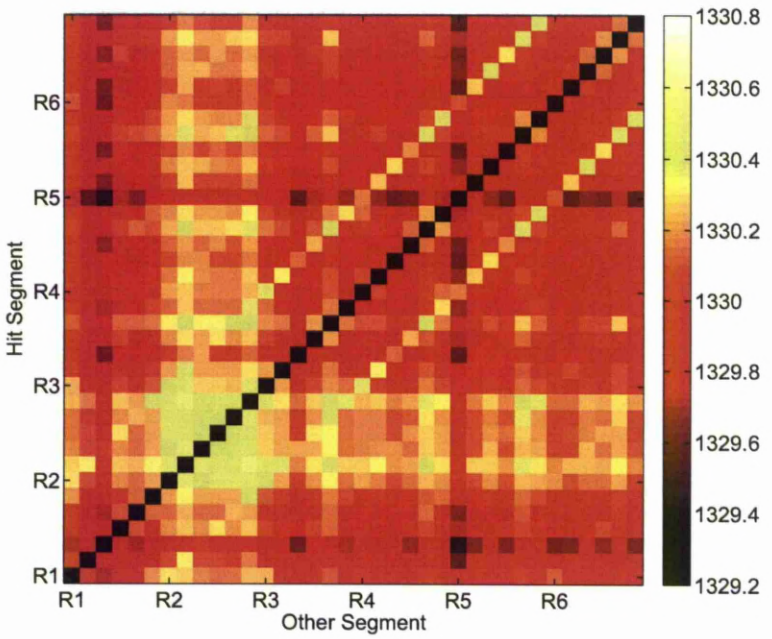

Figure 6.10: A plot showing the mean crosstalk for each segment pair, calculated using the baseline offset method. The segments are numbered by ring. The results of the energy add-back method should have produced a matrix like this if it were not for the problems with the MWD energy values.

6.5 Proportional Crosstalk Correction

Once the proportional crosstalk parameters are known, it is possible to invert the crosstalk model to reproduce the true deposited energies. The crosstalk in the system can be represented by a matrix, **B** such that:

$$\vec{E}_{meas} = \mathbf{B} \cdot \vec{E}_{true}. \tag{6.1}$$

The vectors, E, have n elements, where n is the segment fold for the event. Similarly, the matrix **B** is a square matrix, $n \times n$. We will consider here an event with $n = 3$ (segments 1,2 and 3 hit), but the method can be extended to any number of hit segments. If a detector was perfectly gain matched and had no crosstalk, the matrix **B** would be equal to the identity matrix:

$$\mathbf{B}_{ideal} = \begin{pmatrix} 1 & 0 & 0 \\ 0 & 1 & 0 \\ 0 & 0 & 1 \end{pmatrix}. \tag{6.2}$$

However, if we consider the fractional crosstalk $\delta_{i,j}$ between segments i and j, *Equation 6.2* becomes:

$$\mathbf{B} = \begin{pmatrix} 1 & \delta_{1,2} & \delta_{1,3} \\ \delta_{2,1} & 1 & \delta_{2,3} \\ \delta_{3,1} & \delta_{3,2} & 1 \end{pmatrix}. \tag{6.3}$$

We can then take the inverse of $\mathbf{B}$ and rewrite *Equation 6.1* as,

$$\vec{E}_{true} = \mathbf{B}^{-1} \cdot \vec{E}_{meas}. \tag{6.4}$$

This matrix multiplication can then be carried out for all events to reproduce the correct segment energies. This correction has been implemented on both the energy values and digitised signal traces presented in this thesis.

6.6 Full Electronics Calibration - Residual Minimisation Method

A method has been developed for the GRETINA collaboration [Rad10] to calibrate a complete response function for all components of a detector's electronics. From a combination of experimental and simulated data, parameters are calculated to account for proportional and differential crosstalk, preamplifier bandwidth, and delay for all channels. An outline of the process is shown in *Figure 6.11*.

6.6.1 Simulated Response

GEANT4 is a Monte-Carlo radiation transport simulation developed for high-energy physics applications at CERN. The AGATA GEANT simulation package [FRB+10] was developed in the AGATA collaboration to provide a simple method of constructing GEANT simulations of the AGATA array and associated ancillary detectors. The package allows the simulation geometry to be defined quickly by editing simple macro files which determine the number and placement of detector crystals and sources.

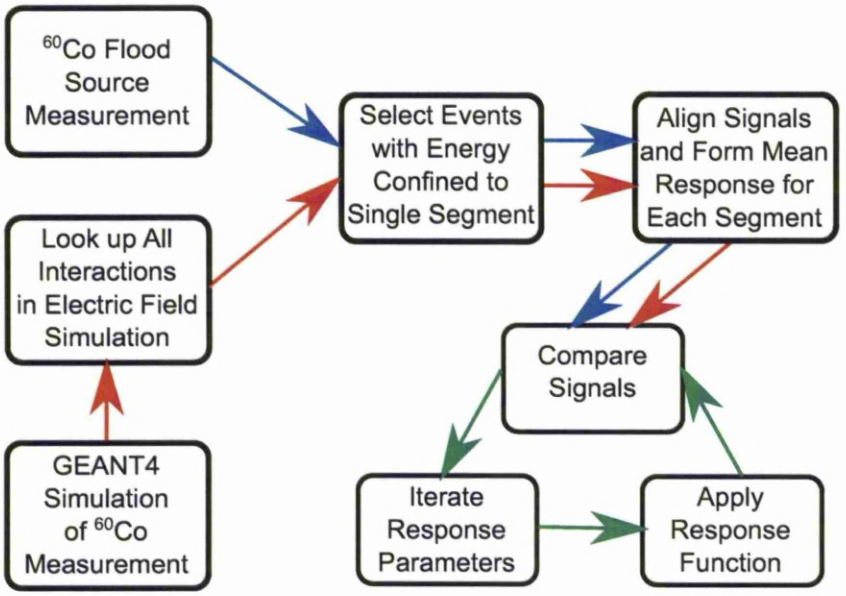

Figure 6.11: The process for performing a full electronics calibration by minimising the residual signal. Experimental data are collected using a digital acquisition system, with a ^{60}Co source placed 25cm from the detector front face. The same source and detector arrangement are modelled using GEANT4, and the signals from the gamma-ray interactions are reconstructed from an electric field simulation. The events, from both datasets, for which all of the deposited energy is confined to a single segment are then identified and organised according to segment number. The signals from each segment are aligned and a mean response formed for each. A fitting algorithm [Rad10] is then used to find the parameters for an electronic response function that minimises the difference between the experimental and simulated data.

For this work, a simple geometry was defined containing only a single C-type AGATA crystal, its aluminium encapsulation and aluminium cryostat end-cap. A 1332.5 keV gamma-ray source was placed 25 cm from the detector front face on the z axis, which ran parallel the crystals central contact. Before the simulation was used for the electronics calibration, the energy and position of interactions was investigated to ensure sensible results were obtained. A full simulation validation was not completed in this work, but the simulation package has been extensively investigated by other members of the collaboration.

Figure 6.12 shows spectra of the total energy deposited in the crystal by each gamma ray (top) and of all individual interactions (bottom). There was no randomisation of the

energy implemented, so the photopeak in the top spectrum has effectively zero width. The cross-section for pair production is very low at this energy but single and double escape peaks are visible at 821.5 keV and 310.5 keV due to the perfect energy resolution.

The energy of both primary and secondary interactions was tracked down to 1 eV; this results in the germanium K-shell X-ray peaks at 8 and 11 keV in the single interaction spectrum. Lower energy X-rays from other atomic shells are all in the first bin of the spectrum due to the 1 keV bin size. As expected, the number of single interactions falls off exponentially with increasing energy, approaching zero at around 550 keV.

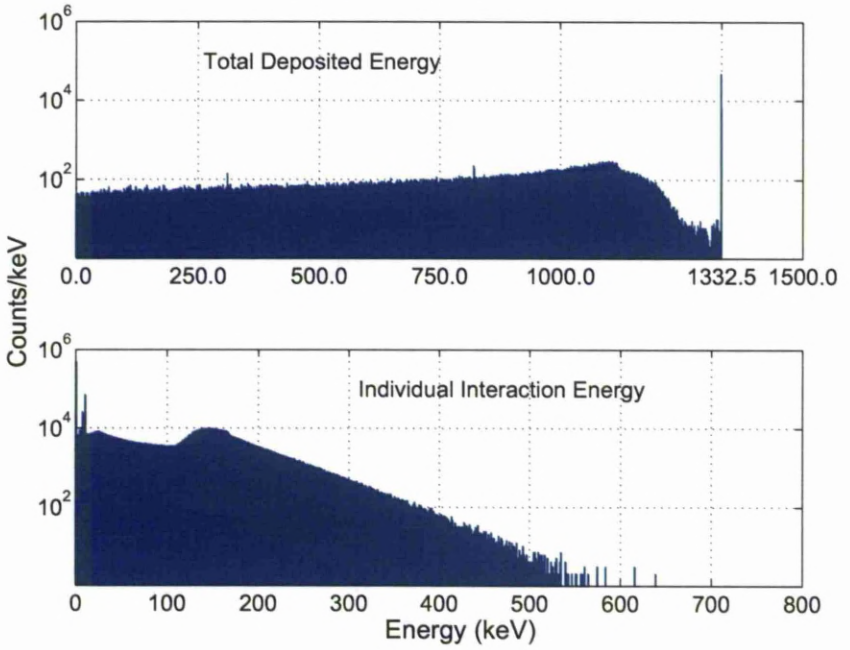

Figure 6.12: Energy spectrum from the AGATA GEANT4 simulation for 1332.5 keV gamma rays. The top spectrum shows the total energy deposited in the crystal. Perfect energy resolution is assumed in the simulation, resulting in visible escape peaks at 821.5 keV and 310.5 keV, features that would usually be difficult to resolve at this gamma-ray energy. The bottom spectrum shows the energy of individual interactions. Peaks for germanium K-shell X-rays are visible at 8 and 11 keV. The number of interactions falls exponentially with increasing energy, approaching zero at around 550 keV.

Figure 6.13 shows the position of the first interaction for the first 10000 events processed, in 3 dimensions (centre) and projected onto each 2 dimensional plane. The profile of the

interactions can be seen to match the AGATA crystal shape, including the hexagonal taper and the empty region inside the central contact. *Figure 6.14* shows histograms of the x,y and z coordinates of the same 10000 interactions. The attenuation of gamma rays through the depth of the detector is apparent, confirming correct source positioning in the simulation. At the extremes of the detectors radius, the distribution of y coordinates falls off more sharply than the x coordinates. This is due to the x axis running through segment corners while the y axis runs through segment faces.

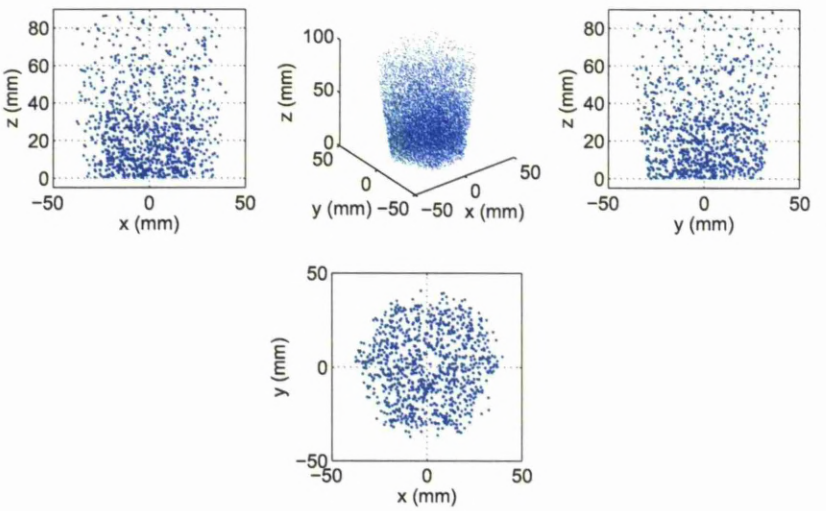

Figure 6.13: The positions of the first interaction for the first 10000 events from the GEANT4 simulation. The shape of the AGATA crystal can be seen including the hexagonal taper and the empty region inside the central contact. The attenuation of gamma rays through the depth of the crystal is also apparent.

In order to compare the gamma-ray attenuation to the known behaviour of 1332.5 keV gamma rays in germanium, a histogram of the total distance from the source to the first interaction was constructed. This is shown in *Figure 6.15*.

The number of interactions is zero until the minimum distance from the source to the detector front face is reached at 250mm. The rate then rises quickly as all gamma rays with a trajectory directed toward the detector reach it within 253mm. The number of interactions then falls of exponentially until it drops to zero at the back of the detector.

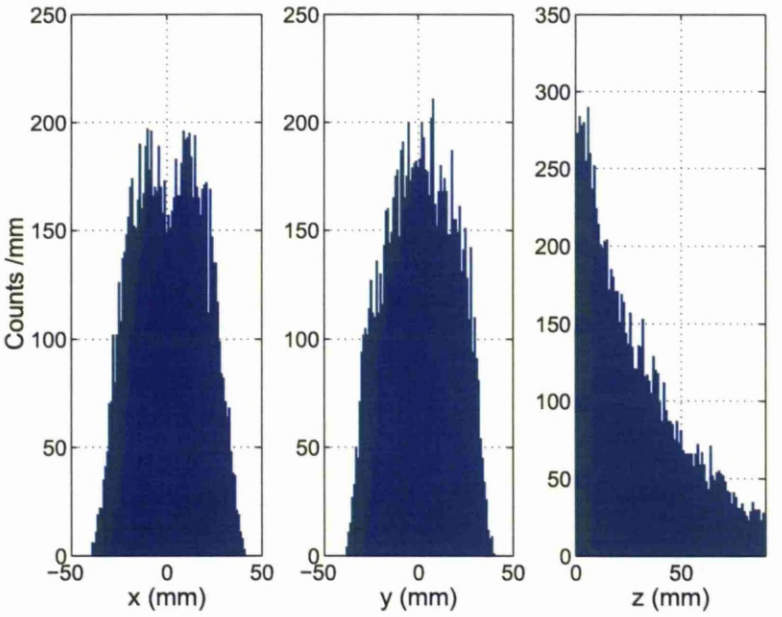

Figure 6.14: The distribution of x,y and z coordinates of the first interaction for the first 10000 events generated by the AGATA GEANT4 simulation. The attenuation of photons through the depth of the detector is apparent, confirming correct source positioning in the simulation.

The expected rate, given the linear attenuation coefficient of 0.2628cm^{-1}, is shown in red and is consistent with the simulated results.

Once the correct configuration of the simulation had been confirmed, a total of 10^{10} gamma rays were simulated to ensure sufficient numbers of events for the analysis. Once the simulation was complete, the following steps were taken to process the raw GEANT4 output:

- The raw output produced by the simulation was in ASCII format, with all interactions listed for every simulated event. The total deposited energy was summed for all events and those with less than the full energy of 1332.5 keV were discarded.

- Interactions that occurred within 1mm of one another were 'packed' together and replaced with an interaction at their energy-weighted mean position. This reduced significantly the number of interactions, as almost all of the low energy X-rays deposited their energy within this distance of their source atom. At this stage a new

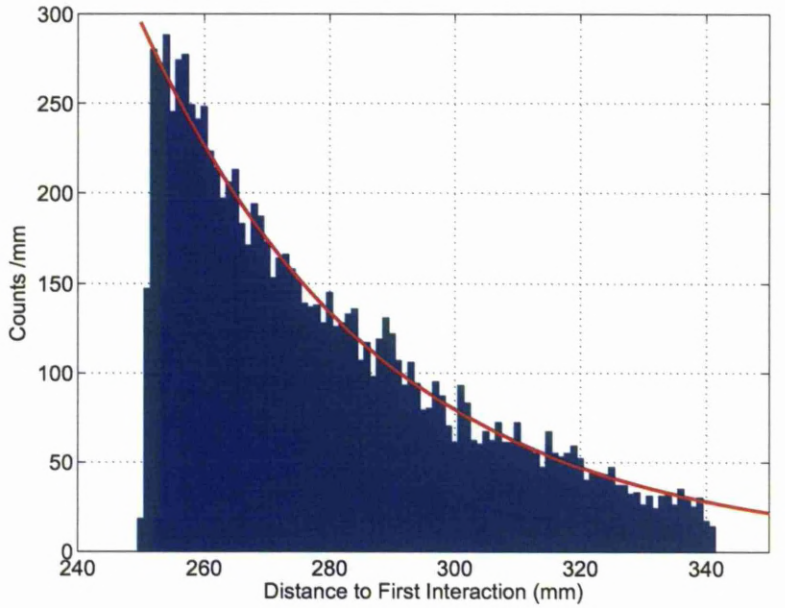

Figure 6.15: The distance from the source to the first interaction for the first 10000 simulated events. The red line shows the expected distribution according to the linear attenuation coefficient for 1332.5 keV gamma rays moving through germanium.

data set was created containing only the packed photopeak interactions. This greatly increased the speed of later processing as, when processing the raw data, the majority of sort time was taken up with disk access.

- The coordinates of each remaining interaction were looked up in the JASS electric field simulation. Those events which were found to share their energy across more than one segment were discarded.

- The simulated signals were normalised so that the real charge signal had a maximum of 10000 in order to match the expected format of the fitting algorithm used later. The signals were also re-sampled at 10ns intervals to match the experimental data. The preamplifier correction, described in *Section 3.5*, was not applied to the simulated signals in this instance, as a preamplifier response is included in the full electronics response function.

- An energy weighted mean was then formed of all the interactions in the single segment

events. No alignment was needed at this stage, as the simulated signals all began from their true t0. At this stage, the signals from each event should represent a typical signal seen in experimental data when energy was confined to a single segment.

- 36 separate files were created, one for each hit segment. Each one contained the simulated signals, for all 37 detector channels, for each event confined to that particular hit segment.

- A mean response of all events for each particular segment was then formed. It was essential at this stage to perform the alignment in the same way as was done with the experimental data. The real charges were aligned to t10, a shift of equal magnitude and direction to the hit segment was applied to all non hit segments.

- The resulting 36 sets of 37 mean signals were stored for later comparison with the experimental data.

The resulting mean simulated response signals for events in segment A2 can be seen in *Figure 6.16.* The image charge signals are smaller than those typical of a single event, this is the result of forming an average from both positive and negative signals. As there are more interactions near the outside of the crystal, where the image charges are negative, the net image charges for the mean response are negative.

6.6.2 Experimental Response

The same experimental data used for the crosstalk calibrations, discussed earlier, were used for this method. The data were processed in the following way:

- All energies and traces were gain matched.

- A MWD energy gate was placed on the 1332.5 keV photopeak.

- The segment fold was identified using the same 3 sigma threshold discussed for earlier measurements. Events with energy found in more than one segment were discarded.

- All events passing these gates were sorted according to the hit segment into 36 separate files containing only the 37 signal traces for each event.

- The signals were normalised to a real charge height of 10000.
- A mean response was formed for each hit segment by aligning the real charge to t10 and shifting other segments by the same amount.
- The resulting 36 sets of 37 mean signals were stored for later comparison with the simulated data.

The resulting experimental signals for interactions in segment A2 can be seen in *Figure 6.16*. Similarly to the simulated signals, the image charges are negative, and smaller than for a typical single event.

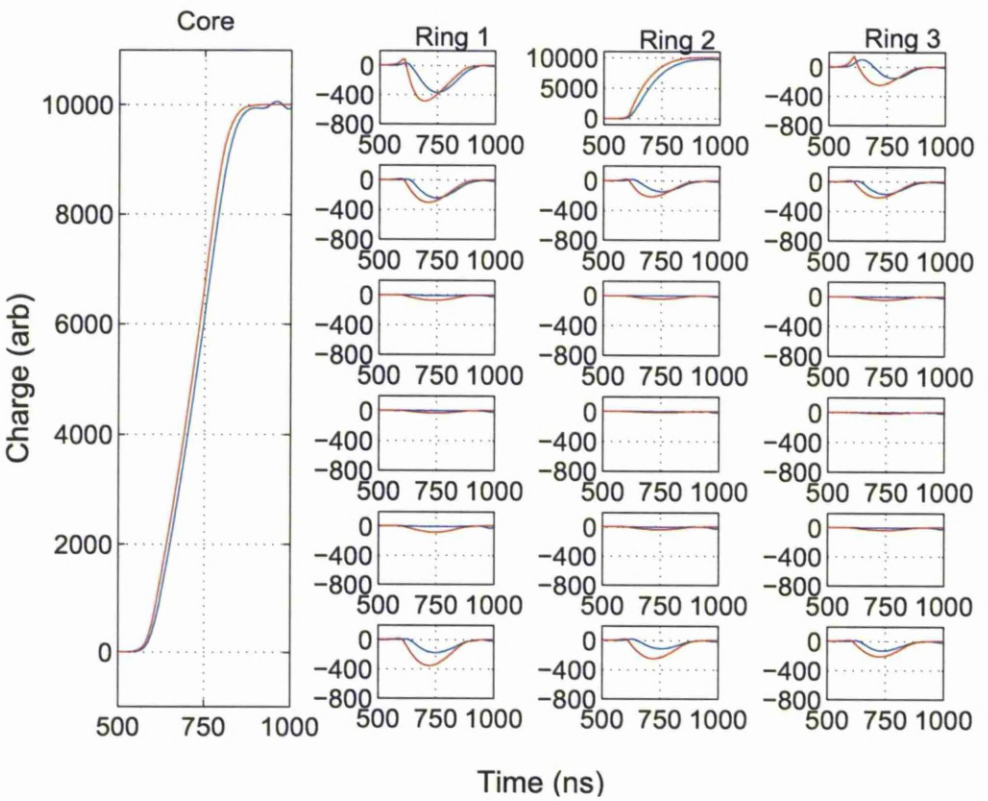

Figure 6.16: The experimental (blue) and simulated (red) mean segment response for events confined to segment A2.

6.6.3 Fitting

Once the simulated and experimental signals for all 36 segments had been obtained the next stage was to find the response function parameters that minimise the difference between the two. In order to achieve this, a computer code developed by David Radford [Radford2009a] for the GRETA collaboration was used to model the response function and perform the fit. Four effects are included in the response function used, they are applied to the simulated signals in this sequence:

- **Preamplifier Shaping** An integration was applied to the data using the time constant τ. The first sample of the output pulse was set to zero, $SigOut(0) = 0$. The remaining samples were calculated according to,

$$SigOut(n+1) = SigOut(n) + \frac{SigIn(n) - SigOut(n)}{\tau}. \tag{6.5}$$

- **Proportional Crosstalk** A correction was applied for proportional crosstalk to every sample of each trace. The magnitude of the correction was equal to the charge on the source signal at each sample, times the crosstalk coefficient between the channels being considered.

$$SigOut1(n) = SigIn1(n) + \delta_{2,1}\, SigIn2(n) \tag{6.6}$$

- **Differential Crosstalk** For each channel being considered, a numeric differential was calculated using a single sample step size. A proportion of this differential signal was then added to the signal for each other channel, according to the magnitude of the differential crosstalk coefficient, ϵ. The correction was not necessarily made to the same sample in each trace however, a second delay parameter, x, was used here to allow for a time shift between the signals,

$$SigOut1(n) = SigIn1(n) + \epsilon_{2,1}\frac{d\, SigIn2(n+x)}{dt}. \tag{6.7}$$

- **Delay** A delay was introduced to each signal to account for any differences in the length of cabling between the different channels.

In order to find the best parameters to use when applying these effects to the signals, the code used the *Marquardt Method* of gradient searching described in [BR92].

6.6.4 Results

The fitting algorithm had the facility to fix any combination of the parameters at null values. This allowed the parameter space to be reduced by ignoring, for example, crosstalk between segments that were separated by more than one segment. Several different combinations of parameters were used and the results studied to assess the reliability of the resulting response function.

A parameter set that produced entirely realistic values was not found. In particular, it was found that the algorithm was finding negative preamplifier shaping times and proportional crosstalk coefficients that did not match the values obtained and tested using the baseline offset method. Ultimately this method of finding the response function was abandoned due to a lack of time to pursue it further.

Two possible reasons for the failure of the residual minimisation method were identified:

- The JASS signal basis was found to produce unrealistic signal shapes in some regions of the detector. In particular, the rise time of some of the signals was much faster than those seen in experiment (see *Chapter 7*). This may explain why the algorithm was finding negative shaping times for some of the preamplifier channels.
- The experimental data was found to have smaller than expected image charge magnitudes for many of the interaction positions studied with the coincidence scan.

Given the above issues with the simulated and experimental data, it is unrealistic to expect an accurate response function to be derived from the experimental and simulated data. This method has however, been demonstrated to work for the GRETINA quad detectors in the USA, and as such it is recommended that this approach is tried again with new AGATA data once the simulated basis has been improved.

Chapter 7

Evaluation of Experimental and Simulated Data

In order to asses the degree of agreement between the experimental and simulated data, pulse shape analysis has been applied to the coincidence scan mean signals using both JASS and MGS bases. In this chapter, the pulse shape analysis method will be described, the results will be presented, and some examples of the simulated and experimental pulse shapes will be examined.

7.1 Pulse Shape Analysis Algorithm

For the purposes of this analysis, a comprehensive basis search algorithm was employed. Each of the mean signals produced using the method described in *Chapter 5* was taken in turn and compared with every signal from the signal basis for which the charge was collected in the same hit segment. The RMS difference between each basis signal and the experimental mean was calculated for the hit segment, core, and each of the four immediate neighbours (refereed to here as *Up*, *Down*, *Left*, and *Right*). For rings 1 and 6, only three neighbour segments were used. The range of samples used in the difference calculation was set independently for each of the experimental mean signals. The first sample was set as either the core or hit segment t10, whichever was earlier, and the final sample was the core or hit segment t90, whichever was later. The alignment between the two signals was kept as a free parameter and the minimum difference recorded. Equal weighting was given to

each of the six channels considered and the basis position with the smallest total difference was recorded as the calculated position.

This process was repeated with both the MGS and JASS bases. For each basis the crystal axis alignment was chosen to match that calculated from the singles scan data in *Section 4.5.3*. For the MGS basis, the impurity concentration used was that specified by the crystal manufacturer: $1.4\times10^{10}\text{cm}^{-3}$ at the back of the crystal $0.65\times10^{10}\text{cm}^{-3}$ at the front face. The hole and electron mobility parameters were fixed to those given in [MGL+00] and [RCNO77], detailed in *Table 3.1*.

For the JASS basis, the reduced impurity concentration of $1.2\times10^{10}\text{cm}^{-3}$ was used at the back of the crystal to allow for more complete depletion (see *Section 3.6*). The hole and electron mobility parameters were the same as those used for the MGS basis.

7.2 General PSA Results

In this section, the PSA results for all positions will be presented and trends identified. A more detailed investigation into the results from specific regions of the detector will be discussed in *Section 7.3*.

7.2.1 JASS Basis

Figure 7.1 (top) shows the results, in quiver plot format, of PSA applied to all coincidence scan mean signals using the JASS basis. The arrows on the quiver plots start at the experimentally determined position, and end at the position found by the PSA algorithm. Projections of the same data are shown onto the xy, xz, and yz planes. *Figure 7.1 (bottom)* shows histograms of the difference between experimental and PSA positions in each dimension. The mean offset in each dimension is indicated by the red dashed line. The quiver plot on the xy plane is difficult to read due to the overlap of events from the six different scan depths, *Figure 7.2* shows the same plot with the data split into six different depths.

Several features are evident from these figures:

- There is significant variation from point to point of the magnitude of the difference between the experimental and PSA positions. This implies the position resolution that can be achieved will vary through the detector. This is not unexpected as the

rate of change of the signal shape with position is not uniform. This effect can also be seen in the singles scan data presented in *Section 4.5.*

- The quiver plots in the xz and yz planes reveal a range offsets in both positive and negative z direction. There is an overall trend for PSA to find the interaction further back in the crystal than experiment. This trend in the z direction is visible in the histogram of z offsets (*Figure 7.1 bottom right).* However this trend is not uniform as many interactions, particularly in rings one and six, are shifted in the opposite direction. The PSA results in ring 1 seem to diverge in both directions from the experimental z position, with some events found a few mm back into the detector and others found directly on the detectors front face at z = 1mm.

- The histogram of z values shows sudden drops in intensity in alternate bins. This is the result of the 1mm granularity of the signal basis. The experimental z positions are represented by six real numbers, then mapped by PSA onto a range of 90 integers. This results in a higher probability of observing some magnitudes of offset in the z direction than others. This effect is not seen in x and y due to the rotational transformation used to move between the scan and AGATA coordinate systems (*Figure 4.6*), which maps the experimental x and y coordinates onto a range of non-integer values but leaves z unchanged.

- On average there are larger z offsets at small radius than large.

- At large radii, there is a tendency for PSA to find a position at smaller radius. This is particularly evident towards the back of the detector where it seems to be the result of faster rise times observed in the JASS basis than in experiment. The effect will be discussed in more detail in *Section 7.3.*

- It appears that the radial position of an interaction is generally determined with greater precision than the azimuthal position. For a large fraction of the positions there is a translation across the detector segment, perpendicular to the direction of charge collection. In most cases the PSA position is shifted toward the centre of the segment, in some cases however, the translation approaches the opposite side of the segment. The positions found by PSA seem to cluster towards a radial line, the position of which varies for each segment but is usually close to the segment centre.

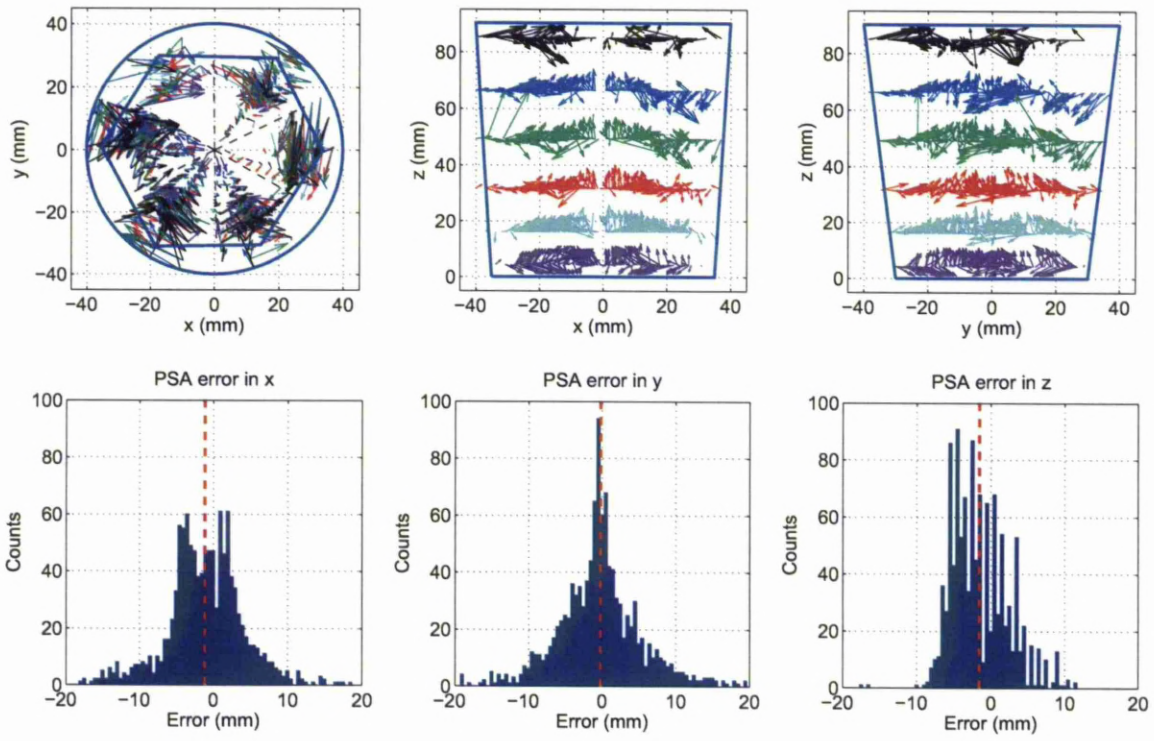

Figure 7.1: Quiver plots resulting from PSA performed on all of the coincidence scan mean signals, using the JASS basis (top). The arrows start from the position determined by the primary and secondary collimator positions and end at the best matching position in the signal basis. Projections are shown into the xy (left), xz (centre), and yz (right) planes. Histograms of the difference between the experimentally determined position and that found by the JASS basis search (bottom), in the x (left), y (centre), and z (right) directions. The mean offset is shown by the red dashed line.

7.2.2 MGS Basis

Figure 7.3 and *Figure 7.4* show the same plots as discussed in the previous section, but this time generated using the MGS signal basis. The general trends apparent in the images are broadly similar to those seen when using the JASS basis, however there are some noteworthy differences:

- In ring one of the detector, the PSA results are similar to those produced by JASS in

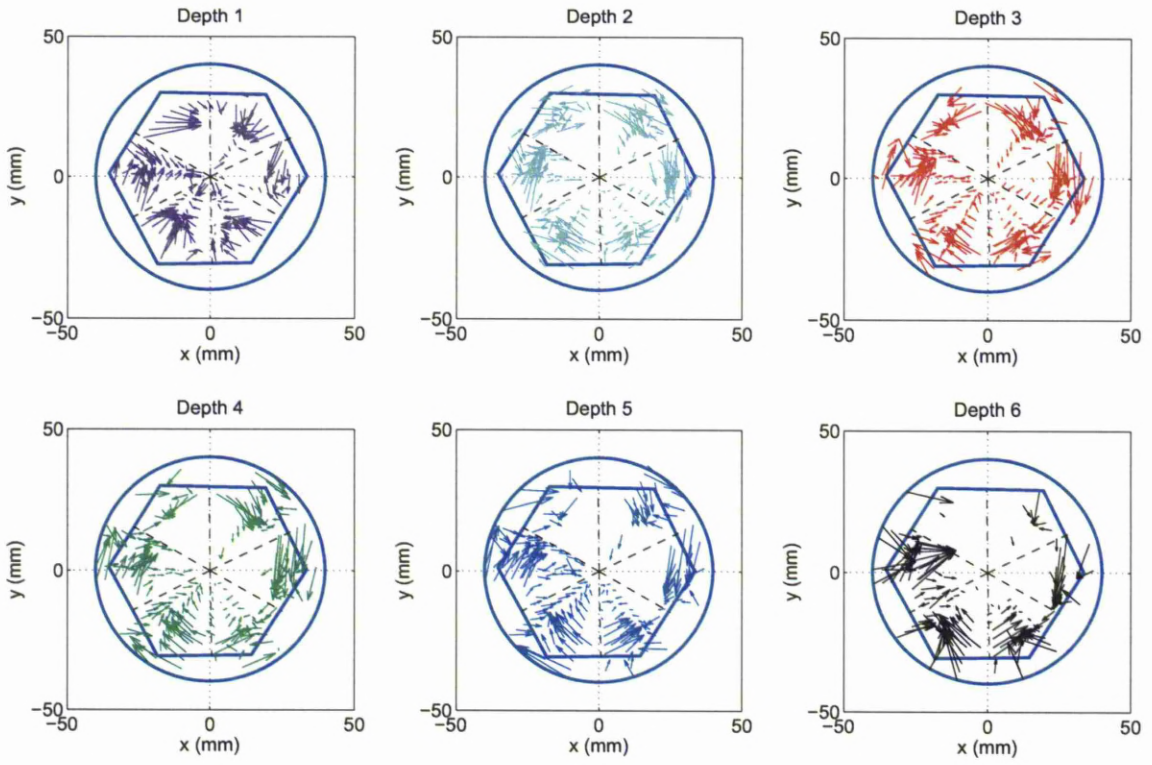

Figure 7.2: Quiver plots showing the difference between the interaction position determined by the primary and secondary collimator positions, and the best matching signal from the JASS basis. The six plots show each of the secondary collimator depths. There is a general trend for the basis search to find a position further from the sector boundary than the collimator position would suggest.

that the reconstructed positions are divided between those shifted back in the detector, and those shifted toward the front face. In the case of the MGS basis however the points are found just short of the front face at z = 2mm. This seems to be simply the result of the missing MGS basis points near the outside of the detector, as discussed in *Section 3.6.2.*

- The trend for PSA to find interactions in ring 6 to be further from the back of the detector than was experimentally determined is still present. This trend seems to be stronger in the MGS data, particularly at small radii and can be related to the

differences in rise time distribution at the back of the detector. *Figure 3.14* shows the T90 distribution for both bases at z = 80mm and while the systematics are similar for both distributions, the actual magnitude is significantly different. The MGS T90 varies between 100ns and 275ns, compared with 150ns to 350ns for the JASS basis. A direct comparison of these rise times with the singles scan data in *Figure 4.10* is not possible due to the effect on the mean rise time of multiple site interactions. The range of values observed however, suggest that the rise times calculated by JASS are, in this region, closer to those seen experimentally.

- As with the JASS basis, the PSA positions seem to cluster toward a radial line in each segment. The position of these lines is not the same as found that found with the JASS basis, this is likely due to the differing rise times seen in the two bases.

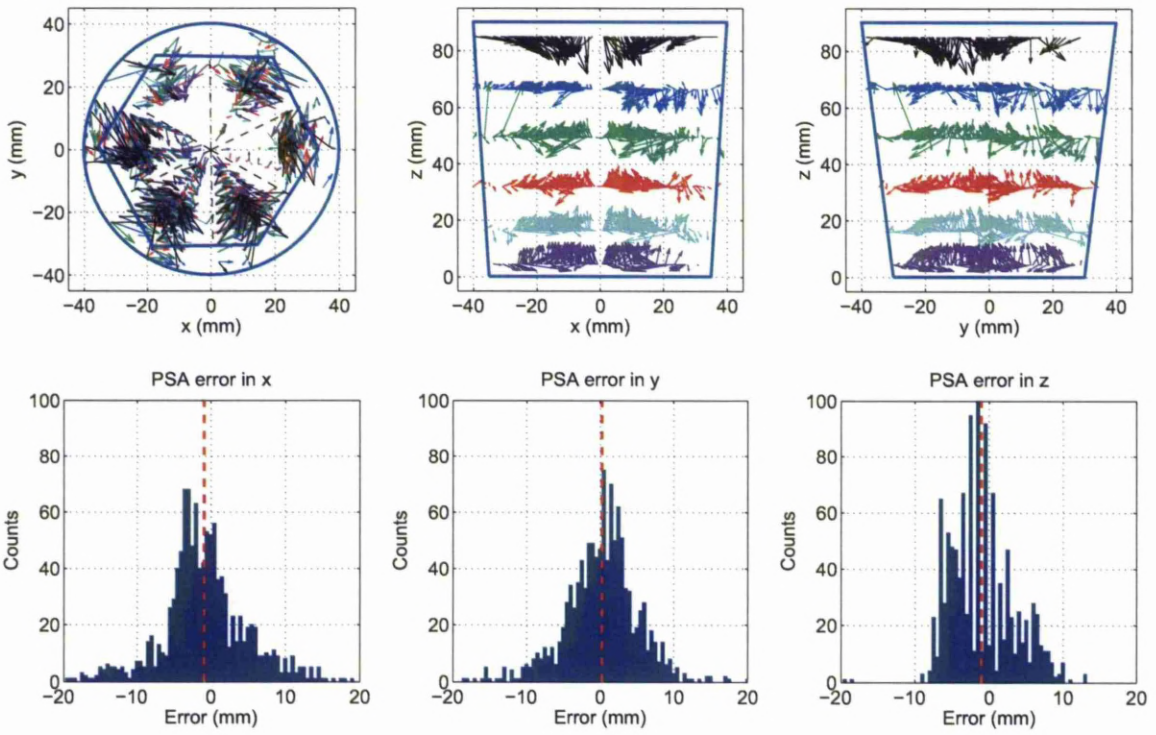

Figure 7.3: Quiver plots resulting from PSA performed on all of the coincidence scan mean signals, using the MGS basis (top). The arrows start from the position determined by the primary and secondary collimator positions and end at the best matching position in the signal basis. Projections are shown into the xy (left), xz (centre), and yz (right) planes. Histograms of the difference between the experimentally determined position and that found by the MGS basis search, in the x (left), y (centre), and z (right) directions. The mean position is shown by the red dashed line.

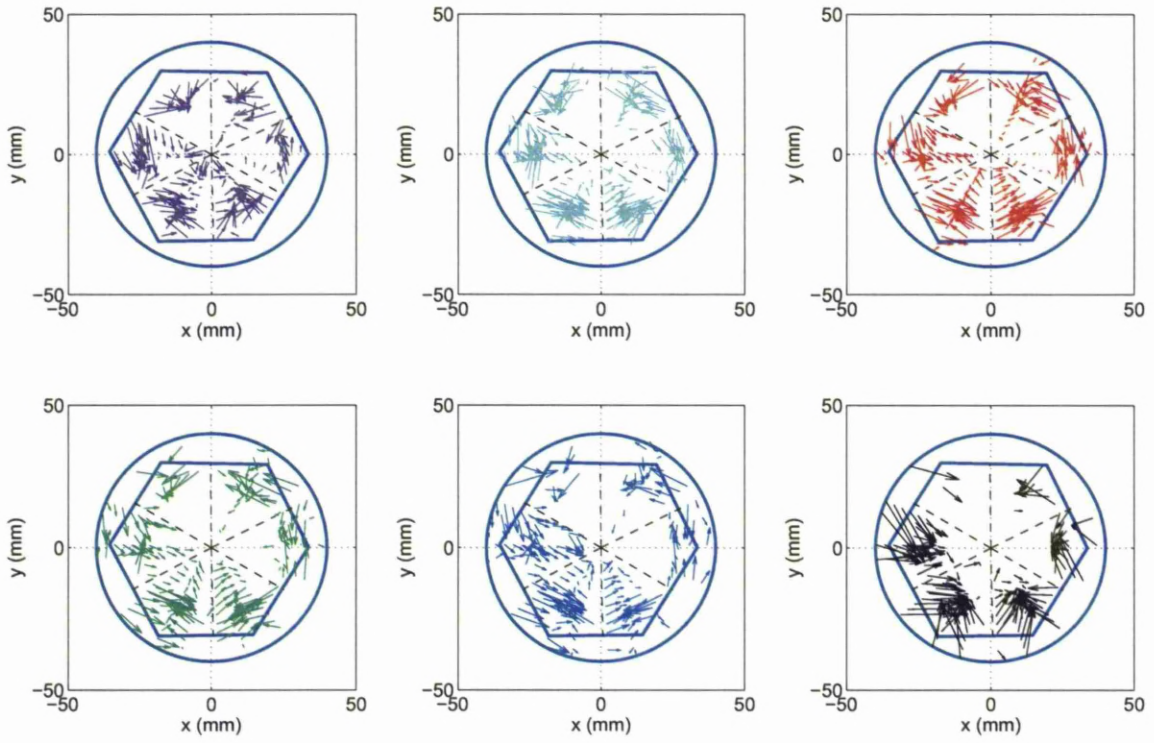

Figure 7.4: Quiver plots showing the difference between the interaction position determined by the primary and secondary collimator positions, and the best matching signal from the MGS basis. The six plots show each of the secondary collimator depths. There is a general trend for the basis search to find a position further from the sector boundary than the collimator position would suggest.

7.2.3 Systematic Offset

As discussed in *Section 5.1*, although the spacing between the secondary collimators was known with high precision, there was some degree of uncertainty as to the position of the collimator array relative to the detector crystal. This systematic error should be visible as a net offset in the z positions identified by PSA. *Figure 7.5* shows the mean offset, in each dimension, of all the positions found by PSA using each of the bases.

In both cases, the x and y offsets are relatively small, less than 3mm in ring six and less than 1mm in most of the detector. No strong conclusions can be drawn from these values however as, in the xy plane, differences are cancelled by the symmetry of the detector. In the z direction however, there is no cancellation and the mean offset reveals useful information. Interactions in the front and back rings are found to have a large offset away from the detector front and back faces respectively. As these offsets are in opposite directions it can be concluded that they are not due to the physical positioning of the detector, but due to the matching between simulated and experimental data. Unlike in the bulk detector volume, in these regions of the detector the electric field and charge collection trajectories are not parallel to the detector front face. This may result in an increased dependency of the determined z position on small differences in the rise time behaviour between simulation and experiment.

Examining the other rings however suggests that there is still a net offset of the PSA positions toward the back of the detector. As there is no other apparent explanation for this, it is proposed that this is due to a physical offset in the position of the crystal. The mean shift in rings 2-5 is 1.65mm using the JASS basis and 1.44mm using the MGS basis. Taking a mean of these values and rounding to the nearest 0.5mm produces an offset of 1.5mm, this will be applied to the experimental data when direct signal shape comparisons are made in the following section.

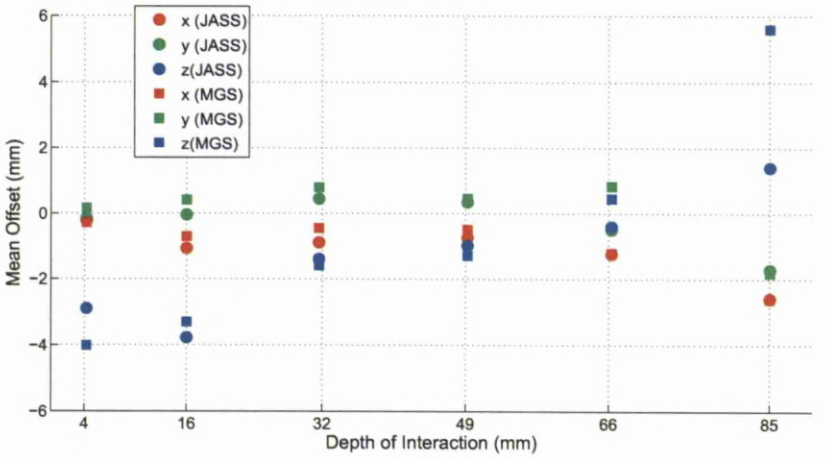

Figure 7.5: The mean offset between the experimentally determined and PSA interaction positions versus the secondary collimator position, for both JASS and MGS signal bases. The offset in the z position for the central region of the detector (rings 2-6) has been used to estimate the systematic error due to the positioning of the crystal on the scan table. The mean offset in the z direction in these rings is -1.65mm according to the JASS signal basis and -1.44mm according to the MGS basis. The offset in the x and y directions is exceptionally small here, this is due to the cancelling of positions on opposite sides of the detector.

7.3 Further Investigation of Signal Shapes

In order to highlight the differences and similarities between experimental and simulated signals, a more detailed comparison will be made at a selection of regions in the crystal; *Figure 7.6* shows the positions to be considered. For each set of positions, figures will be presented showing the signal shape as a function of position for selected detector segments which are generated from the experimental data and from both of the signal bases. Quiver plots are shown indicating the offset from the experimental position to the position found by PSA, for both signal bases. For selected positions, experimental and simulated signals will be aligned by minimising the RMS difference between them, then shown together alongside the residual difference between the two.

The simulated signals shown in this section are taken from the same position as the experimental signals, after the correction for the systematic offset found in *Section 7.2.3*.

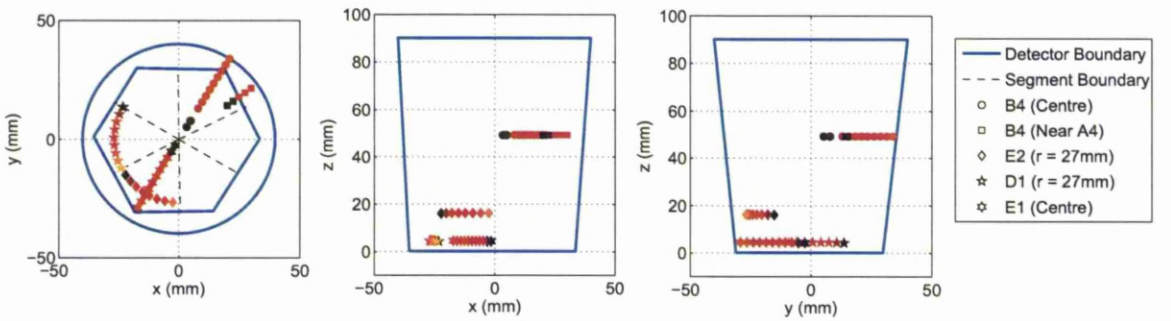

Figure 7.6: The positions of interactions to be considered in detail in this chapter. The points on the plot represent the position, in the AGATA coordinate frame, of the coincidence scan mean signals discussed in this section. Projections are shown into the xy (left), xz (centre) and yz (right) planes.

7.3.1 Line Through Centre of Segment E1

The signals here represent positions on a line through the centre of segment E1, 6mm from the detector front face. *Figure 7.7* shows the signals from experiment (left), JASS (centre) and MGS (right), produced by the core (top), hit segment (bottom), and up segment

(centre). The simulated signals are all aligned to their true t0 position but this is impossible to reproduce with the experimental signals due to electronic noise. The experimental signals have instead been aligned to t30.

At small radius, both the core and hit segment produce very fast signals (T90 $\approx$ 50ns) as the charge is collected over the short distance between the core and detector front face. The total rise time increases with radius as the charge collection distance grows. At larger radii, the fastest part of the hit segment signal is at the beginning because the charge is moving close to the segment contact, where its weighting field gradient is steepest. This situation is reversed for the core, which has it's steepest component at the end as the charge approaches its contact. The magnitude of the image charge seen in the up segment increases with increasing radius, as the charge collection path passes closer to that contact. Both simulations see only negative image charges in the up segment at these positions, the experimental data however suggests that at small radii, there is a small positive image charge.

The signals from the JASS basis show that at larger radii there is a sudden increase in the rise time for the last $\approx$70% of the core signal. In fact, before the preamplifier correction is applied to the JASS signals, the last section of the charge pulse rises within a single 1ns sample for some positions. This discontinuity in the core signal seems unphysical and clearly does not match what is seen in experiment, a similar effect is seen in the JASS basis at a number of positions. The regions affected by this rise time discontinuity can be seen in the rise time slice at z=5mm in *Figure 3.14*.

Figure 7.8 shows the quiver plots for the points on this line produced with JASS (left) and MGS (right). The offset in the azimuthal direction is small for all of these positions using either basis. The MGS basis also produces accurate positions in the radial direction. In the case of the JASS basis, the radial position is accurately determined at small radii but closer to the outside of the detector there is a large offset to positions at smaller radius because of the discontinuity in the core rise time. The faster than expected rise causes the PSA algorithm to find a better match at smaller radius than the true position.

To illustrate the differences more clearly it is useful to show experimental and simulated signals on the same axis. *Figure 7.9* and *Figure 7.10* show the experimental (blue) and JASS (red) signals for the two extreme positions in this line. The signals for each segment have

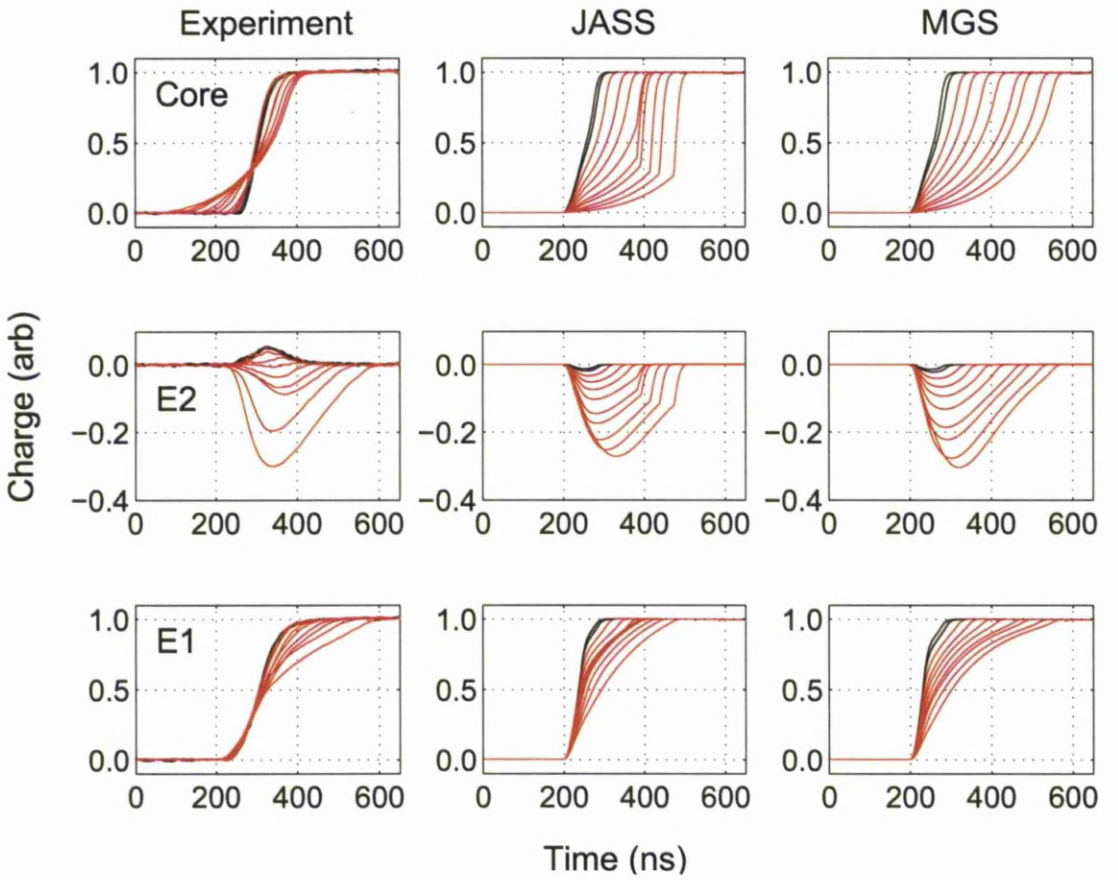

Figure 7.7: Signals from the core (top), hit segment (bottom), and segment above (centre) for interactions on a line through the centre of segment E1 at z = 6mm. Signals determined by experiment (left) are shown, along with those from the JASS (centre) and MGS (right) electric field simulations.

first been aligned by minimising the RMS difference between them, the residual difference has then been calculated by subtracting the simulated signal from the experimental signal. The residual, shown in black on the figures, has been offset by 0.3 for clarity. Plots showing the experimental and MGS signals for the same positions can be found in *Appendix A*.

Figure 7.9 shows the signals from the smallest radius position, shown in black on *Figure 7.7*. *Figure 7.10* shows the signal from the maximum radius, orange on *Figure 7.7*. At small radius, the opposing image charge polarity of the signals produces a large residual in each of the neighbour segments. Examination of the up image charge signals shows that, in this

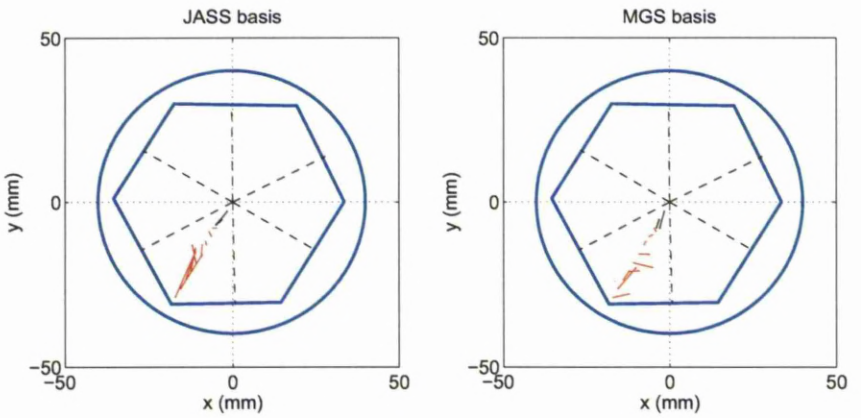

Figure 7.8: Quiver plots showing the positions determined by PSA for the experimental signals shown in *Figure 7.7*, using the JASS (left) and MGS (right) signal bases. Using the JASS basis results in generally good position determination at positions close to the detector core, but closer to the outside of the detector there is a trend of finding interactions closer to the centre. This seems to be due to the rise time predicted by JASS at these radii being smaller than that which is observed. MGS produces good matching for all of these positions.

region of the detector, the magnitude is changing quickly with changing xy position. This difference in polarity could be the result of a small offset in the positioning of the crystal, or possibly the result of differential crosstalk.

At small radius, the core signal calculated by JASS matches closely to experiment however the segment signal rise time is significantly faster. This can be seen clearly in the hit segment residual and image charge widths in *Figure 7.9*. Conversely, at larger radii the JASS segment signals match very closely, the small differences in image charge magnitude seen in *Figure 7.10* could easily be explained by differential crosstalk. In contrast to this, the core signal is much faster in JASS than experiment and leaves a very large residual as a result of the discontinuity discussed earlier. This phenomena of fast segment signals at small radius and fast core signals at large radius is seen throughout the JASS basis.

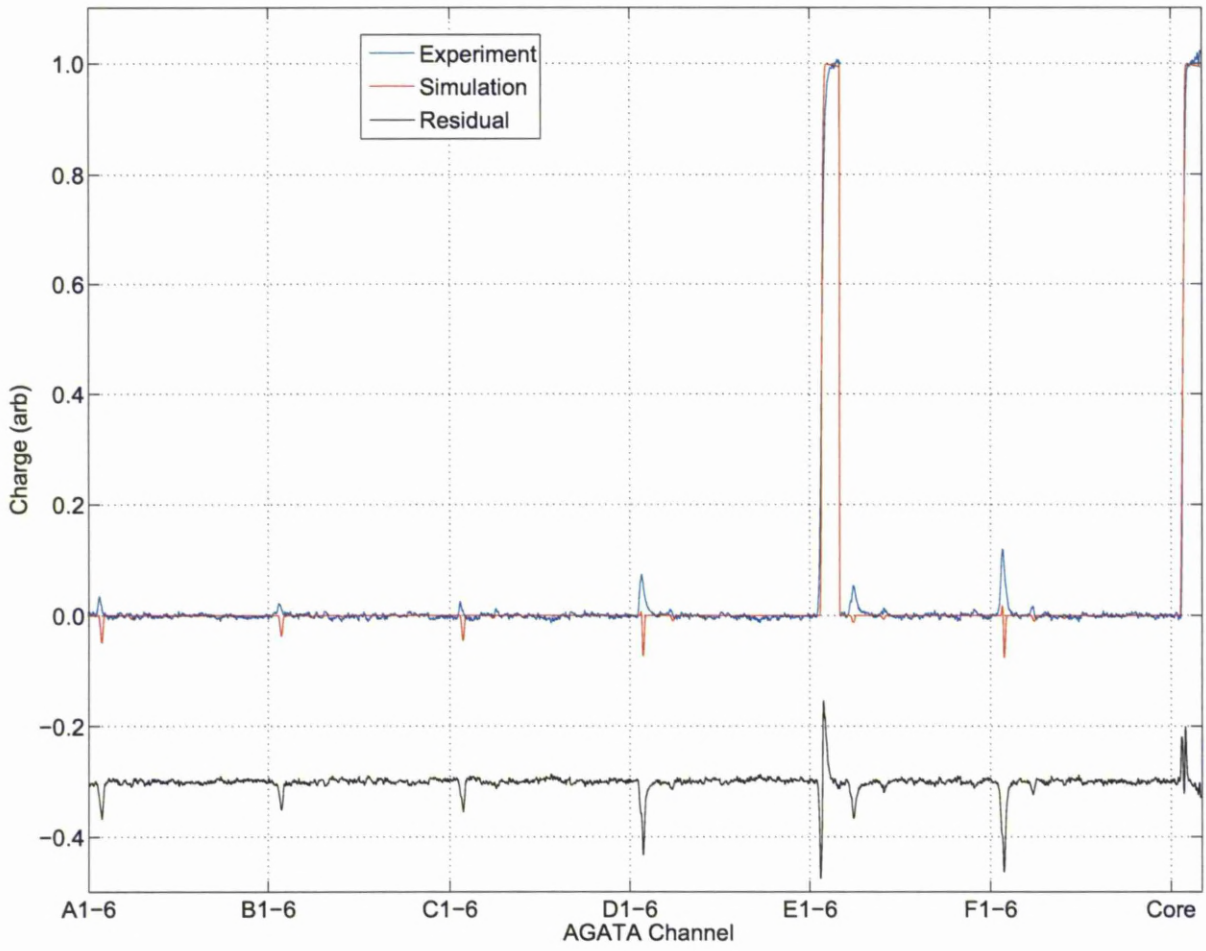

Figure 7.9: The experimental (blue) and JASS (red) signals for all detector segments, for interactions at the position from *Figure 7.7*, closest to the central contact. The signals have been aligned using a difference minimisation method, the residual difference is shown in black with a negative offset of 0.3 for clarity. There is a large residual on the core signal, first negative then positive, due to the faster rise time seen in the simulation. There is also a large residual in the image charge segments due to opposing polarity between the experimental and simulated image charges.

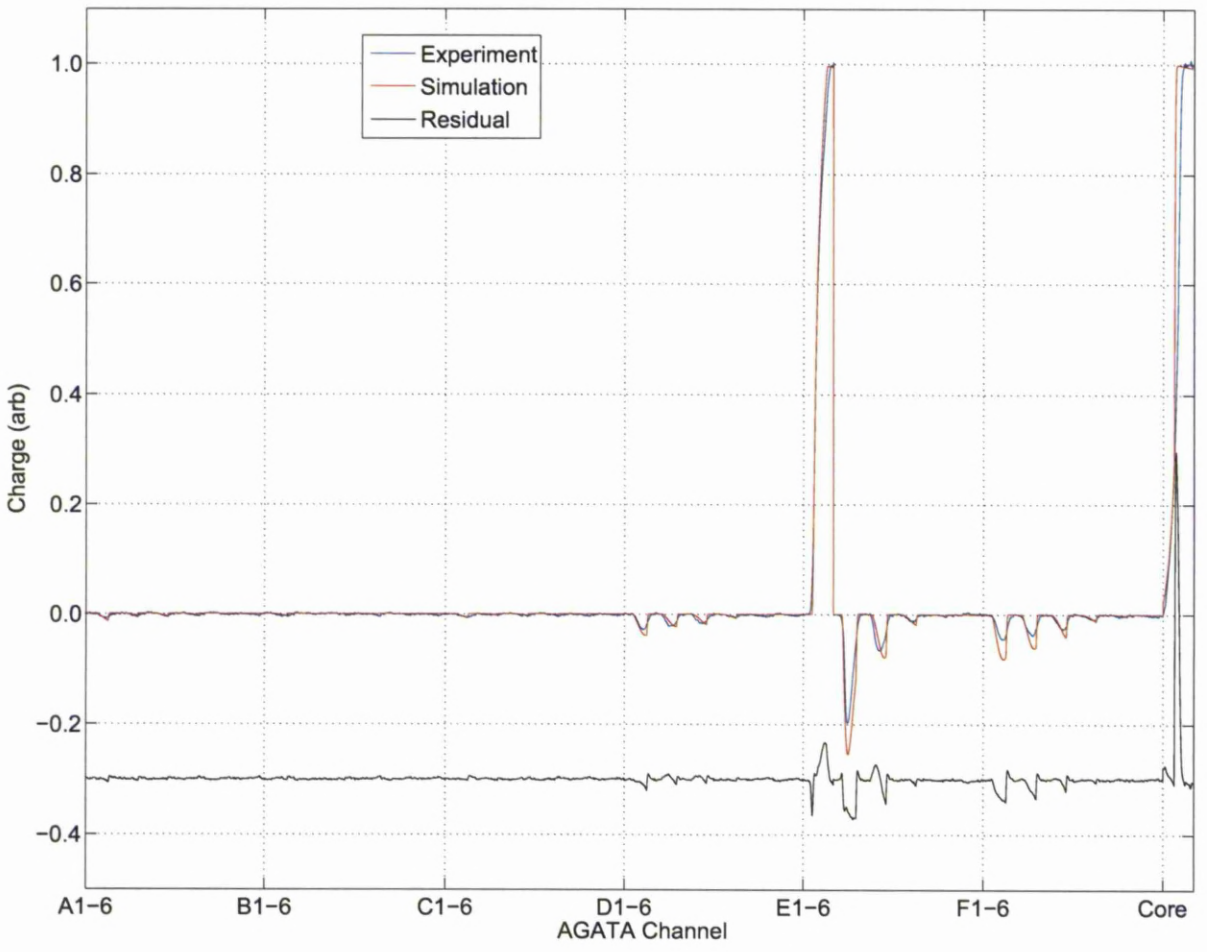

Figure 7.10: The experimental (blue) and JASS (red) signals for all detector segments, for interactions at the position from *Figure 7.7*, closest to the outer contact. The signals have been aligned using a difference minimisation method, the residual difference is shown in black with a negative offset of 0.3 for clarity. The image charges are slightly larger according to the simulation, and the rise time of the core is faster in the simulation, but otherwise there is good agreement.

7.3.2 Azimuth in Segment D1 at Radius of 27mm

Figure 7.11 shows the experimental and simulated signals for positions along an azimuthal arc in segment D1 at z = 6mm and at a radius of 27mm from the detector segmentation centre. From top to bottom, the signals shown are due to the core, and left, hit and right segments. As in the previous section, the experimental signal is shown on the left, JASS in the centre, and MGS on the right. *Figure 7.12* shows the quiver plots produced by performing PSA on the experimental data using the JASS (left) and MGS (right) bases.

The data from these positions demonstrates a common problem found throughout this work that is responsible for a significant reduction in the accuracy of the position reconstruction. There is generally good agreement between the signals from experiment and either simulation, for the core and hit segment signals, although the JASS basis again produces and unusually sharp rise for the final section of the pulse at some positions. The simulations however, produce a larger range of image charge magnitudes in the left and right segments than is observed in experiment. This results in the effect seen in *Figure 7.12*, where the PSA position is shifted away from the segment boundaries relative to the experimental position.

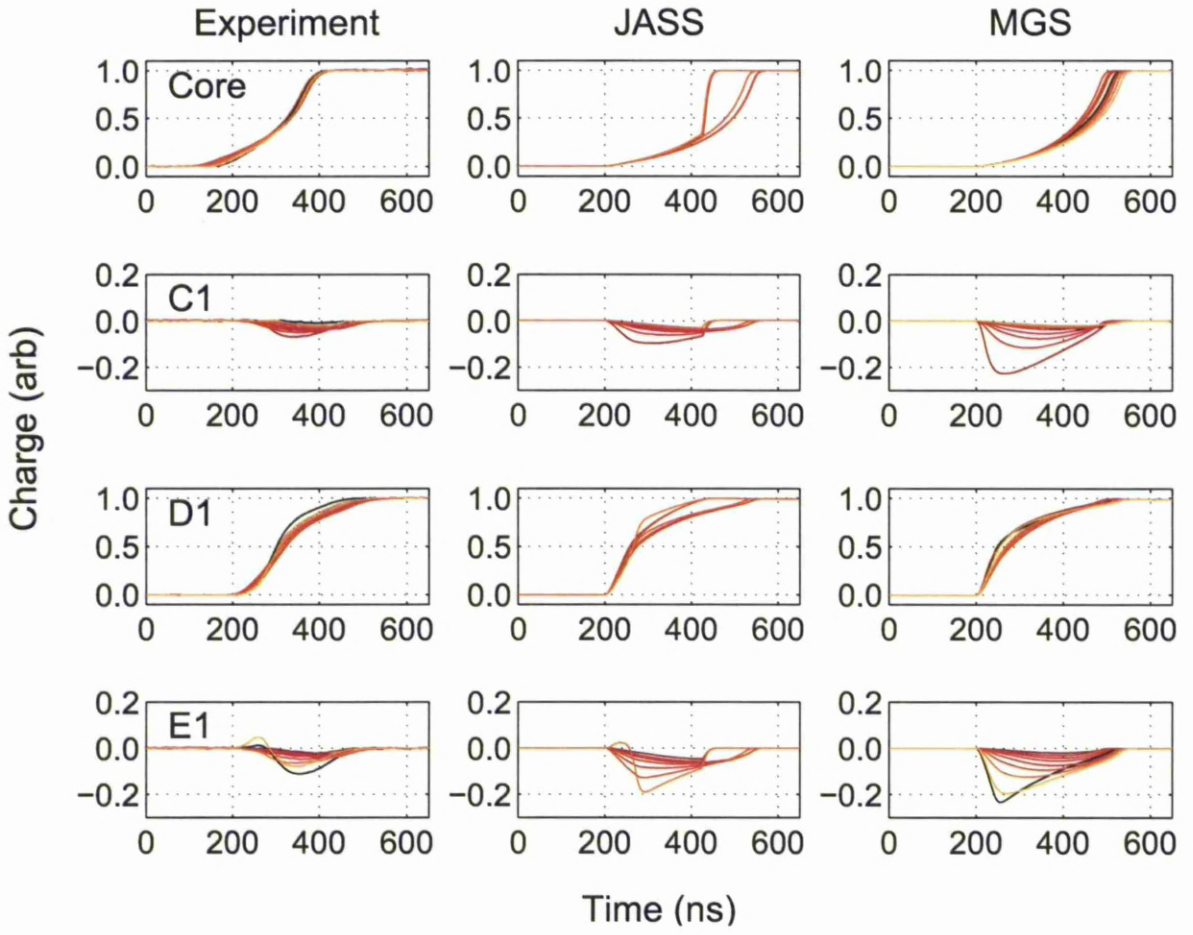

Figure 7.11: Signals from the core (top), left (2nd from top), hit (3rd from top) and right (bottom) segments for interactions in segment D1, at a radius of 27mm. Experimental signals (left) are shown along with those from the JASS (centre) and MGS (right) electric field simulations. There is relatively close matching of the rising edge for all three sets of signals, apart from three positions in the JASS basis that have an unusually fast rise over the last 50%. The image charge magnitudes seen in experiment are smaller than those found in either simulation.

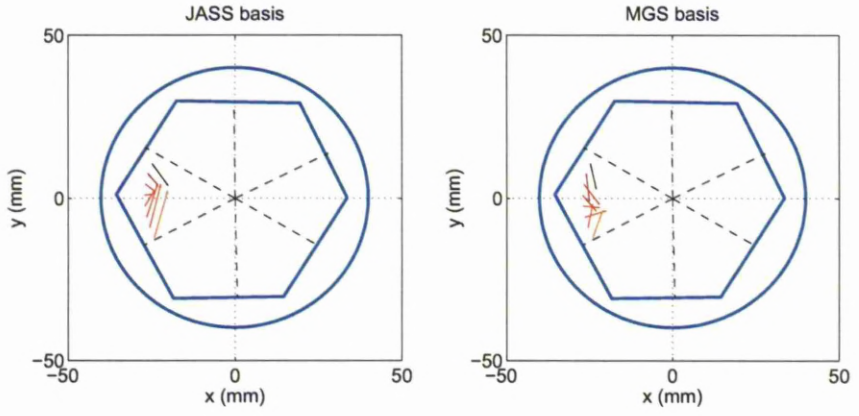

Figure 7.12: Quiver plots showing the positions determined by PSA for the experimental signals shown in *Figure 7.11*, using the JASS (left) and MGS (right) signal bases. The interaction positions found by PSA using either of the electric field simulations are found to cluster near to the centre of the segment. This is due to the smaller image charge magnitudes seen in the experimental data which result in a best match found at positions where the simulated image charges are smaller.

7.3.3 Azimuth in Segment E2 at Radius of 27mm

Figure 7.13 shows experimental and simulated signals produced by interactions along an azimuthal arc in segment E2 at z=17.5mm and at a radius of 27mm from the detector segmentation centre. From top to bottom, the signals shown are due to the core, and left, hit and right segments.

As with the similar example discussed in the last section, the MGS and experimental real charge signals match well. The experimental image charge magnitudes however show a much smaller variation in image charge magnitude than is predicted by MGS. This is again reflected in PSA positions found away from the segment boundary (*Figure 7.14*).

As before, the JASS core signals show a discontinuity in the rising edge which is not reproduced in experiment, here the sudden change in gradient occurs at a much smaller fraction of the total height. The image charge magnitude according to the JASS signals is similar to that seen in experiment, however there are quite significant differences in the shape.

Figure 7.15 shows the experimental and MGS signals, together with the residual, for the position next to the boundary with sector F (orange on *Figure 7.13*). There is close agreement between the simulated and experimental real charge signals, which is reflected in the accuracy in the determination of radial position. The up and down image charge signals are larger in MGS, leaving a significant residual.

Figure 7.16 shows the experimental and JASS signals, for the same position. Here all of the signals leave large residuals due to significantly faster rise times in JASS. The image charge magnitudes here are much closer to those seen in experiment than was the case for MGS.

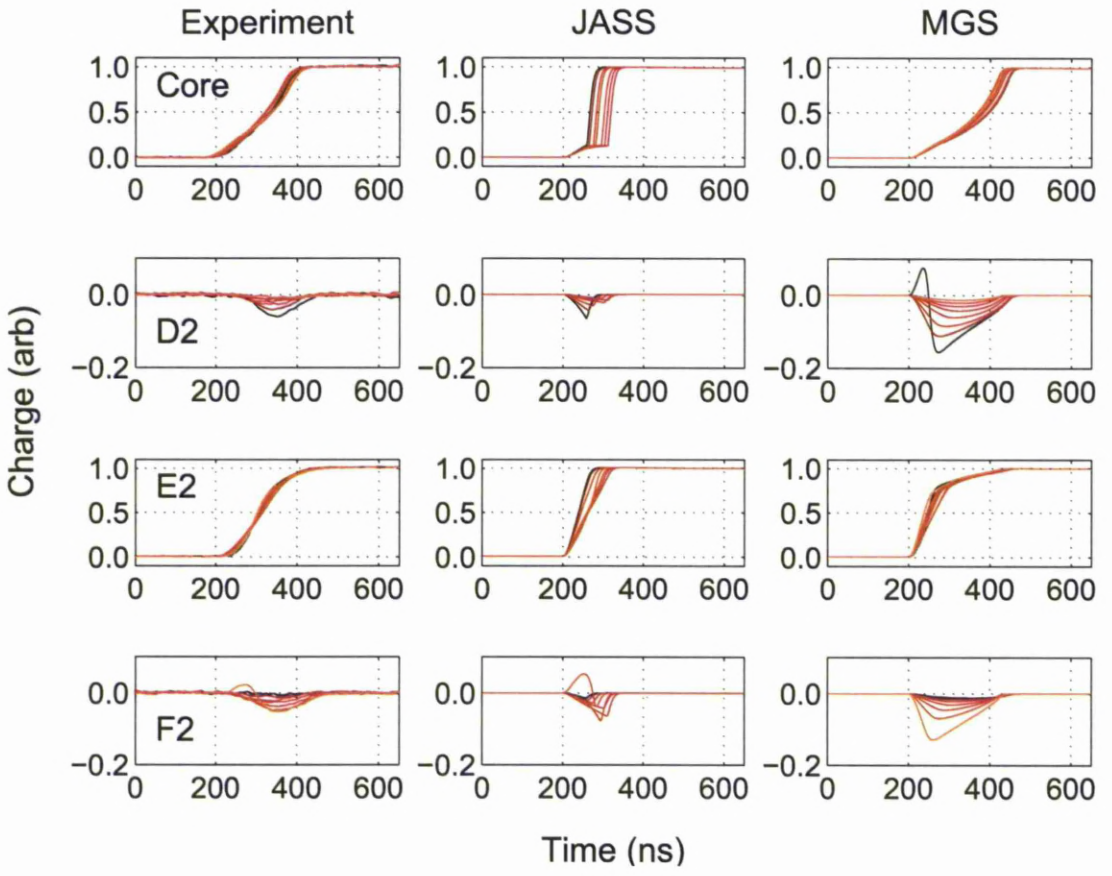

Figure 7.13: Signals from the core (top), left (2nd from top), hit (3rd from top) and right (bottom) segments for interactions in segment E2, at a radius of 27mm. There is little variation in the rise time of these signals due to the constant radius of the interactions, and hence constant charge collection distance. The JASS signals show a small image charge magnitude, comparable to that seen in the experimental data, however the rising edge of the core signal seems to be somewhat discontinuous near the start of its rising edge. The MGS signals have a very similar shape to the experimental signals in the rising edge, but a much larger image charge magnitude.

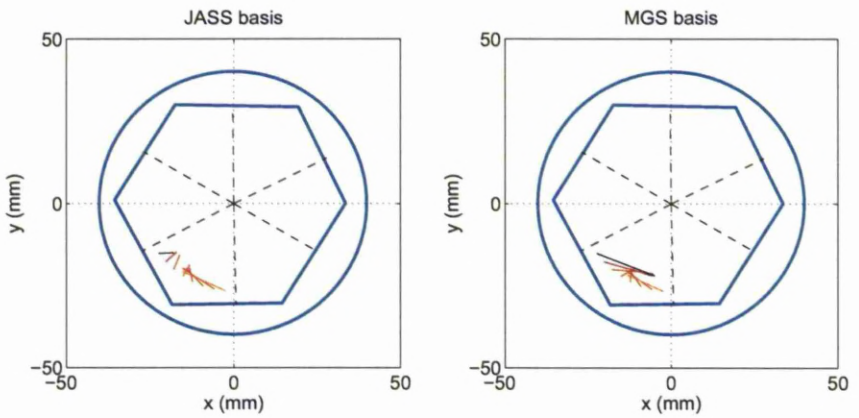

Figure 7.14: Quiver plots showing the positions determined by PSA for the experimental signals shown in *Figure 7.13*, using the JASS (left) and MGS (right) signal bases. Both bases produce relatively good determination of the radius of interaction, but there is a large error in the azimuthal position due to the difference between experimental and simulated image charge magnitude.

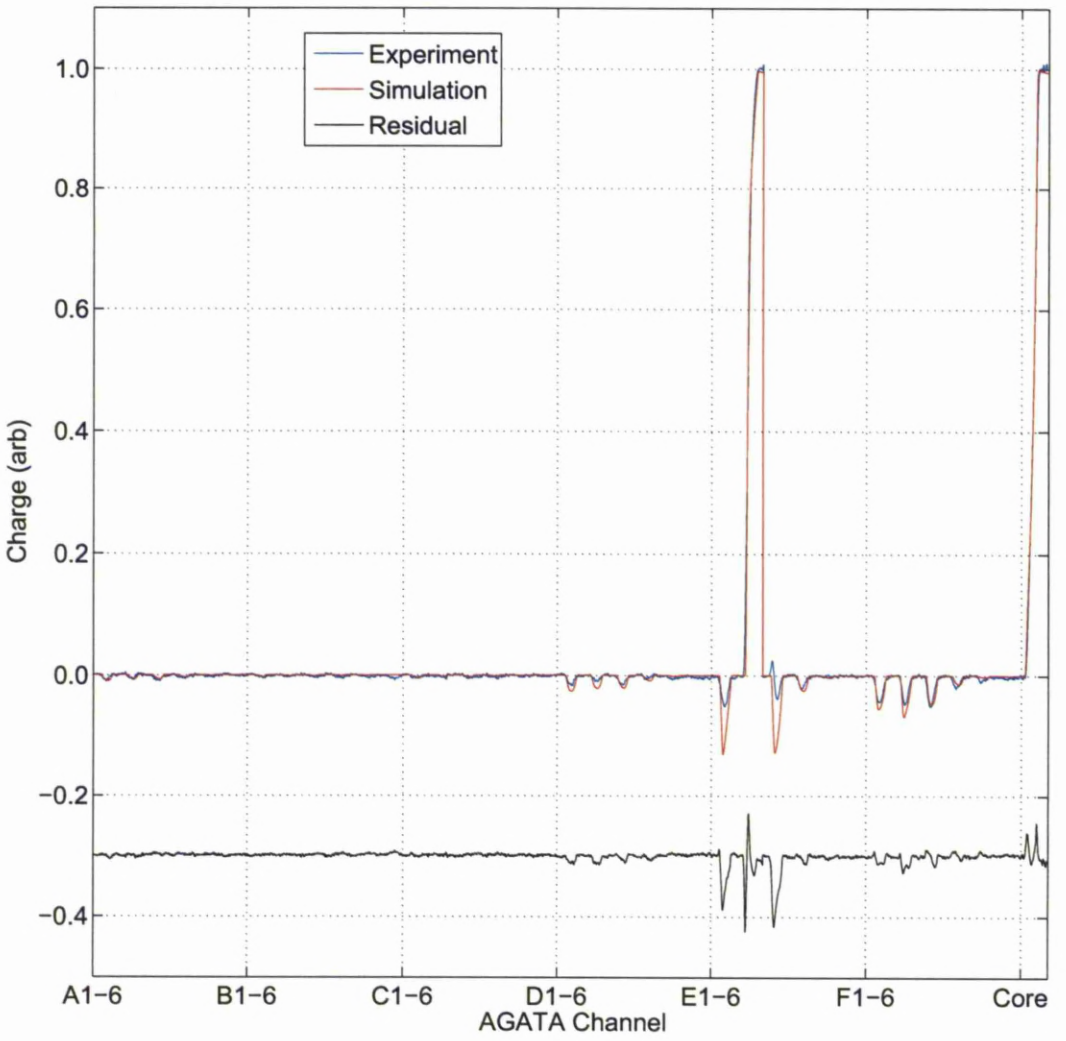

Figure 7.15: The experimental (blue) and MGS (red) signals for all detector segments, for an interaction from *Figure 7.13*, near the boundary with sector F. The interaction position is the same as that shown in *Figure 7.16*. The signals have been aligned using a difference minimisation method, the residual difference is shown in black with a negative offset of 0.3 for clarity. There is good agreement here between the rising edges, and relatively good agreement with the image charges in segments to the left and right. The up and down image charges are significantly smaller in the experimental data however, leaving a large residual in these channels.

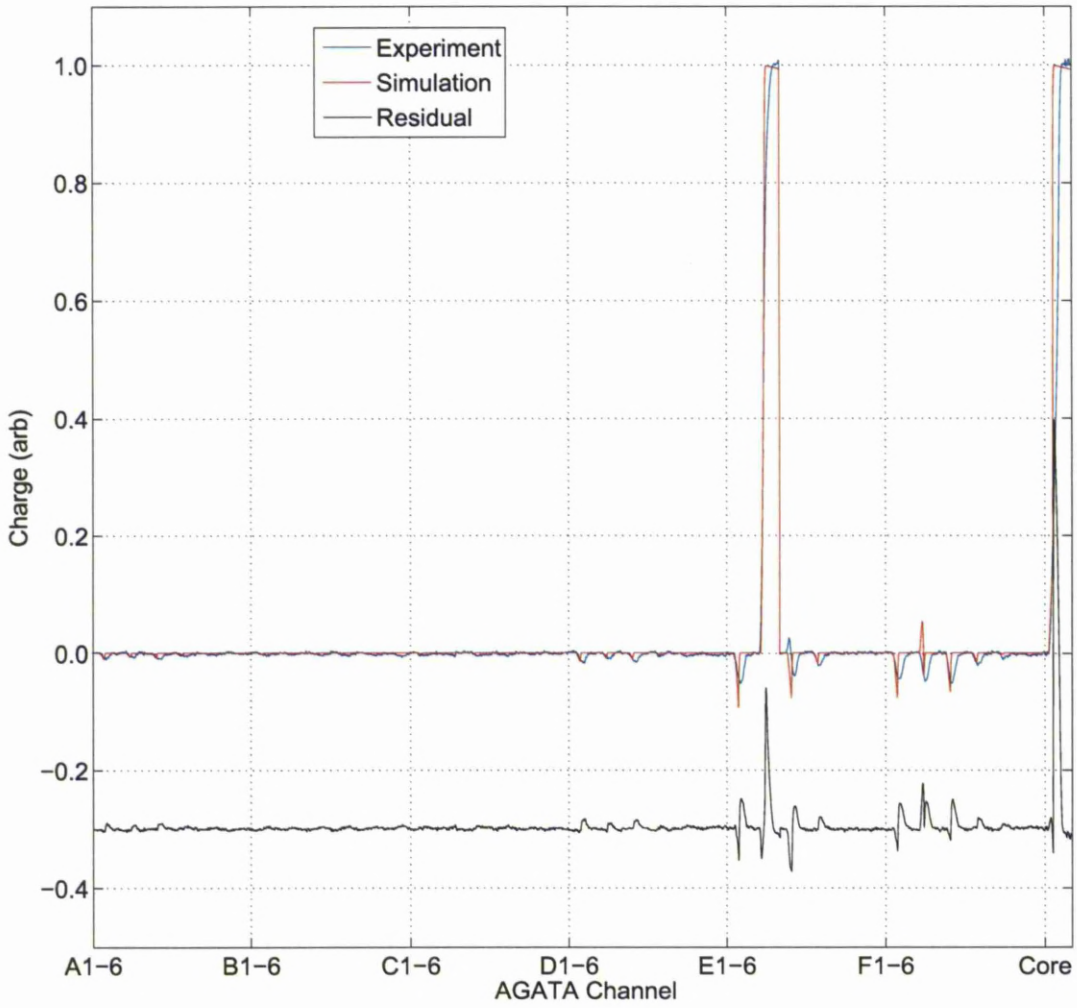

Figure 7.16: The experimental (blue) and JASS (red) signals for all detector segments, for an interaction from *Figure 7.13*, near the boundary with sector F. The signals have been aligned using a difference minimisation method, the residual difference is shown in black with a negative offset of 0.3 for clarity. There is a large residual on both real charge signals, due to the faster rise time of the JASS signal. The image charge magnitudes match more closely, but there is still a discrepancy due to the faster rise time of the simulated signals.

7.3.4 Line Through the Centre of Segment B4

Figure 7.17 shows the experimental and simulated signals for a line of points through the centre of segment B4 at z=51mm. From top to bottom, the plot shows the left, right, up, hit and down segments. The real charge signals match very closely for all three sets of signals. The up and down image charge signals in JASS and MGS are also very close matching, with a steady progression from positive to negative with increasing radius. Unusually however, the image charge magnitudes to the left are larger in JASS, but those to the right are larger in MGS. This is likely due to the differing segmentation boundaries in the two simulations, discussed in *Section 3.6.2.*

The experimental image charge magnitudes to the left and right are much smaller than those seen in the simulations. This causes particular problems in the JASS basis, for which PSA produces a significant offset toward the outside of the segment (*Figure 7.18*). The positions reproduced by PSA using the MGS basis are very close to the experimentally determined positions.

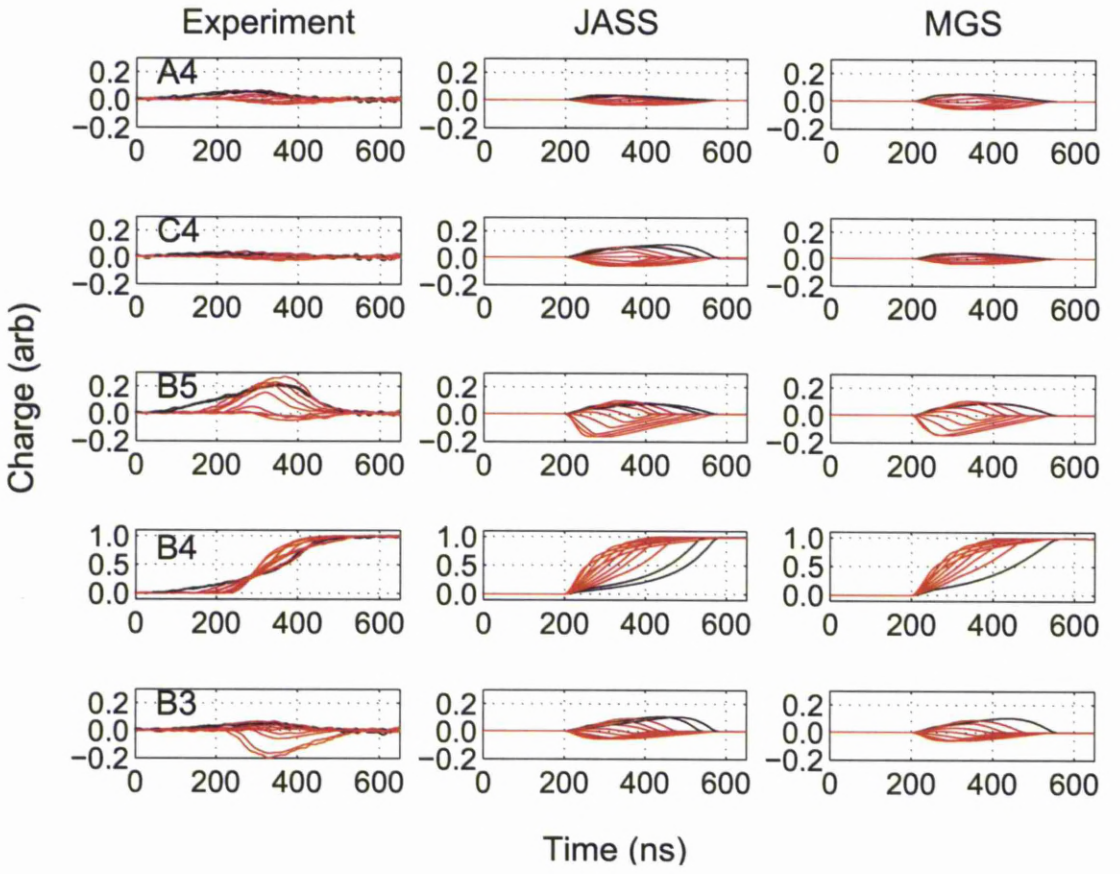

Figure 7.17: Signals from the left, right, up, hit and down segments (top-bottom) for interactions in segment B4, according to experiment (left), JASS (centre), and MGS (right). There is little variation in the rise time of these signals due to the constant radius of the interactions, and hence constant charge collection distance. The range of rise times is similar for all three sets of signals, however the range of image charge magnitudes is somewhat greater in both simulations. There is also some discrepancy in the image charge polarity in the up and down segments.

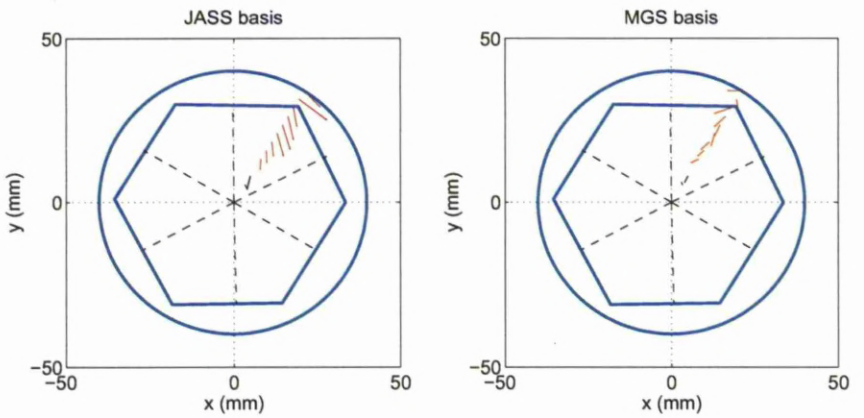

Figure 7.18: Quiver plots showing the positions determined by PSA for the experimental signals shown in *Figure 7.17*, using the JASS (left) and MGS (right) signal bases. The radius of each interaction is determined with reasonable accuracy by either simulation. The azimuthal position is subject to a greater degree of error, particularly when using the JASS basis, due to the discrepancy in the image charge magnitude.

7.4 Detector Position Resolution

For each position in the coincidence scan, *Figure 7.19* shows the difference between the experimentally determined position and that found by PSA with the JASS basis. The data are separated into the six depths at which coincidence scan data were collected. Each point on the plot represents the experimentally determined position of a mean signal, while the colour of the point indicates the distance in mm to the PSA position.

The offset distance is measured in all three dimensions so some of the information about the position resolution in individual positions is hidden. For example, the position resolution in x and y is better at small radii, while the resolution in z is better at larger radii. The combination of these two effects produces a roughly uniform resolution across the xy planes indicated in the plots. The mean distance for all positions is 8.4mm.

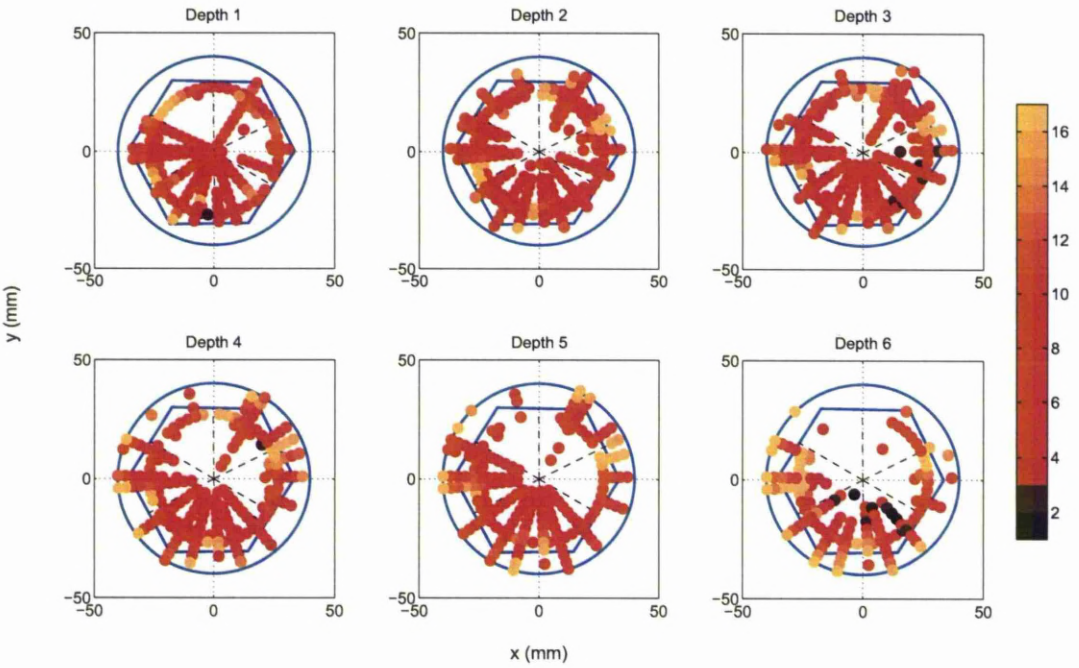

Figure 7.19: The magnitude of the difference between the position determined experimentally and by PSA with the JASS basis. The position of the points represents the experimentally determined position and the colour scale represents the distance, in mm, to the position found by PSA.

Figure 7.20 shows the same plot for PSA using the MGS basis. The mean offset seen here

is 7.3 mm. There is a significantly higher offset seen in the back ring of the detector. This is due to the tendency of MGS to cluster events away from the region near the passivation layer due the anomalously high rise times seen here.

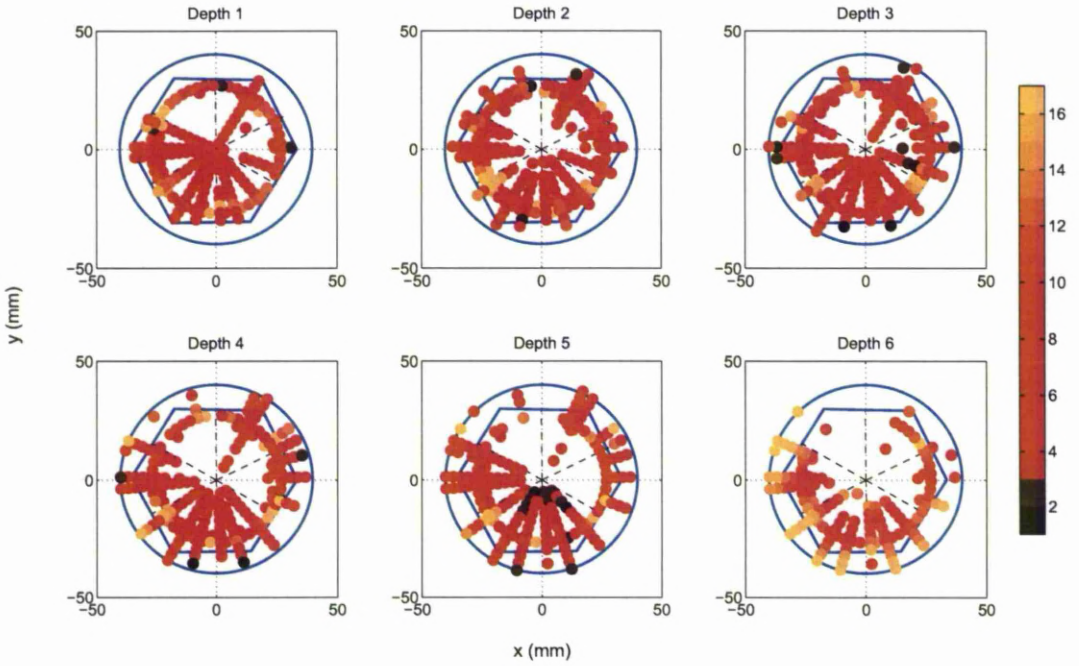

Figure 7.20: The magnitude of the difference between the position determined experimentally and by PSA with the MGS basis. The position of the points represents the experimentally determined position and the colour scale represents the distance, in mm, to the position found by PSA.

Table 7.1 shows the mean displacement found with each basis, the displacements in each direction and the total are included. For comparison the mean displacement found previously for the AGATA symmetric prototype detectors using basis [Dim08] and parametric [Nel08] PSA are included.

7.4.1 Experimental Causes of Poorer Than Expected Position Resolution

The mean position resolutions determined in this work, shown in *Table 7.1*, are significantly larger than expected using either of the electric field simulations. This is due to systematic differences between the simulated basis and experimental data which result in the most

Source	dR (mm)	dx (mm)	dy (mm)	dz (mm)
This Work (JASS)	8.4	3.9	4.2	4.1
This Work (MGS)	7.3	4.3	3.7	3.6
[Dim08] (MGS)	2.5	-	-	-
[Nel08] (Parametric)	9.3	-	-	-

Table 7.1: The position resolution achieved applying PSA to the mean signals produced in this work using JASS and MGS. The values are calculated according to the mean displacement between the position found using the coincidence scanning method, and that found by a basis search. The values in each different dimension are also included. For comparison mean position resolutions measured using the AGATA symmetric prototype detectors are also included. In [Dim08] the resolution was calculated in the same manner as this work, using an MGS basis. In [Nel08] a parametric approach to PSA was applied instead of a basis search, the mean resolution was estimated from the precision of Doppler correction in in-beam measurements.

similar signals being from different positions.

The differences in rise time between the simulations and experiment cause significant shifts in the radial direction. In both JASS and MGS there are regions where the total rise time of signals is less than that seen in experiment, however this is more prevalent in the JASS basis. This effect causes a shift in the PSA position toward locations with shorter rise times at intermediate radii. The discontinuity seen in the rising edge of JASS signals at some locations also has the effect of introducing a shift in the radial direction.

Differences in the image charge magnitude are also apparent, in particular in the magnitude of image charge signals induced in segments neighbouring the hit segment show a smaller range in experiment than in simulation. This resulted in a tendency for the best matching simulated position to be further from the segment boundary than the true position of the experimental signal.

There are reasons to believe that some of these differences are due to errors in the experimental rather than simulated data:

- [RBF+09] reported a position resolution of 2.1mm (5mm FWHM) achieved using an MGS basis with in-beam experimental data. The position resolution was measured by comparing the width of a Doppler broadened gamma-ray peak produced from in-beam with data simulated using a range of position resolutions. This suggests that

something other than the MGS basis is contributing to the 7.3mm mean position resolution observed in this work.

- A novel method for obtaining signals from single interaction sites in a highly segmented detector was recently proposed [CCM+08]. The method is called a *Pulse Shape Comparison Scan* (PSCS) and it relies on comparing signals from two independent singles scans, performed using orthogonal collimator directions. In order to asses this new method of scanning, data collected for this thesis were shared with collaborators from the University of Milan who performed such an analysis using the front and side singles scan data. Early results from this work are presented in [CMW+08] and the results show a range of image charge magnitudes greater than seen in the coincidence scan and in agreement with those seen in JASS and MGS.

Every effort has been made during this work to identify the cause of the smaller than expected image charge signals. Possible sources were divided into four categories:

- **Scaling**: The possibility that the image charge signals were being scaled unintentionally during some stage of the analysis was investigated. Several possible sources of such a mistake were considered and tested, including during gain matching and crosstalk correction. This was finally ruled out as a source of the problem by examining the baseline noise distribution for real and image charge mean signals, as no significant difference was noticed between the two, scaling was ruled out as a source of the problem.

- **Alignment**: Misalignment of the signals during mean pulse formation would produce mean signals with reduced image charge magnitudes and longer rise times. After careful checking of the alignment codes and the resulting aligned signals, this option was ruled out by comparing the mean signals for some of the affected positions with the individual contributions to the mean. No significant difference in image charge magnitude was detected.

- **Filtering**: It is possible that, either through the analysis process or through the initial triggering system, the larger image charges were selectively filtered, leaving signals with systematically smaller than average image charge magnitudes. The analysis

codes were checked thoroughly for this, gating conditions were relaxed at all stages and the effect on the image charge magnitudes monitored, but no source of the problem was revealed. It was not possible to rule out filtering at the triggering stage as the detector was shipped away from Liverpool before this problem was identified, ruling out the possibility of repeat measurements.

- **Electronics**: It is possible that fault in the digitisers or other electronic units resulted in the attenuation of image charge signals or the rejection of events containing larger image charges.

It was not possible to eliminate either of the last two possible sources of the reduced image charge magnitude. Two problems were identified with the data recorded by the digitisers which could be related to the image charge problem:

- Throughout all of the measurements that were conducted, between 5 and 10% of the events had missing data on one or more digitiser cards, this was discussed in more detail in *Section 4.2.1*. Although no correlation was found between the number of events with missing data and the collimator position, it is possible that some systematic bias was introduced to the data through this problem.

- The energy values returned by the MWD algorithm for the core were shown to be lower than the true value for ≈8% of the events (see *Section 6.3*). These events were rejected from the data however there was no way of monitoring this for other channels as the digitisers were the only source of information on segment energy.

Chapter 8

Summary

Digital experimental data were collected from an asymmetric C-type AGATA capsule mounted in a test cryostat using GRETINA digitiser cards and an independent triggering system. Measurements were first conducted using a single trigger condition to probe the mean response of the detector to a collimated beam of 662keV gamma-ray photons (see *Chapter 4*) and calibrate the crosstalk characteristics (see *Chapter 6*). Following that a coincidence scan method, using a second collimator assembly and a series of BGO and NaI scintillation detectors, was used to identify signals from well defined single interaction positions within the detector crystal (see *Chapter 5*).

- The initial tests carried out on the detector showed the electronic noise, energy resolution and efficiency to be within the specification agreed with the crystal manufacturer. The core energy resolution was measured to be 1.29 keV and 2.27 keV at 60 keV and 1332.5 keV respectively, the segment energy resolutions are shown in *Figure 4.1.* The relative efficiency of the detector was found to be 83±2%.

- The proportional crosstalk between detector segments was measured and found to be between 1.5 and 2.5% for all segment combinations. A correction for this effect was successfully implemented.

- The manufacturer specification for AGATA crystals states that the <100> crystal axis, along which charge collection is fastest, should run through the centre of AGATA sector A. Analysis of the rise time distribution as a function of position was conducted

using the singles scan data and it was found that the slower <110> passed through sector A. The simulated signal bases were altered to account for this effect.

- A coincidence scan was conducted and multiple signals were collected from gamma-ray interactions at 2172 single interaction sites through the detector. The systematic variation of the signal shape as a function of position was investigated in detail.

The signals generated by the coincidence scan were later compared with those produced by two different electric field simulations of the detector, MGS and JASS, to assess their accuracy and precision (see *Chapter 3*). A number of observations were made regarding the performance of the simulations.

8.1 MGS

Overall the MGS simulation showed the best performance for PSA with a mean position resolution of 7.3mm.

- The electric and weighting field calculations performed by MGS were conducted on a fixed 1mm spatial grid. This grid was unsuitable for modelling the rapidly changing fields found near the core and segment contacts which resulted in a failure of the simulation at these positions. This causes a reduced effective volume of the detector according to MGS and a systematic error on the position found by PSA for all interactions within 1mm of the contacts. The effect of these missing positions is most significant near the front face of the detector where the contacts are larger and where, in normal operation of the detector, the number of gamma rays interacting is highest.

- Through most of the detector volume, the rise time distribution calculated by MGS matched closely to that seen in experiment.

- For positions near the passivation layer at the back of the detector, the rise time predicted by MGS was significantly longer than that seen in experiment. This resulted in a systematic shift away from this region in the position found by PSA.

- The magnitude of the image charges induced in segments neighbouring the hit segment was larger in MGS than seen in experiment. The degree of the discrepancy varied

through the detector but ultimately resulted in a shift away from segment boundaries of the position found by PSA.

8.2 JASS

PSA performed using a basis produced by the JASS simulation showed a mean position resolution of 8.4mm.

- JASS calculations suggest that, at the impurity concentration and bias suggested by the crystal manufacturer, there are regions near the back of the C001 crystal that remain undepleted. The singles scan measurements show a response from the detector in these regions confirming that the detector is fully depleted. The JASS simulation models the depletion of the detector in a thorough manner, allowing the space charge to equilibrate before recalculating the electric field. As the uncertainty on the impurity concentrations provided by the crystal manufacturer is unknown the concentration was adjusted in the simulation to allow the crystal to more fully deplete.

- The JASS simulation was able to provide simulated signal shapes for interactions throughout the volume of the detector crystal. The systematic variation of the signal shape as a function of position matched that which was found from experiment and the MGS simulation. There were however, a variety of regions in the crystal for which the rise time of the signal was significantly faster than that seen elsewhere. This resulted in a tendency for PSA to identify an interaction within one of these regions as being at the wrong radial position.

- Differential crosstalk was considered as a source of the rise time discrepancy but was ruled out as it cannot effect the full 100% rise time of a signal. The mobility parameters used in the simulation were also considered but ruled out as they were identical to those used in MGS.

- In some regions of the detector there was a sharp discontinuity in the rising edge of the JASS signal and charge collection was completed almost instantaneously. This also caused an error in the radial position found by PSA due to the resulting short rise time.

- As with MGS, the magnitude of the image charges induced in segments neighbouring the hit segment was larger than that seen in experiment. The degree of the discrepancy varied through the detector but resulted in a shift away from segment boundaries of the position found by PSA.

8.3 Future Work at Liverpool

- Analysis is ongoing on a coincidence scan of an A-type AGATA crystal, performed using the Liverpool scanning system and GRETINA digitisers. The results of this scan will be compared with the results presented here to illustrate the differences between the crystal types.

- The GRETINA digitisers and the analogue triggering system will be investigated as a possible source of the smaller than expected image charge magnitudes observed here. It is expected that the position sensitivity will be much improved if this issue is resolved.

- If electric field simulations are to be used to produce the signal basis for PSA in AGATA, it is essential that the response of a detector can be reliably predicted given the crystal specification. This will be tested by scanning another C-type crystal and comparing the results with those found here.

- Development is continuing on the JASS electric field simulation. If a consistently accurate match to experimental data can be produced then another attempt will be made to implement a full electronics calibration using the residual minimisation technique described in *Chapter 6*.

8.4 The AGATA Demonstrator and the Role of this Work

The AGATA demonstrator is currently running in Legnaro National Lab, Italy, with five triple clusters installed. Since February 2010 17 in-beam experiments have been performed with a total of over 100 days of beam time. A range of experimental techniques have been employed including fusion-evaporation reactions, Coulomb excitation and Doppler-

shift lifetime techniques, covering a range of nuclei from ^{15}O to neutron-rich U and Th isotopes.

Techniques have been developed to accurately measure the position resolution achieved in-beam [SRN+11] and FWHM values of 8.6mm at 246 keV and 4mm in the range 1.4-4 MeV have been measured. Work is continuing to further improve on this performance but the resolution of 5mm required for successful application of gamma-ray tracking has already been achieved for most of the energy range investigated by AGATA.

Online PSA in Legnaro has been implemented using the MGS and JASS bases, as well as with the *AGATA Data Library* (ADL) simulation which was not available in time to be considered in this work. The best on-line performance is currently being achieved when using the ADL basis.

The experimental basis generated for this thesis using the coincidence scan method is the only one to have been produced for an asymmetric AGATA crystal. It is critical to improving the performance of on-line PSA that the electric field basis is tested by comparison with experiment and refined to improve its accuracy.

Over the next decade, new detector modules will continue to be added to AGATA increase its efficiency and the algorithms for simulation, PSA and GRT will be continuously developed to optimise the array's performance. The work described in this thesis and the lessons learned from it are vital AGATA's development. This realisation of gamma-ray tracking will have a huge impact on nuclear structure studies at European facilities. The unprecedented efficiency, angular resolution and count rate will allow the investigation of more exotic nuclei than ever before.

Appendix A

Additional Comparison of Experimental and MGS Signals

Figure 7.9 and *Figure A.2* show the experimental and MGS signals for the points at minimum and maximum radius on the line through the centre of segment E1. The signals from the remaining positions on this line are shown in *Section 7.3.1*, together with the quiver plots and JASS signals.

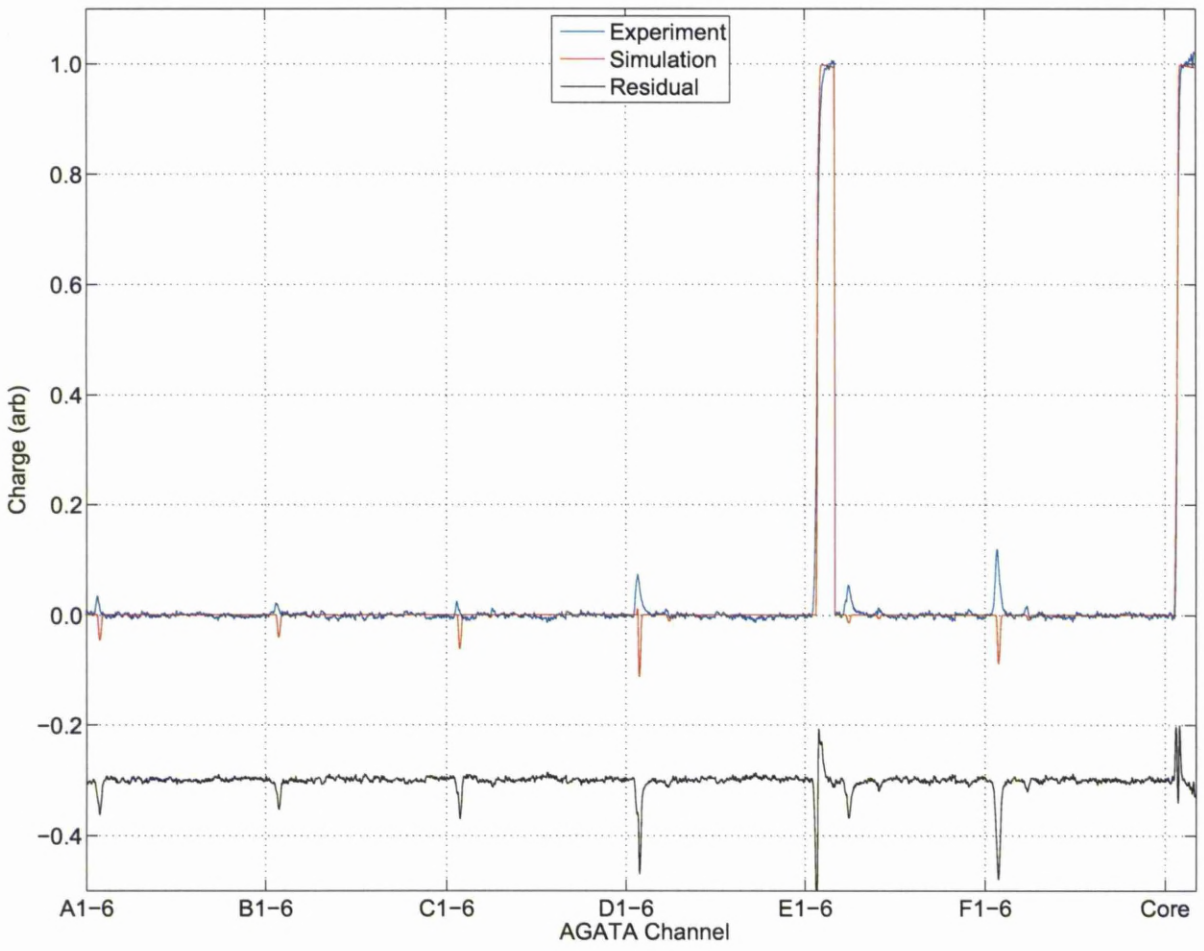

Figure A.1: The experimental (blue) and MGS (red) signals for all detector segments, for interactions at the position from *Figure 7.7*, closest to the central contact.

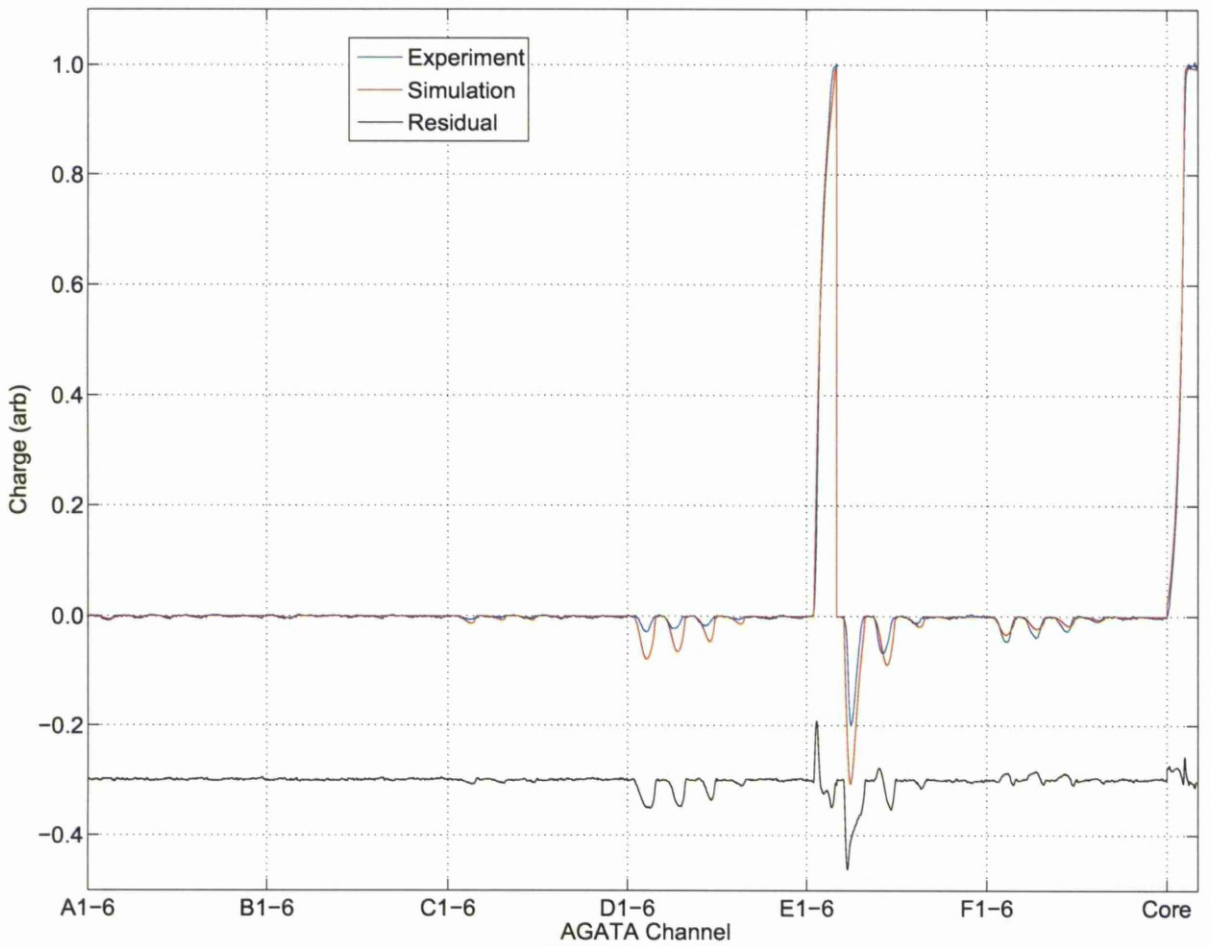

Figure A.2: The experimental (blue) and MGS (red) signals for all detector segments, for interactions at the position from *Figure 7.7*, closest to the outer contact.

Bibliography

[AAA+11] S Akkoyun, G De Angelis, L Arnold, A Ataç, Y Aubert, C Aufranc, A Austin, S Aydin, and F Azaiez. AGATA Advanced Gamma Tracking Array. *Europe*, pages 1–38, 2011.

[AQP05] M Allali, D Quiron, and E Pachoud. Irregular AGATA Canister No C001 - Manufacturer's Report. Technical Report May, 2005.

[BC68] G. Bertolini and A. Coche. *Semiconductor Detectors.* Elsevier Science, 1968.

[BR92] Philip R. Bevington and D. Keith Robinson. *Data Reduction and Error Analysis for The Physical Sciences.* McGraw-Hill Companies, 1992.

[BRP06] Bart Bruyneel, P Reiter, and G Pascovici. Characterization of large volume HPGe detectors. Part II: Experimental results. *Nuclear Instruments and Methods in Physics Research Section A: Accelerators, Spectrometers, Detectors and Associated Equipment*, 569(3):774–789, December 2006.

[Bru08] Bart Bruyneel. On the Origin of Differential Crosstalk in Segmented Detectors. Technical report, IKP Koln, 2008.

[BRW+09a] Bart Bruyneel, P Reiter, Andreas Wiens, J Eberth, Herbert Hess, G Pascovici, N Warr, and D Weisshaar. Crosstalk properties of 36-fold segmented symmetric hexagonal HPGe detectors. *Nuclear Instruments and Methods in Physics Research Section A: Accelerators, Spectrometers, Detectors and Associated Equipment*, 599(2-3):196–208, February 2009.

[BRW+09b] Bart Bruyneel, P Reiter, Andreas Wiens, J Eberth, Herbert Hess, Gheorghe Pascovici, N Warr, Sezgin Aydin, Dino Bazzacco, and F. Recchia. Crosstalk

corrections for improved energy resolution with highly segmented HPGe-detectors. *Nuclear Instruments and Methods in Physics Research Section A: Accelerators, Spectrometers, Detectors and Associated Equipment*, 608(1):99–106, September 2009.

[BS96] C W Beausang and J. Simpson. Large arrays of escape suppressed spectrometers for nuclear structure experiments. *J. Phys.G: Nucl. Part. Phys*, 22(5):527–558, May 1996.

[CCM+08] F Crespi, F Camera, B Million, M Sassi, O Wieland, and A Bracco. A novel technique for the characterization of a HPGe detector response based on pulse shape comparison. *Nuclear Instruments and Methods in Physics Research Section A: Accelerators, Spectrometers, Detectors and Associated Equipment*, 593(3):440–447, August 2008.

[CMW+08] F C L Crespi, B Million, O Wieland, Via Celoria, A.J. Boston, C. Unsworth, H. C. Boston, S. Colosimo, S. Moon, P. J. Nolan, and Agata Demonstrator. Characterization of Segmented HPGe Detectors Using Pulse Shape Comparison Methods γ-ray Tracking Detectors. 261(2007):2008–2008, 2008.

[CS] John Cresswell and Janet Sampson. MTsort Language - EDOC033.

[DBC+09] M. R. Dimmock, A.J. Boston, J. Cresswell, I.H. Lazarus, Patrice Medina, P. J. Nolan, Camille Parisel, Cayetano Santos, J. Simpson, and C. Unsworth. Validation of Pulse Shape Simulations for an AGATA Prototype Detector. *IEEE Transactions on Nuclear Science*, 56(4):2415–2425, August 2009.

[DDLM10] F. Didierjean, G. Duchêne, and A. Lopez-Martens. The Deterministic Annealing Filter: A new clustering method for γ-ray tracking algorithms. *Nuclear Instruments and Methods in Physics Research Section A: Accelerators, Spectrometers, Detectors and Associated Equipment*, 615(2):188–200, April 2010.

[Dim08] M. R. Dimmock. *Characterisation of AGATA Symmetric Prototype Detectors.* PhD thesis, University of Liverpool, 2008.

[DJYZ06] Dionisio Doering, John Joseph, Harold Yaver, and Sergio Zimmermann. GRETINA Digitizer Specification. Technical report, 2006.

[DLV+99] M A Deleplanque, I.Y. Lee, K Vetter, G J Schmid, F S Stephens, R M Clark, R M Diamond, P Fallon, and A O Macchiavelli. GRETA : utilizing new concepts in -ray detection . *Nuclear Instruments and Methods in Physics Research*, 430:292–310, 1999.

[DNB+05] M Descovich, P. J. Nolan, A.J. Boston, J Dobson, S Gros, J. Cresswell, J. Simpson, I.H. Lazarus, P Regan, and J Valientedobon. The position response of a large-volume segmented germanium detector. *Nuclear Instruments and Methods in Physics Research Section A: Accelerators, Spectrometers, Detectors and Associated Equipment*, 553(3):512–521, November 2005.

[ES08] J Eberth and J. Simpson. From Ge(Li) detectors to gamma-ray tracking arrays50 years of gamma spectroscopy with germanium detectors. *Progress in Particle and Nuclear Physics*, 60(2):283–337, April 2008.

[FdR+00] F. Azaiez, G. deFrance, R. Julin, P.J. Nolan, B.M. Nyakó, P.M. Walker, -EXOGAM Collaboration, J. Simpson, J. Fouan, W. Korten, G. Sletten, and J. Gerl. The EXOGAM Array:A Radioactive Beam Gamma-Ray Spectrometer. 2000.

[FRB+10] E. Farnea, F. Recchia, D. Bazzacco, Th. Kröll, Zs. Podolyák, B. Quintana, and a. Gadea. Conceptual design and Monte Carlo simulations of the AGATA array. *Nuclear Instruments and Methods in Physics Research Section A: Accelerators, Spectrometers, Detectors and Associated Equipment*, 621(1-3):331–343, September 2010.

[GNdA+03] A. Gadea, D. R. Napoli, G. de Angelis, R. Menegazzo, D. Rosso, F. Scarlassara, C. Ur, N. Blasi, A. Bracco, F. Camera, S. Leoni, B. Million, M. Pignanelli, G. Pollarolo, A. DeRosa, G. Inglima, M. La Commara, G. La Rana, D. Pierroutsakou, M. Romoli, M. Sandoli, P. G. Bizzeti, A. M. Bizzeti-Sona, G. Lo Bianco, C. M. Petrache, A. Zucchiatti, P. Cocconi, B. Quintana, Ch Beck,

D. Curien, G. Duchene, F. Haas, P. Medina, P. Papka, J. Durell, S. J. Freeman, A. Smith, B. Varley, K. Fayz, V. Pucknell, J. Simpson, W. Gelletly, P. Regan, A. M. Stefanini, L. Corradi, M. Axiotis, L. Berti, E. Fioretto, T. Kroell, A. Latina, N. Marginean, G. Maron, T. Martinez, C. Rusu, N. Toniolo, S. Szilner, M. Trotta, D. Bazzacco, S. Beghini, M. Bellato, F. Brandolini, E. Farnea, R. Isocrate, S. M. Lenzi, S. Lunardi, G. Montagnoli, P. Pavan, and C. Rossi Alvarez. Coupling a CLOVER detector array with the PRISMA magnetic spectrometer. *The European Physical Journal A - Hadrons and Nuclei*, 20(1):193–197, April 2003.

[Gor03] A. Gorgen. Position sensitivity of the AGATA prototype crystal analyzed using a database of calculated pulse shapes. 2003.

[Ha09] T. Ha. *Characterisation des Detecteurs d'AGATA et Etude de l'Hyperdeformation Nucleaire dans le Region de Masse 120.* PhD thesis, Universite Paris-Sud 11, Orsay, France, 2009.

[He01] Z. He. Review of the ShockleyRamo theorem and its application in semiconductor gamma-ray detectors. *Nuclear Instruments and Methods in Physics Research Section A: Accelerators,Spectrometers,Detectors and Associated Equipment*, 463(1-2):250–267, May 2001.

[HGH+04] Muhsin Harakeh, Daniel Guerreau, Walter Henning, Mark Huyse, Helmut Leeb, Karsten Riisager, Gerard van der Steenhoven, and Gabriele-Elisabeth Korner. NuPECC Long Range Plan 2004: Perspectives for Nuclear Physics Research in Europe in the Coming Decade and Beyond. Technical report, NuPECC, 2004.

[Jon02] G Jones. Calibration of Compton polarimeters. *Nuclear Instruments and Methods in Physics Research Section A: Accelerators, Spectrometers, Detectors and Associated Equipment*, 491(3):452–459, October 2002.

[Jor94] V Jordanov. Digital synthesis of pulse shapes in real time for high resolution radiation spectroscopy. *Nuclear Instruments and Methods in Physics Research*

Section A: Accelerators, Spectrometers, Detectors and Associated Equipment, 345(2):337–345, June 1994.

[Kit04] Charles Kittel. *Introduction to Solid State Physics.* John Wiley and Sons, 2004.

[Kno10] Glenn F. Knoll. *Radiation Detection and Measurement.* Wiley, 2010.

[KR90] R Keyser and W. Raudorf. Germanium radiation detector manufacturing: Process and advances. *Nuclear Instruments and Methods in Physics Research Section A: Accelerators, Spectrometers, Detectors and Associated Equipment*, 286(3):357–363, January 1990.

[Kra87] Kenneth S. Krane. *Introductory Nuclear Physics.* John Wiley & Sons, 1987.

[Kro96] T Kroll. Analysis of simulated and measured pulse shapes of closed-ended HPGe detectors*1. *Nuclear Instruments and Methods in Physics Research Section A: Accelerators, Spectrometers, Detectors and Associated Equipment*, 371(3):489–496, March 1996.

[LAB+03] I.H. Lazarus, D.E. Appelbe, A.J. Boston, P.J. Coleman-Smith, J.R. Cresswell, M. Descovich, S.A.A. Gros, M. Lauer, J. Norman, C.J. Pearson, V.F.E. Pucknell, J.A. Sampson, G. Turk, and J.J. Valiente-Dobon. The GRT4 VME pulse processing card for segmented germanium detectors. *2003 IEEE Nuclear Science Symposium. Conference Record (IEEE Cat. No.03CH37515)*, pages 1165–1169 Vol.2, 2003.

[Lee90] I.Y. Lee. The GAMMASPHERE. *Nuclear Physics A*, 520:c641–c655, December 1990.

[Lee99] I.Y. Lee. Gamma-ray tracking detectors. *Nuclear Instruments and Methods in Physics Research Section A: Accelerators, Spectrometers, Detectors and Associated Equipment*, 422(1-3):195–200, February 1999.

[LHK+04] A LopezMartens, K Hauschild, A Korichi, J Roccaz, and J Thibaud. \gamma-ray tracking algorithms: a comparison. *Nuclear Instruments and Methods in*

Physics Research Section A: Accelerators, Spectrometers, Detectors and Associated Equipment, 533(3):454–466, November 2004.

[MGL+00] L Mihailescu, W Gast, R.M Lieder, H Brands, and H Jäger. The influence of anisotropic electron drift velocity on the signal shapes of closed-end HPGe detectors. *Nuclear Instruments and Methods in Physics Research Section A: Accelerators, Spectrometers, Detectors and Associated Equipment*, 447(3):350–360, June 2000.

[MSV04] P. Medina, C. Santos, and D. Villaume. A simple method for the characterization of HPGe detectors. *Proceedings of the 21st IEEE Instrumentation and Measurement Technology Conference (IEEE Cat. No.04CH37510)*, pages 1828–1832, 2004.

[Muk76] T. Mukoyama. Range of electrons and positrons. *Nuclear Instruments and Methods*, 34:10–12, 1976.

[Nat63] Marshall Nathan, I. Anisotropy of the Conductivity of n-Type Germanium at High Electric Fields. *Physical Review*, 130(6):5–8, 1963.

[Nel08] Laura Nelson. *The Spatial Resolution Achievable with Parametric Pulse Shape Analysis of AGATA Detectors and its Application to In-beam Data.* PhD thesis, University of Liverpool, 2008.

[NGT85] P. J. Nolan, D. Gifford, and P. Twin. The performance of a bismuth germanate escape suppressed spectrometer. *Nuclear Instruments and Methods in Physics Research Section A: Accelerators, Spectrometers, Detectors and Associated Equipment*, 236(1):95–99, May 1985.

[NSS79] P. J. Nolan and J F Sharpey-Schafer. The measurement of the lifetimes of excited nuclear states. *Reports on Progress in Physics*, 42(1):1–86, January 1979.

[OR87] M Omar and L Reggiani. Drift velocity and diffusivity of hot carriers in germanium: Model calculations. *Solid-State Electronics*, 30(12):1351–1354, December 1987.

[PTVF07] William H. Press, Saul A. Teukolsky, William T. Vetterling, and Brian P. Flannery. *Numerical Recipes 3rd Edition: The Art of Scientific Computing.* Cambridge University Press, 2007.

[PZP06] A. Pullia, F. Zocca, and G. Pascovici. An Advanced Preamplifier for Highly Segmented Germanium Detectors. *IEEE Transactions on Nuclear Science*, 53(5):2869–2875, October 2006.

[Rad10] David (ORNL) Radford. Private communication: Methods used for crosstalk correction in GRETINA collaboration, 2010.

[Ram39] Simon Ramo. Induced by Electron Motion *. *Engineering*, (11):0–1, 1939.

[RBF+09] F. Recchia, D. Bazzacco, E. Farnea, a. Gadea, R. Venturelli, T. Beck, P. Bednarczyk, a. Buerger, a. Dewald, and M. Dimmock. Position resolution of the prototype AGATA triple-cluster detector from an in-beam experiment. *Nuclear Instruments and Methods in Physics Research Section A: Accelerators, Spectrometers, Detectors and Associated Equipment*, 604(3):555–562, June 2009.

[RBP82] T.W. Raudorf, M.O. Bedwell, and T.J. Paulus. Pulse Shape and Risetime Distribution Calculations for HPGe Coaxial Detectors. *IEEE Transactions on Nuclear Science*, NS-29(1):764–768, 1982.

[RCNO77] L. Reggiani, C. Canali, F. Nava, and G. Ottaviani. Hole drift velocity in germanium. *Physical Review B*, 16(6):2781–2791, September 1977.

[RN95] Ingemar Ragnarsson and Sven Gvsta Nilsson. *Shapes and Shells in Nuclear Structure.* Cambridge University Press, 1995.

[Sav03] H Savajols. VAMOS: A variable mode high acceptance spectrometer for identifying reaction products induced by SPIRAL beams. *Nuclear Instruments and Methods in Physics Research Section B: Beam Interactions with Materials and Atoms*, 204:146–153, May 2003.

[Sch09a] Michael Christian Schlarb. Private Communication. Technical report, 2009.

[Sch09b] Michael Christian Schlarb. *Simulation and Real-Time Analysis of Pulse Shapes from segmented HPGe-Detectors.* PhD thesis, 2009.

[Sim05] J Simpson. THE AGATA SPECTROMETER. *Acta Physica Polonica B*, 36(4):1383–1393, 2005.

[Sim06] J. Simpson. The AGATA project. *Journal of Physics: Conference Series*, 41(1):72–80, May 2006.

[SRN+11] P.-A. Söderström, F. Recchia, J. Nyberg, A. Al-Adili, A. Ataç, S. Aydin, D. Bazzacco, P. Bednarczyk, B. Birkenbach, and D. Bortolato. Interaction position resolution simulations and in-beam measurements of the AGATA HPGe detectors. *Nuclear Instruments and Methods in Physics Research Section A: Accelerators, Spectrometers, Detectors and Associated Equipment*, 638(1):109–96, March 2011.

[SSS88] J F Sharpey-Schafer and J. Simpson. Escape suppressed spectrometer arrays: A revolution in γ-ray spectroscopy. *Progress in Particle and Nuclear Physics*, 21:293–400, 1988.

[UK 07] UK Nuclear Physics Community. A Strategy for UK Nuclear Physics: Discussion document for Nuclear Physics Town meeting on 24th January 2007. Technical report, 2007.

[Vet00] K Vetter. Three-dimensional position sensitivity in two-dimensionally segmented HP-Ge detectors. *Nuclear Instruments and Methods in Physics Research Section A: Accelerators, Spectrometers, Detectors and Associated Equipment*, 452(1-2):223–238, September 2000.

[VKLL01] T Vidmar, M Korun, A Likar, and M Lipoglavsek. A physically founded model of the efficiency curve in gamma-ray spectrometry. *Journal of Physics D: Applied Physics*, 34(16):2555–2560, August 2001.

[WHB+10] Andreas Wiens, Herbert Hess, Benedikt Birkenbach, Bart Bruyneel, J Eberth, Daniel Lersch, Gheorghe Pascovici, Peter Reiter, and Heinz-georg Thomas. The AGATA triple cluster detector. *Nuclear Instruments and Methods in Physics Research Section A: Accelerators, Spectrometers, Detectors and Associated Equipment*, 618(1-3):223–233, June 2010.